

---

Non-equilibrium dynamics in  
one-dimensional spin-polarized Fermi gases  
with resonant interaction

---

Master Thesis

by

Jan Philipp Kumlin

from Waiblingen



Department of Physics  
Ludwig-Maximilians-Universität

September 16, 2015

Munich



---

Nichtgleichgewichtsdynamik in  
eindimensionalen spin-polarisierten  
Fermi-Gasen mit resonanter Wechselwirkung

---

Masterarbeit

von

Jan Philipp Kumlin

aus Waiblingen



Fakultät für Physik  
Ludwig-Maximilians-Universität

16. September 2015

München



Advisor: PD Dr. Fabian Heidrich-Meisner



# Contents

<b>Introduction</b>	<b>1</b>
<b>1. FFLO Phase and Bose-Fermi Resonance Model</b>	<b>7</b>
1.1. FFLO phase . . . . .	7
1.1.1. Pairing mechanism in the FFLO phase: Mismatch of Fermi surfaces	8
1.1.2. Correlations in FFLO phase . . . . .	10
1.1.3. Realization of the FFLO phase in one dimensional spin-imbalanced gases . . . . .	11
1.1.4. FFLO phase in traps . . . . .	14
1.1.5. Experimental observation . . . . .	15
1.2. Bose-Fermi resonance model . . . . .	15
1.2.1. BFRM in the continuum . . . . .	15
1.2.2. BFRM on a lattice . . . . .	20
1.2.3. Experimental observation . . . . .	22
<b>2. Quantum Quenches and Slow Ramps: Kibble-Zurek Mechanism</b>	<b>27</b>
2.1. Quantum quenches . . . . .	27
2.2. Slow Ramps: Kibble-Zurek mechanism (KZM) . . . . .	28
2.2.1. Kibble-Zurek mechanism . . . . .	28
2.2.2. Beyond the Kibble-Zurek mechanism . . . . .	34
<b>3. Matrix Product States and Time Evolving Block Decimation</b>	<b>37</b>
3.1. Singular value decomposition and Schmidt decomposition . . . . .	37
3.2. Matrix Product States (MPS) . . . . .	40
3.2.1. Examples . . . . .	41
3.2.2. Normalization . . . . .	42
3.2.3. Calculation of expectation values and correlations . . . . .	42

3.3. Matrix Product Operators (MPO) . . . . .	42
3.4. Time Evolving Block Decimation . . . . .	45
3.4.1. Trotter-Suzuki decomposition . . . . .	45
3.4.2. Vidal representation . . . . .	46
3.4.3. TEBD update process . . . . .	47
3.4.4. Ground state search with TEBD . . . . .	49
3.4.5. Error sources . . . . .	51
3.5. MPS with conserved quantum numbers . . . . .	52
3.5.1. TEBD update process . . . . .	53
3.5.2. Examples . . . . .	54
3.6. iTEBD . . . . .	55
3.6.1. Comparison between TEBD and iTEBD . . . . .	55
3.7. Implementation and test results . . . . .	56
3.7.1. Testing the code . . . . .	57
<b>4. Numerical Results</b>	<b>63</b>
4.1. Ramps across the resonance . . . . .	63
4.1.1. Number of molecules . . . . .	65
4.1.2. Momentum distribution function . . . . .	68
4.1.3. Adiabaticity . . . . .	77
4.2. Connection to Kibble-Zurek theory . . . . .	79
4.3. Central charge . . . . .	85
4.3.1. Consequences for a Kibble-Zurek interpretation . . . . .	86
4.4. Summary . . . . .	89
<b>Summary</b>	<b>91</b>
<b>A. Implementation details</b>	<b>95</b>
<b>B. BFRM and FFLO</b>	<b>99</b>
<b>C. Error control</b>	<b>103</b>
<b>D. Additional figures</b>	<b>107</b>
<b>Bibliography</b>	<b>111</b>

# Introduction

In 1964, Fulde and Ferrell [1] and Larkin and Ovchinnikov [2] proposed a novel type of unconventional superfluid order for attractive weakly interacting fermions in condensed matter systems, extending the ideas of Bardeen, Schrieffer and Cooper [3] in their famous BCS theory to the case of partially spin-polarized systems. Fulde and Ferrell discovered that paired electrons in the superconducting state can acquire non-zero center-of-mass momentum  $\mathbf{q}$  such that they propagate as a plane wave, which breaks both rotational and translational symmetry as well as time-reversal symmetry. On the other hand, Larkin and Ovchinnikov pointed out that a superposition of left and right moving plane waves with opposite momenta  $\mathbf{q}$  and  $-\mathbf{q}$  is energetically favorable compared to the solution found by Fulde and Ferrell and does not break time-reversal symmetry. In this way, the system can exhibit both superfluidity and magnetization. Due to the non-vanishing center-of-mass-momentum  $\mathbf{q} = \mathbf{k}_{F,\uparrow} - \mathbf{k}_{F,\downarrow}$ , the superfluid order parameter itself gets spatially modulated,  $\Delta(x) \sim e^{-iqx}$  for Fulde and Ferrell and  $\Delta(x) \sim \cos(qx)$  for Larkin and Ovchinnikov. In one dimension, the modulation is directly proportional to the polarization of the system,  $q \propto p$ . In addition to that, the FFLO state is expected to be more robust in one dimension as the nesting effect is enhanced in this case and the FFLO phase occupies a larger region in the phase diagram (see [4] and [5] for reviews).

However, an experimental observation of the FFLO phase in condensed-matter systems has remained elusive up today<sup>1</sup>. One reason for that is that in those systems, the possible setting in of the FFLO phase appears at magnetic fields much larger than the critical (Clogston limit [7]) Zeeman field,  $h_c$ . Above this limit, the coupling of the external magnetic field to the orbital motion of the charged electrons becomes dominant and leads to the breakdown of the Meissner effect, in which the magnetic field can penetrate the superconductor leading to a phase transition into the normal phase. In addition to that,

---

<sup>1</sup>However, there is indirect evidence for the FFLO state from the specific heat data of organic superconductors in a strong magnetic field that is parallel to the layer structure [6].

impurity effects can prevent FFLO type of superfluid order in those systems [8, 9].

The situation, though, changed with the realization of ultracold quantum gas experiments that provide a fruitful playground both for experimentalists as well as theorists up to now (for reviews on ultracold quantum gases, see [10–12]). In those experiments, systems can be studied in a very clean and controlled environment. Moreover, with the help of so-called Feshbach resonances [13, 14] interactions can be tuned not only in strength but also in sign such that one can tune the interactions from being attractive to being repulsive and vice versa. Another major achievement has been the realization of optical lattices which allow for constraining the atoms to a quasi-one or two-dimensional geometry. Reviews of experiments with ultracold bosonic and fermionic atoms in one dimension are given in [15] and [16].

From the theoretical point of view, the Gaudin-Yang model [17, 18], which is a model for a two-component Fermi gas in one dimension with a  $\delta$ -potential interaction, as well as its lattice version, the Fermi-Hubbard model, are models which realize the FFLO phase in one dimension. These models have been solved exactly both for the balanced case [19, 20] as well as for the spin-imbalanced case [21, 22] using the Bethe ansatz. For a review of the physics of Fermi gases in one dimension, we refer to [5]. Using bosonization, Yang [23] was able to calculate the characteristic pairing correlations of the FFLO phase,

$$\langle \hat{c}_{i,\uparrow}^\dagger \hat{c}_{i,\downarrow}^\dagger \hat{c}_{j,\downarrow} \hat{c}_{j,\uparrow} \rangle \propto \frac{\cos(q|x|)}{|x|^\alpha}, \quad |x| = |i - j|. \quad (0.1)$$

This result has been also verified for the attractive Fermi-Hubbard model in [24], using the density matrix renormalization group (DMRG) algorithm. Since then, the FFLO state has been studied by various groups using DMRG methods [25–27], quantum Monte Carlo (QMC) [28, 29] and mean-field theory [30, 31].

Experimentally, ultracold Fermi gases in 1D were investigated at ETH by Moritz et al. [32], where they studied the binding of fermions into molecules due to a confinement induced resonance which occurs due to the quasi-1D geometry as a combination of the strong transverse confinement and a Feshbach resonance in the 3D scattering length [33, 34]. Quite recently, at Rice University, Liao et al. [35] measured the density profiles of a (spin-imbalanced) two-component ultracold Fermi gas of  $^6\text{Li}$  atoms in a harmonic trap confined in a quasi-1D geometry using an optical lattice. The imbalance of both fermionic species was achieved by controlling the population of two hyperfine states driving rf sweeps between them at different powers. In this way, they confirmed the key signatures of the 1D phase diagram

calculated in [21,22] where the system exhibits a fully paired phase for small magnetic fields, a fully polarized phase for large magnetic fields and a partially polarized phase exhibiting FFLO correlations. Different from the 3D case, this phase is in the center of the cloud with the wings being either fully paired or fully polarized. However, the experimental data did not reveal the smoking gun signature of the FFLO phase, the momentum distribution function (MDF) of the pairs peaked at non-zero momentum. Several proposals have been made for the unambiguous experimental detection of the FFLO correlations so far, including time-of-flight measurements of the molecule MDF after projecting the pair correlations onto the molecules using a Feshbach resonance [36], measuring of noise correlations [25,37] and rf-spectroscopy [38]. A full overview of the proposals for the experimental observation of FFLO correlations is given in [4].

In the context of this thesis, we will focus on the idea of projecting the pair correlations onto the molecules by ramping the system over a Feshbach resonance. In order to account for the possibility of paired fermions being converted into tightly bound molecules around the resonance, one has to include an additional molecular channel which one can couple to. This leads to the Bose-Fermi resonance model (BFRM) [39,40]. In this model, one adds an additional Feshbach term that couples the fermionic channel to the molecular channel which in general is detuned in energy. The detuning can be varied from being on the BCS side of the resonance to being on the BEC side of the resonance. In 1D, the BFRM for a spin-balanced gas has been studied by Recati et al. [41] and Citro and Orignac [42], while the latter also extended their calculations to the case of a spin-imbalance induced by an external magnetic field [43]. In the context of FFLO correlations, the BCS-BEC crossover in the BFRM was investigated using DMRG in [44], where they also showed the emergence of quantum phase transitions as opposed to the balanced case, where the crossover is a smooth one. In addition to that, Baur et al. [29] showed in a three-body calculation that the phase transition from the FFLO state on the BCS side of the resonance to the BEC state is accompanied with a change in the symmetry of the ground state wave function.

Recently, the dynamics of FFLO correlations has been studied by Riegger et al. for interaction quenches and linear ramps in the Fermi-Hubbard model [45,46] and in the BFRM [45]. In [46], they studied the survival of FFLO correlations for interaction quenches in the Fermi-Hubbard model when changing the interaction from being attractive ( $U_i < 0$ ) to being repulsive ( $U_f = -U_i > 0$ ). They showed, using exact diagonalization (ED) and DMRG that for strong initial interactions, the time averaged post-quench momentum distribution features a strong FFLO peak while for smaller interactions, the height of the

FFLO peak decreases and the position of the maximum gets shifted to larger values of the quasi-momentum  $k$ . In the limit of very weak interactions, the time averaged post-quench pair momentum distribution approaches its post-quench ground state distribution, where the peak is very broad and shifted towards  $k = 0$ . In the case of slow ramps, they found that the visibility of the FFLO peak decreases monotonically with the ramp time and FFLO correlations are lost rapidly (timescale of the order of only a few tunneling times). For the BFRM (studied in [45]), linear ramps across the resonance from the BCS side onto the BEC side were investigated using ED. It was shown that for intermediate polarization ( $p = 1/2$ ), the visibility of the FFLO peak in the time averaged post-ramp momentum distribution of the molecules is enhanced for intermediate ramp times. In the case of large polarization ( $p = 3/4$ ), the visibility is also enhanced for large ramp times, however the parameters of the simulations (i.e. the restriction to small system sizes) only allowed for one single molecule to form.

In the present work, we want to extend the analysis of the survival of FFLO correlations when ramping across the resonance in the BFRM by accessing larger system sizes using the Time Evolving Block Decimation (TEBD) algorithm by Vidal [47, 48]. Different from [45], we will study the momentum distribution of the molecules during the ramp instead of the time averaged post-ramp distribution. We also get a correlation enhancing effect for the visibility at the end of the ramp in the momentum distribution function of the molecules but for larger polarization ( $p = 3/4$ ) and intermediate ramp times, whereas we do not see any enhancing effect for  $p = 1/2$ . Another important aspect of this thesis lies on a better understanding of the dynamics during the ramp. To this end, we study the energy during the ramp and a quantity that we call rescaled energy, which is directly related to the excess energy produced during the ramp. With this quantity, we are able to identify adiabatic scaling of the excess energy according to Kibble-Zurek theory [49, 50] (see also [51]) for the system size under consideration. We find that the scaling exponent is similar for small and intermediate polarization but significantly smaller for large polarization. In order to get a better understanding of the nature of the quantum phase transitions that are crossed during the ramp, we further calculate the central charge of the different phases which is associated with the number of gapless excitations in the system. For the FFLO phase, we find a central charge  $c \approx 2$  accounting for the gapless spin and charge excitations in a spin-imbalanced Fermi gas with attractive interactions. In the intermediate phase, where we have coexistence of paired fermions and molecules, we find  $c \approx 3$ . In the BEC+FP FG phase, where we have a BEC of molecules and a system of fully polarized fermions, we

expect again  $c = 2$ . However, the quality of our data did not allow for a calculation of the central charge.

## **Outline**

The thesis is structured in the following way: The first chapter is dedicated to the physics of our work where we discuss the pairing mechanism in the FFLO phase as well as its characteristic signatures. We introduce the BFRM as a two-channel model and discuss its physics for a spin-imbalanced Fermi gas at zero temperature.

In the second chapter, we explain the concept of the Kibble-Zurek mechanism, accounting for the non-equilibrium dynamics during the ramp.

In the third chapter, we review the concept and the theoretical background of Matrix Product States (MPS) and the important aspects of the TEBD algorithm. We will also point out the use of conserved Abelian quantum numbers and present the key parts of our implementation.

In the last chapter, we present and discuss our results obtained from numerical simulations.



# 1. FFLO Phase and Bose-Fermi Resonance Model

In this chapter, we review the basic properties and characteristics of the FFLO phase as well as the Gaudin-Yang model, which realizes the FFLO phase. In Section 1.2, we introduce the Bose-Fermi resonance model (BFRM) as a two-channel model and discuss its phase diagram calculated in [44] for the case of a spin-imbalanced Fermi gas.

## 1.1. FFLO phase

The FFLO phase was first proposed independently by Fulde and Ferrell [1] and Larkin and Ovchinnikov [2] for fermionic superfluids coupled to an external magnetic field. Other systems like quark condensates are also supposed to exhibit FFLO phases [52, 53].

According to standard BCS-theory, below a critical temperature  $T_c$ , up- and down-fermions can form Cooper pairs and condense, forming the well-known BCS ground state. For an equal population of both spin species (or equivalently, no external magnetic field), the Cooper pairs have vanishing center-of-mass momentum. However, in the case of a non-vanishing external field, a possible pairing at non-zero center-of-mass momentum exists. In reality, an applied magnetic field does not only couple to the polarization of a system due to the Zeeman effect but also to the orbital motion of charged electrons. In type I superconductors, there exists some critical field  $h_c$  for which the superconductor cannot any longer expel the external field leading to a breakdown of superconductivity due to the coupling of the magnetic field to the orbital motion of the electrons. Unfortunately, in condensed-matter systems, this field is much smaller than the critical Zeeman field  $h_c^Z$ , i.e.  $h_c/h_c^Z = \sqrt{4\pi\chi_P} \ll 1$  (with  $\chi_P$  the Pauli paramagnetic susceptibility), which leads to breakdown of the ordered phase before a possible FFLO phase may set in. In addition, impurity effects can also prevent the realization of FFLO states [8].

### 1.1.1. Pairing mechanism in the FFLO phase: Mismatch of Fermi surfaces

In standard (equal population) BCS theory, the order parameter of the superconducting phase is given by the expectation value of fermionic s-wave pairs with opposite momentum

$$\Delta = \langle \hat{c}_{k,\uparrow} \hat{c}_{-k,\downarrow} \rangle, \quad (1.1)$$

where the momentum  $k$  is located very close to the Fermi surface. For a spin-balanced gas, the fermions pair at opposite momentum and opposite spin as in this case, the interaction volume is maximal (c.f. Fig. 1.1).

For spin-imbalanced systems, the situation changes as the Fermi surfaces of both spin species do not match any longer. In order to still get the maximal interaction volume for the scattering process of two fermions with opposite spin, the Fermi surfaces have to be shifted relative to each other by some wavevector  $\mathbf{q} \neq 0$ . Thus, the resulting Cooper pair acquires a non-vanishing center of mass momentum  $\mathbf{q} = \mathbf{k}_{F,\uparrow} - \mathbf{k}_{F,\downarrow}$ . As a result, the pairing for a spin-imbalanced gas of attractively interacting fermions can be understood in terms of a nesting effect of the Fermi surfaces of both species.

As can be seen in Fig. 1.2, the effect is more pronounced in lower dimensions as the fraction of fermions in the FFLO state becomes larger. For one-dimensional systems, the Fermi wavevector is directly proportional to the density, leading to

$$q_{1D} = \pi(n_{\uparrow} - n_{\downarrow}) = \pi n p, \quad (1.2)$$

where we introduced the polarization  $p = \frac{N_{\uparrow} - N_{\downarrow}}{N}$ . Thus, the FFLO momentum is directly proportional to the polarization  $p$  in 1D. The Cooper pairs in the FFLO state hence propagate through the system with some momentum  $q$ . For time-reversal symmetric Hamiltonians (like the BCS Hamiltonian) the net current, however, has to vanish so that there is the same amount of pairs with opposite momentum  $-q$ . This leads to a real-valued and spatially modulated order parameter

$$\Delta(q, x) = \Delta_0 \cos(qx). \quad (1.3)$$

The majority spins are located in the nodes of the order parameter in real space (Fig. 1.3). With this configuration, the system can simultaneously realize superfluidity as well as magnetization.

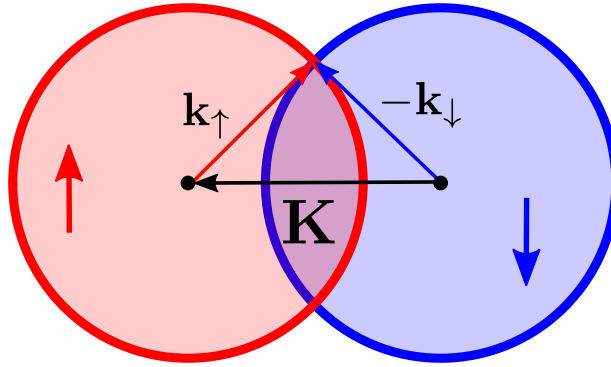


**Figure 1.1.:** Pairing mechanism for a balanced gas. The interaction volume (crossing points of the Fermi surfaces (thick circles)) is maximal for  $\mathbf{K} = 0$ .

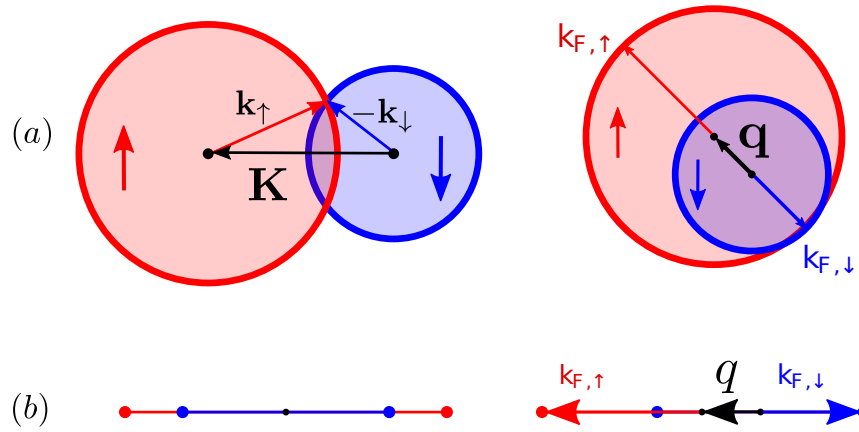


**Figure 1.2.:** (a) Mismatch of Fermi surfaces in 2D (Fermi surfaces are circles) leading to a finite center-of-mass momentum  $\mathbf{q} = \mathbf{k}_{F,\uparrow} - \mathbf{k}_{F,\downarrow}$ . (b) Same situation for 1D (Fermi surfaces are points). The fraction of fermions in the FFLO state is larger for lower dimensions.

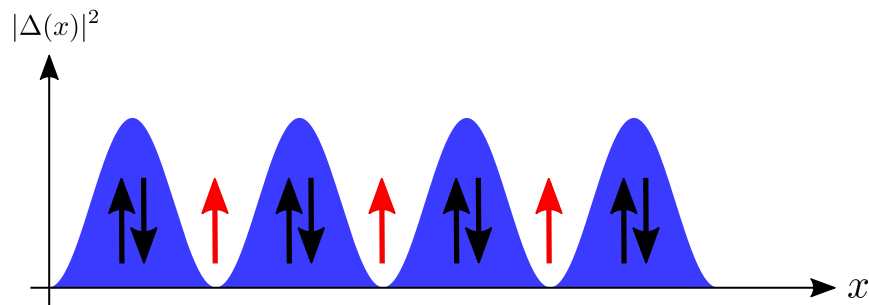


**Figure 1.3.:** Spatial modulated order parameter in the FFLO phase  $\sim |\cos(qx)|^2$ . Excess fermions sit in the nodes.

### 1.1.2. Correlations in FFLO phase

The main feature of the FFLO phase is the special type of correlations, which can be derived by the s-wave pair-pair correlations

$$\rho_{ij}^{\text{pair}} = \langle \hat{c}_{i,\uparrow}^\dagger \hat{c}_{i,\downarrow}^\dagger \hat{c}_{j,\downarrow} \hat{c}_{j,\uparrow} \rangle. \quad (1.4)$$

In the case of a spin-balanced gas, the correlations decay algebraically

$$|\rho_{ij}^{\text{pair}}| \propto \frac{1}{|i-j|^{1/K_c}}, \quad (1.5)$$

with  $K_c$  the charge Luttinger exponent [23].

For spin-imbalanced systems with small polarizations, correlations in Eq. (1.4) can be described by the sine-Gordon theory with a ground state consisting of arrays of domain walls with a change of the superfluid order parameter by  $\pi$  [23, 54]. Going to larger polarizations, the order parameter becomes sinusoidal with a power-law decay

$$|\rho_{ij}^{\text{pair}}| \propto \frac{|\cos(q|i-j|)|}{|i-j|^{\alpha(p)}}. \quad (1.6)$$

In the one-dimensional case, FFLO-type correlations are dominant for arbitrary polarizations  $p$  [8, 54]. The exponent  $\alpha(p)$  is discontinuous in  $p$  [23]. For vanishing polarization, it is given by the inverse Luttinger parameter, whereas for very small but finite polarizations, bosonization yields  $\alpha(p \rightarrow 0^+) = 1/K_c + 1/2$  [23].

In ultracold quantum gases experiments, one almost always probes the momentum distribution function (MDF) of a gas which makes it reasonable to Fourier transform Eq. (1.4) and look at the pair-MDF given by

$$n_k^{\text{pair}} = \frac{1}{L} \sum_{l,m=1}^L e^{ik(l-m)} \rho_{lm}^{\text{pair}} \quad (1.7)$$

with  $k = \frac{2\pi n}{L}$  and  $n = -L/2 + 1, \dots, L/2$  for an even number of sites.

The pairing of the fermions at non-vanishing center-of-mass momentum  $q$  leads to a MDF which is peaked around  $q \neq 0$  and  $-q \neq 0$ . The smoking gun signature of a FFLO phase in 1D experimentally would be the linear scaling of the peak position  $q$  with the polarization  $p$ . The pair momentum distribution function has been calculated using DMRG by Feiguin and Heidrich-Meisner [24], where they showed that for a one-dimensional gas of attractively

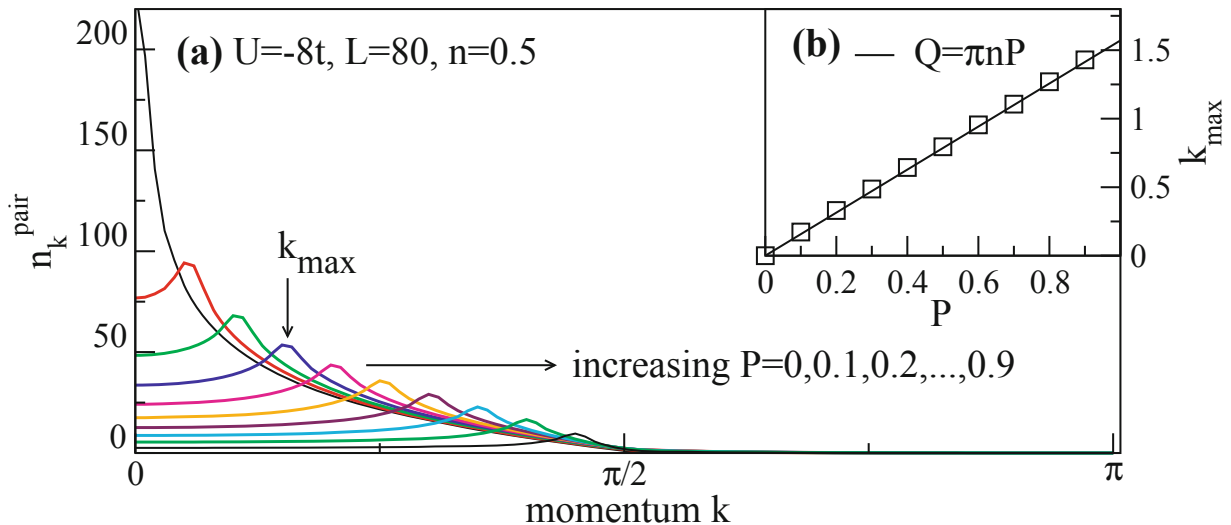


**Figure 1.4.:** FFLO correlations in the pair momentum distribution for attractive fermions in 1D calculated with DMRG simulations. The inset shows the peak position of  $n_k^{\text{pair}}$  as a function of the polarization. The peak position,  $k_{\text{max}}$  scales linearly with the polarization as expected in the FFLO phase. From [24].

interacting fermions in the imbalanced case,  $n_k^{\text{pair}}$  indeed shows FFLO correlations where the position of the peak momentum scales linearly with the polarization as predicted (Fig. 1.4).

### 1.1.3. Realization of the FFLO phase in one dimensional spin-imbalanced gases

In the following, we will outline the main ideas of how the BCS-BEC crossover can be realized in one dimension and we present the model which describes the actual physics of the problem. We first turn to the case of a balanced gas, where the transition from the BCS phase to the BEC phase is described by a smooth crossover. For a more detailed discussion, see [4].

#### Balanced case

The main problem in realizing the BCS-BEC crossover in one dimension is the fact that in two or less dimensions, a bound state is always present at the two-particle level, which in turn is a necessary and sufficient condition for a BCS instability [55]. In fact, the whole notion of a BCS-BEC crossover is not as easy as in three dimensions, as in addition, the BEC consists of tightly bound pairs that behave like hard-core bosons due to the Pauli

exclusion principle of their fermionic constituents. In this case, the bosons form a strongly interacting Tonks-Girardeau gas [56] whereas in 3D, the BEC is weakly repulsive.

However, in a real physical context, the situation never becomes purely 1D but is always quasi-1D, where we have confined the gas in a waveguide geometry with strong transverse confinement. The condition for the strong transverse confinement is that only the lowest eigenmode in the transverse direction is occupied, or put more quantitatively,

$$\varepsilon_F \ll \hbar\omega_\perp \quad \Leftrightarrow \quad nl_\perp \ll 1, \quad (1.8)$$

where  $\varepsilon_F$  is the Fermi energy,  $\omega_\perp$  the frequency of the transverse confinement,  $l_\perp = \sqrt{\frac{\hbar}{m\omega_\perp}}$  the associated oscillator length and  $n$  the density of the system. For this condition, the actual interaction between the fermions can be replaced by a contact interaction in terms of a pseudo-potential  $g_{1D}\delta(x)$  [10]. The system can then be described in terms of the Gaudin-Yang model [17, 18] with the microscopic Hamiltonian

$$H = -\frac{\hbar^2}{2m} \left( \sum_{i=1}^{N_\uparrow} \frac{\partial^2}{\partial x_i^2} + \sum_{i=1}^{N_\downarrow} \frac{\partial^2}{\partial y_i^2} \right) + g_{1D} \sum_i^{N_\uparrow} \sum_j^{N_\downarrow} \delta(x_i - y_j). \quad (1.9)$$

For the contact interaction, the scattering amplitude in the low-energy limit can be written as

$$f(k) \simeq -\frac{1}{1 + ik a_{1D}} \quad (1.10)$$

with the 1D scattering length  $a_{1D} = -\frac{2\hbar^2}{mg_{1D}}$ .

Introducing the dimensionless coupling constant  $\gamma = \frac{mg_{1D}}{\hbar^2 n} = -\frac{\pi}{k_F a_{1D}}$ , which fully characterizes the Hamiltonian Eq. (1.9), we see that the strong coupling regime in one dimension is reached for low densities. In the strong coupling limit,  $k_F a_{1D} \ll 1$ , the system consists of tightly bound molecules due to the attractive interaction. As also mentioned above, the molecules behave as hard-core bosons such that in the BEC limit, the system is described in terms of a Tonks-Girardeau gas in the strictly one-dimensional case.

In the 'real' quasi-1D case, however, the situation is different. Solving the two-body problem in 3D under the condition of strong transverse confinement, Bergeman et al. [34] have shown that for this setup, there is always exactly one bound state present, independent of the 3D scattering length  $a$ . In addition, Olshanii [33] has shown that the low-energy

scattering properties can be described in terms of an effective  $\delta$ -potential with strength

$$g_{1D} = \frac{2\hbar\omega_{\perp}}{1 - Aa/l_{\perp}}, \quad (1.11)$$

with a numerical constant  $A = -\xi(1/2)/\sqrt{2} \simeq 1.0326$ . For a 3D scattering length of  $a = \frac{l_{\perp}}{A}$ , the effective interaction diverges leading to a confinement induced resonance [33], where the 1D scattering length  $a_{1D}$  vanishes. Due to the quasi-1D geometry, the bound state survives the CIR at  $g_{1D} > 0$ , where the  $\delta$ -potential itself does not feature a bound state in 1D. At  $1/\gamma = 0$ , beyond the CIR, the bound state energy  $\varepsilon_b \geq 2\hbar\omega_{\perp}$  is the largest energy scale in the system such that the dimers are essentially unbreakable bosons. Far away from the CIR, the effective interaction between the bosons coincides with the free space result in 3D. Thus one recovers the weakly interacting Bose gas [57].

Thus, for a balanced two-component Fermi gas in a waveguide geometry, we have a full BCS-BEC crossover in one dimension [19, 20]. Up to the CIR, we have a gas of attractively interacting fermions, that can be described in terms of the Gaudin-Yang model. The ground state has a gap in the spin spectrum, which is BCS-like and additional gapless density fluctuations, such that the gas forms a so-called Luther-Emery liquid [58]. Beyond the resonance, the system can be described in terms of the Lieb-Liniger model for repulsive bosons [59]. Right at the resonance, the molecules form a Tonks-Girardeau gas.

### Imbalanced case

The Gaudin-Yang model Eq. (1.9) can also be solved exactly for finite spin-imbalance (finite polarization) using the Bethe ansatz. From the ground state energy  $E(n, s)/L$ , with the density  $n = n_{\uparrow} + n_{\downarrow}$  and the imbalance  $s = n_{\uparrow} - n_{\downarrow}$ , one can calculate the chemical potential and the effective magnetic field

$$\mu = \frac{\partial(E/L)}{\partial n}, \quad (1.12)$$

$$h = \frac{\partial(E/L)}{\partial s}. \quad (1.13)$$

From these equations, one can calculate the phase diagram [21, 22], which is shown in Fig. 1.5. The system exhibits three different phases. For small chemical potential and small magnetic field, the system is in a fully paired phase, where we have a balanced gas of attractively interacting fermions forming Cooper pairs. For large magnetic fields, we have a fully polarized system, consisting of only one fermionic species. In between is the partially

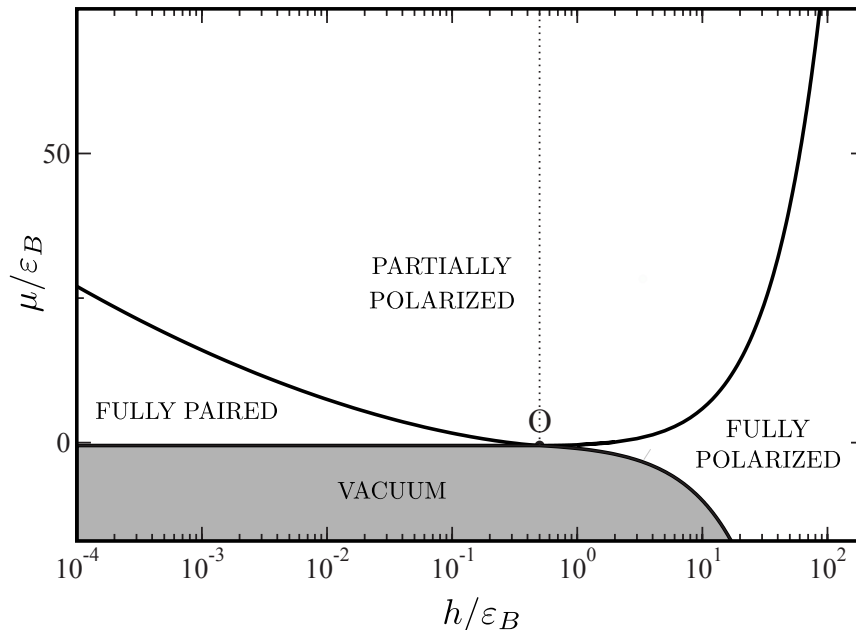


**Figure 1.5.:** Phase diagram for a one-dimensional gas of attractively interacting fermions. From [22]

polarized phase, where we have a spin-imbalanced gas that exhibits FFLO correlations as has been shown using DMRG in [24].

Even though we are dealing with zero temperature throughout this thesis, for the sake of completeness, we mention that effects of finite temperature have also been studied using the thermodynamic Bethe ansatz in [60, 61].

#### 1.1.4. FFLO phase in traps

In experiments, ultracold gases are often confined by means of a harmonic trap. For quasi-one-dimensional systems, the radial confinement (e.g. in  $x$ - and  $y$ -direction) is much larger than in the axial direction ( $z$ -axis) in order to freeze out the radial motion. The weak confinement along the axial direction is then given by a harmonic potential of the form  $V(z) = V_0 z^2$ . Weak trapping potentials, where the spatial variance of the trapping potential is small compared to the local Fermi energy, can be treated in the local density approximation (LDA). Here, one assumes a local chemical potential  $\mu(z)$  given by

$$\mu(z) = \mu_0 - V_0 z^2. \tag{1.14}$$

Now, it is possible to have different phases corresponding to a different chemical potential in the system. As an example, consider the phase diagram in Fig. 1.5 for a 1D system of spin-imbalanced attractive fermions. In LDA, the shell structure above some critical polarization,  $p_c$ , then looks like the following. In the center of the trap, where  $\mu$  is large, one finds a partially polarized phase (possibly with FFLO correlations), whereas in the wings, one finds a fully polarized Fermi gas. For smaller polarizations, or equivalently, smaller magnetic fields, the wings consist of fully paired fermions.

### 1.1.5. Experimental observation

A direct observation of FFLO phases in ultracold gases remains open up to now. However, experiments at Rice University [35] have probed the density profiles of a spin-imbalanced attractive Fermi mixture in an optical trap (Fig. 1.6).

They created an imbalanced mixture of the two lowest hyperfine level of the  ${}^6\text{Li}$  ground state and loaded the atoms into an array of 1D tubes formed with a 2D optical lattice. The system was cooled to  $T = 175$  nK. Further, an external magnetic field was tuned to the BCS side of the Feshbach resonance in  ${}^6\text{Li}$  such that the interaction becomes strongly attractive. The resulting density profile shows a partially polarized core and fully polarized wings above a critical polarization  $p > p_c$  as opposed to the three-dimensional case, where it is the other way round. For polarizations below  $p_c$ , the wings consist of fully paired atoms. However, this detection scheme does not reveal the characteristic FFLO correlations therefore only providing an indirect probe of the FFLO phase.

Other detection schemes for the direct observation of the FFLO phase in condensed matter systems have been proposed and include time-of-flight measurements [36], noise correlations [25] and rf-spectroscopy [38].

## 1.2. Bose-Fermi resonance model

### 1.2.1. BFRM in the continuum

Single-channel models such as the Gaudin-Yang model [17, 18] or the Fermi-Hubbard model suffer from the inability to capture a possible BCS-BEC crossover due to a diverging scattering length at resonance. In order to capture the essence the resonance correctly, one thus has to resort to a two-channel model that not only considers the two fermionic species in the open channel but also incorporates the closed channel bound state. The minimal 1D

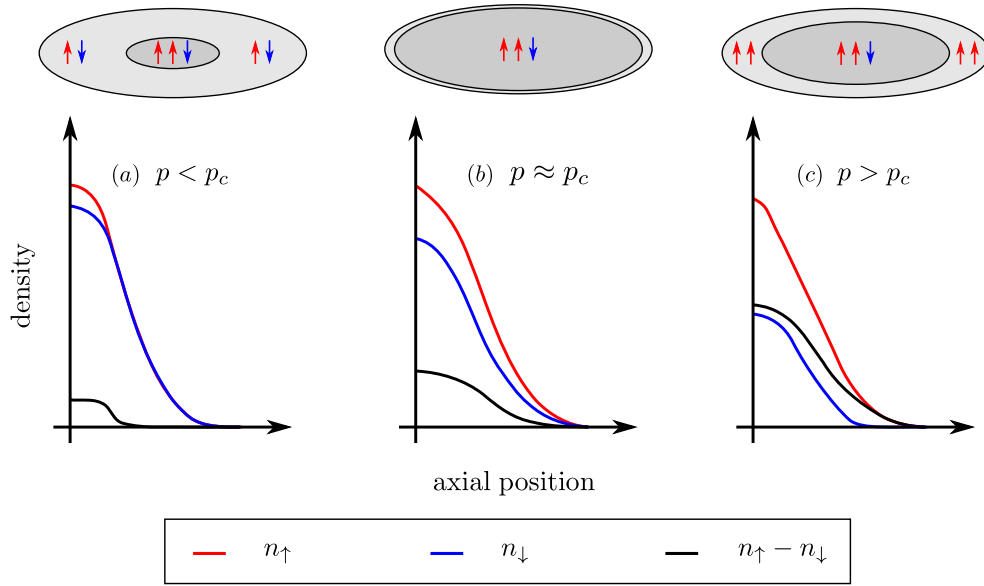


**Figure 1.6.:** Sketch of experimentally probed density profiles in a spin-polarized gas of  ${}^6\text{Li}$  atoms with attractive interactions loaded into a quasi-1D geometry. Black lines denote the density of the majority fermions, blue lines the density of the minority fermions. Red lines indicate the difference. (a) For small polarizations ( $p < p_c$ ), there is a small partially polarized core and unpolarized wings. (b) Near the critical polarization ( $p \approx p_c$ ), almost the whole cloud is partially polarized. (c) Above critical polarization ( $p > p_c$ ), there exists a partially polarized core, while the wings of the cloud are fully polarized.

model capturing such physics typical for a Feshbach resonance is the Bose-Fermi resonance model (BFRM) [39–41]<sup>1</sup>.

$$\begin{aligned}
 H_{\text{BFRM}} = & \int dx \sum_{\sigma} \hat{\psi}_{\sigma}^{\dagger} \left( -\frac{\hbar^2}{2m} \frac{\partial^2}{\partial x^2} \right) \hat{\psi}_{\sigma} + \int dx \hat{\psi}_B^{\dagger} \left( -\frac{\hbar^2}{4m} \frac{\partial^2}{\partial x^2} - \nu \right) \hat{\psi}_B \\
 & + g \int dx \left( \hat{\psi}_B^{\dagger} \hat{\psi}_{\uparrow} \hat{\psi}_{\downarrow} + \text{h.c.} \right).
 \end{aligned} \tag{1.15}$$

$\hat{\psi}_{\sigma}^{(\dagger)}$  and  $\hat{\psi}_B^{(\dagger)}$  are annihilation (creation) operators for fermionic and bosonic fields, respectively. The energy of the bound state consisting of two paired fermions is detuned by some energy  $\nu$  relative to the fermionic state. The last term in Eq. (1.15) denotes the Feshbach coupling term, with coupling constant  $g$ , that converts pairs of fermions into molecules and vice versa.

Due to the Feshbach coupling term, the particle number of both fermionic species is not conserved individually but only the total particle number  $N = N_{\uparrow} + N_{\downarrow} + 2N_{\text{mol}}$ . In addition, the population imbalance  $\Delta N = N_{\uparrow} - N_{\downarrow}$ , or equivalently the polarization  $p = \Delta N/N$ , is conserved.

Note also that we have not included a possible interaction between the fermions that would be of type  $\sim a_{\text{bg}} \hat{\psi}_{\uparrow}^{\dagger} \hat{\psi}_{\downarrow}^{\dagger} \hat{\psi}_{\downarrow} \hat{\psi}_{\uparrow}$ , where  $a_{\text{bg}}$  is the background scattering length. This approximation is reasonable close to the resonance  $\nu \approx 0$ .

For large negative detuning  $\nu$ , we are in the BCS limit where the number of molecules is small or almost zero. The fermions are paired in momentum space and form Cooper pairs due to a weak attractive interaction  $\sim g^2/\nu$ . The opposite case, large positive detuning  $\nu$ , denotes the BEC limit, where we have a condensate of real-space paired fermions with repulsive interaction.

We now want to take a closer look at the origin of this interaction, which can be understood from the following picture (see Fig. 1.7). Assume we are in the BCS limit where the molecular channel is detuned by  $\nu$ , thus having free fermions. If  $g$  is finite, up- and down-fermions at the same point  $x$  in space can make virtual transitions into the molecular state which give rise to an additional energy  $g^2/\nu$ , which also can be seen from second order perturbation theory for  $g \ll 1$ . However, this is not restricted to this limit. On the BEC side, the situation is just inverted. We have real-space pairs of fermions in the molecular state while the fermionic channel is higher in energy. Again, the molecules can break up and make virtual transitions into the unpaired channel provided there is no additional free

<sup>1</sup>Note the difference in the sign of the detuning compared to [41].

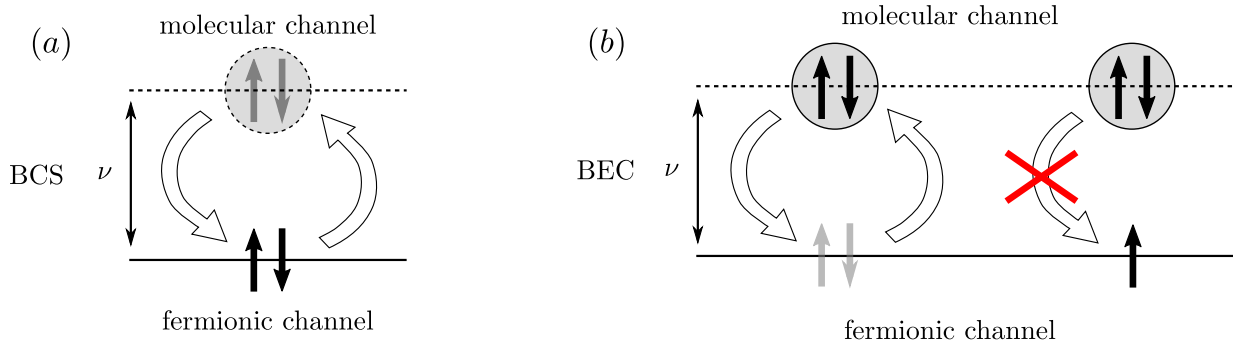


**Figure 1.7.:** Effective interaction in BFRM. (a) On the BCS side, unpaired fermions can make virtual transitions into the molecular state giving rise to an attractive interaction between fermions. (b) On the BEC side, virtual transitions into fermionic channel are only possible if it is not occupied by another fermion. This gives rise to a repulsive interaction.

fermion in this channel already. This leads to a repulsive interaction between molecules and fermions with interaction strength  $\sim g^2/\nu$ .

The weak attractive interaction on the BCS side is important for establishing superconductivity by forming momentum-space paired fermions. As discussed above, in the case of a spin-imbalanced gas this leads to the FFLO phase as will be discussed when looking at the phase diagram for the lattice system in Section 1.2.2.

### Scattering properties

Following [41], we discuss the scattering properties of the BFRM for the two-body problem and calculate the scattering amplitude and the binding-energy of the bound state. To this end, we use the grand-canonical version of Eq. (1.15)

$$\hat{H}_{\text{BFRM}}^{\text{gc}} = \hat{H}_{\text{BFRM}} - \mu \hat{N} \quad (1.16)$$

and set  $\hbar = 1$ .

The scattering process between two fermions in terms of Feynman diagrams is shown in Fig. 1.8. The molecule propagator in momentum space is given by

$$D(k, \omega) = D_0(k, \omega) + D_0(k, \omega) \Pi(k, \omega) D(k, \omega) \quad (1.17)$$

with the bare molecule propagator  $D_0(k, \omega)$  given by

$$D_0(k, \omega) = \frac{1}{\omega - \frac{k^2}{4m} - 2\mu + \nu + i0^+}. \quad (1.18)$$

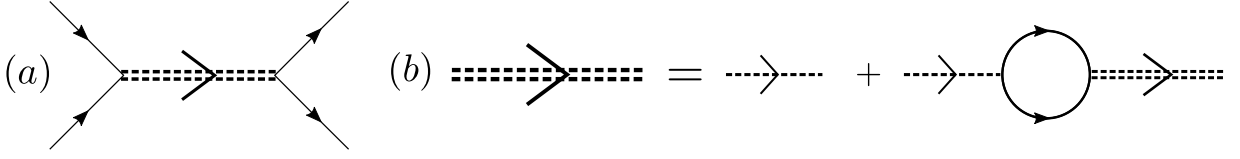


**Figure 1.8.:** (a) Feynman diagram of the scattering process of two fermions forming a molecule. Double dashed line (middle) is the full molecule propagator  $D(k, \omega)$ . (b) Dyson equation for the full molecule propagator. Dashed line denotes the bare molecule propagator  $D_0(k, \omega)$ , the bubble on the right hand side corresponds to the polarization insertion (or self-energy)  $\Pi(k, \omega)$ .

The self-energy  $\Pi$  is given by

$$\Pi(k, \omega) = g^2 \int \frac{dk'}{2\pi} \frac{1}{\omega - \frac{k'^2}{m} - \frac{k^2}{4m} + 2\mu + i0^+}. \quad (1.19)$$

The energy of the bound state is then given by the pole at  $k = 0$  and  $\mu = 0$  of the (full) molecule propagator, which yields

$$\frac{|\varepsilon_b|}{|\varepsilon_\star|} - \sqrt{\frac{|\varepsilon_\star|}{|\varepsilon_b|} - \frac{\nu}{|\varepsilon_\star|}} = 0, \quad (1.20)$$

with an on-resonance bound state energy  $\varepsilon_\star = -m^{1/3}g^{4/3}/2^{2/3}$ . As pointed out in [41], the scattering between two fermions can be described by an effective contact potential with interaction strength

$$\tilde{g} = \frac{g^2}{\nu}, \quad (1.21)$$

which is exactly what we got from the simple picture discussed above. By introducing the size of the bound state at resonance  $r^\star = (m|\varepsilon_\star|/2)^{-1/2}$ , we can define the broad-resonance (or strong-coupling) limit  $nr^\star \ll 1$ . This is equivalent to the condition that the energy of the bound state at resonance is much larger than the Fermi energy. In contrast, a narrow Feshbach resonance is characterized by the condition  $nr^\star \gg 1$ . As discussed by Recati et al. [41], in the broad resonance limit and spin-balanced case, the BFRM is equivalent to the exactly solvable modified Gaudin-Yang model that consists of a Gaudin-Yang model of attractive fermions on the BCS side of the resonance and a Lieb-Liniger model [59] of repulsive dimers on the BEC side. Thus, the BEC-BCS crossover in one dimension is smooth. This changes when a finite imbalance in the spin populations is induced by an external Zeeman field coupling to the spin imbalance,  $-h(\hat{N}_\uparrow - \hat{N}_\downarrow)$ . Baur et al. [29]

have shown in a three-body calculation that at a certain detuning  $\nu > 0$ , the spatially modulated FFLO correlations disappear and ordinary BEC correlations emerge. This change is reflected in the change of the symmetry of the three-body ground state wave function.

### 1.2.2. BFRM on a lattice

In numerical methods like TEBD, we can not treat the BFRM in the continuum but need a spatial discretization. We therefore assume a lattice with  $L$  sites and a lattice spacing of unity. Eq. (1.15) then transforms into

$$\begin{aligned}
 H_{\text{BFRM}} = & -t \sum_{i=1}^{L-1} \sum_{\sigma} \left( \hat{c}_{i,\sigma}^{\dagger} \hat{c}_{i+1,\sigma} + \text{h.c.} \right) - \frac{t}{2} \sum_{i=0}^{L-1} \left( \hat{m}_i \hat{m}_{i+1} + \text{h.c.} \right) \\
 & - (\nu + 3t) \sum_{i=1}^L \hat{m}_i^{\dagger} \hat{m}_i + g \sum_{i=0}^L \left( \hat{m}_i^{\dagger} \hat{c}_{i,\uparrow} \hat{c}_{i,\downarrow} + \text{h.c.} \right). \tag{1.22}
 \end{aligned}$$

We shifted the detuning such that at  $\nu = 0$ , the energy for adding one molecule equals the energy of adding one fermion of each species. Further, we treat the molecules as hard-core bosons allowing at maximum one molecule per site.

In analogy to the discussion of the binding energy in the continuum case, for the lattice case, the calculation has been done in [44] and yields

$$\varepsilon_b - \nu = g^2 \int_{-\pi}^{\pi} \frac{dk}{2\pi} \frac{1}{\varepsilon_b + 4t(1 - \cos k)}. \tag{1.23}$$

The solution of this equation in terms of the dimensionless binding energy  $\Omega = \varepsilon_b/\varepsilon_{\star}$  and the dimensionless detuning  $\nu' = \nu/\varepsilon_{\star}$  is shown in Fig. 1.9 for different values of  $g$ . As can be seen, the dimensionless binding energy is practically independent of  $g$  and approaches  $\Omega = \nu'$  in the BEC limit.

### Phase diagram for imbalanced case

The phase diagram for the imbalanced ( $N_{\uparrow} \neq N_{\downarrow}$ ) case has been mapped out by Heidrich-Meisner et al. [44] using DMRG and characterizing the different phases by the number of molecules present and the type of correlations. For details, we refer to the original paper.

In Fig. 1.10, the polarization-detuning phase diagram for a density of  $n = 0.6$  and a coupling constant  $g = t$  is shown. It exhibits three different phases that are separated

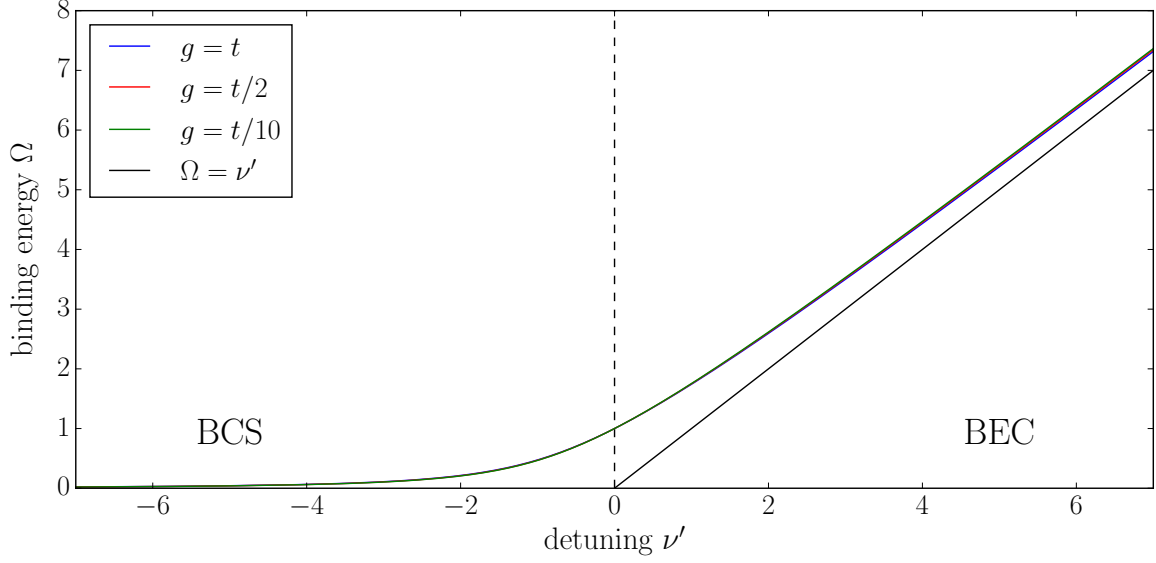


**Figure 1.9.:** Binding energy  $\Omega$  vs. detuning  $\nu'$  from Eq. (1.23) for different  $g$ . Black line gives the asymptotic behaviour  $\Omega = \nu'$  in the BEC regime. Dashed line indicates the resonance. (Reproduced from [44])

by the critical polarizations  $p_1$  and  $p_2$ . Below the critical polarization  $p_1$ , one has pairing at finite momentum both in the pair momentum distribution function as well as in the molecule distribution function (see Fig. 1.11). For  $p_1 < p < p_2$ , additional pairing at zero momentum sets in, which becomes even more pronounced as  $p$  increases.

The critical polarization  $p_2$  denotes the point, where the minority fermions are depleted completely ( $N_\downarrow = 0$ ). This happens below full saturation, where  $N = N_\uparrow$ , and indicates the point when all minority fermions are paired into molecules.

As mentioned above, the 1D BFRM features three different phases in the imbalanced case:

- (i) 1D FLLO: In this phase, the fermions are paired at non-zero momentum as can be seen by the pair momentum distribution function. The phase extends up to the critical polarization  $p_1$  above which the FFLO correlations become more and more suppressed. As indicated also by the inset of Fig. 1.10, the FFLO phase is more robust for small polarizations and low densities.
- (ii) BEC + FP FG: This phase is characterized by molecules that are condensed into BEC, which is immersed in a fully polarized Fermi gas (FP FG). It appears above the critical polarization  $p_2$ .

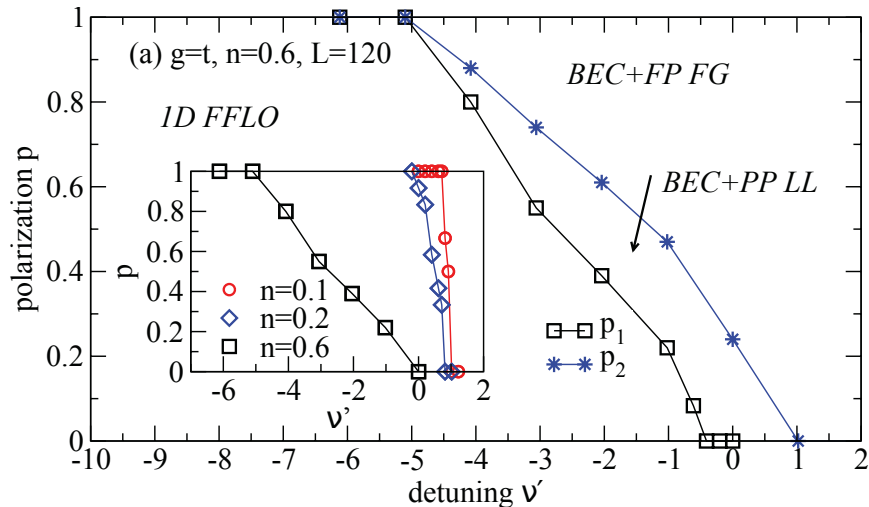


**Figure 1.10.:** Polarization vs. detuning phase diagram for the BFRM model, calculated with DMRG. From [44]

- (iii) BEC + PP LL: For polarizations  $p_1 < p < p_2$ , we have a molecular BEC with pairing at zero momentum coexisting with a partially polarized Luttinger liquid.

The phase diagram depending on a rescaled Zeeman field  $h' = h/\varepsilon_*$  is shown in Fig. 1.12. The critical fields  $h_1$  and  $h_2$  are associated with the critical polarizations  $p_1$  and  $p_2$ , respectively. In addition to that, a saturation field  $h_{\text{sat}}$  occurs, above which the system is fully polarized (FP) and we are left with only one spin species. Further, there is a critical field  $h_c$  that is associated with the spin gap  $\Delta = 2h_c$  of the standard 1D BCS-BEC crossover. For large positive detuning  $\nu' \gg 1$ , the spin gap is directly proportional to the binding energy  $\Delta \propto \nu'$  [44].

### 1.2.3. Experimental observation

As discussed in Section 1.1.5, up to now, there has been no direct observation of FFLO correlations in spin-imbalanced Fermi gases. While in typical time-of-flight measurements in ultra cold gas experiments only the momentum distribution function of each species is probed individually, in addition, FFLO correlations are lost during the free expansion when released from the trap. This is due to a quantum distillation process where the excess fermions are separated from the superfluid pairs [62–64].

However, one possible solution to that problem is to project the momentum distribution function of the pairs on the BCS side of the resonance onto the molecule distribution on the BEC side of the resonance. In spin-balanced gases, this can be done by changing the

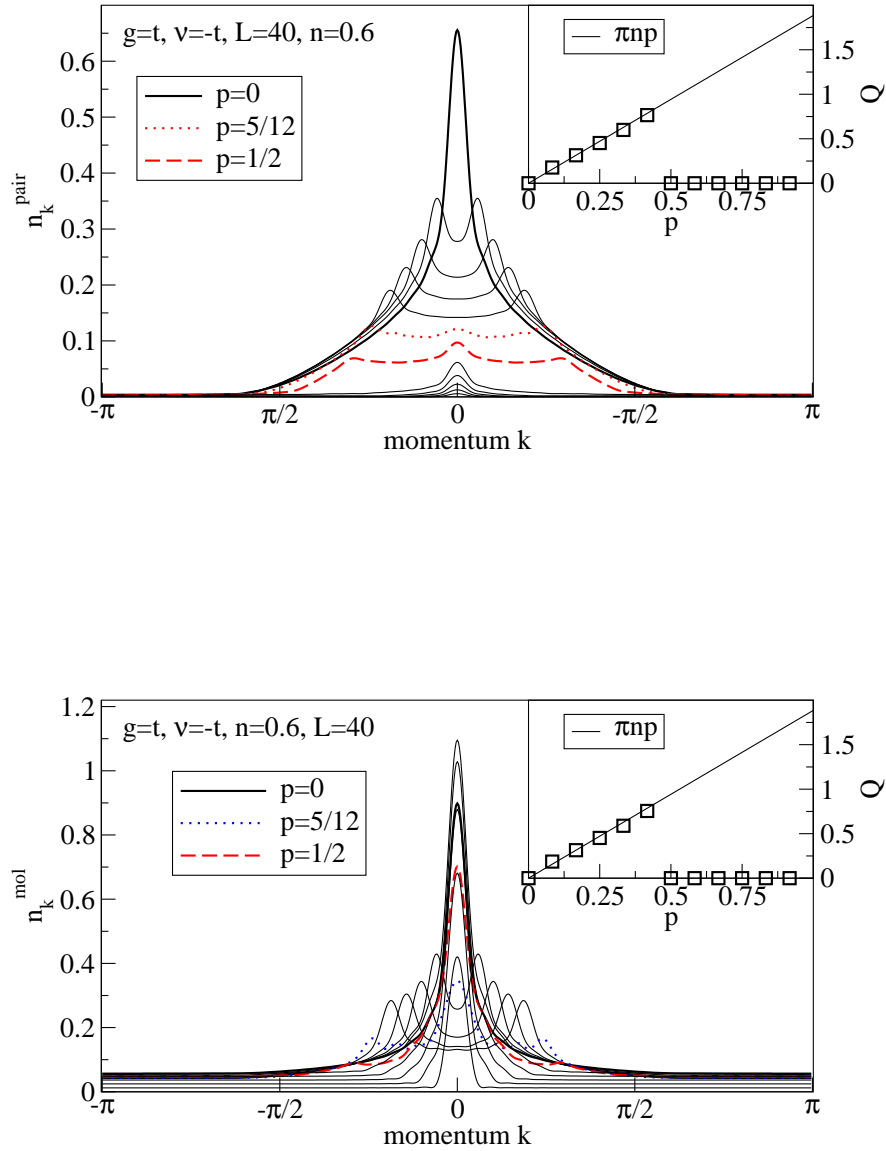


**Figure 1.11.:** (*Top*): Momentum distribution function of pairs for different polarizations. Inset: Peak position  $Q$  versus polarization. (*Bottom*): Momentum distribution function for molecules. From [44].

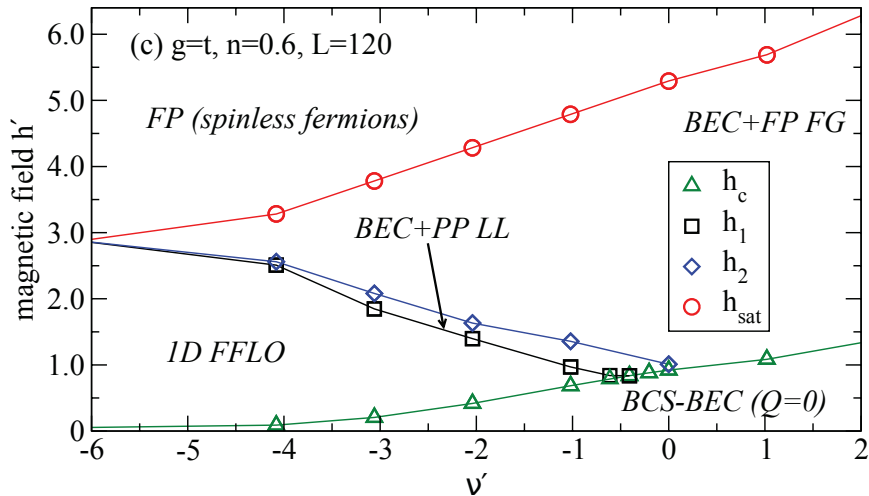


**Figure 1.12.:** Magnetic field vs. detuning phase diagram for the BFRM model, calculated with DMRG. From [44]

interaction from being attractive to being repulsive by ramping over a Feshbach resonance with a magnetic field. The main feature arising for imbalanced gases is, nevertheless, the non-smooth crossover between BCS-phase and BEC-phase as discussed above. Due to phase transitions during the ramp, it is unclear how the ramp has to be performed in order to make the FFLO correlations visible in the momentum distribution function. This question will be discussed in Section 4.1.2.

Having found an optimal ramp protocol for imprinting the FFLO correlations onto the molecules, we have to probe the molecule momentum distribution function after time-of-flight. Therefore, we shortly derive the resulting distribution after some time  $t$  when released from a trap (for details of the calculation see Appendix B).

Assume the molecules to be in a condensate with wave function  $M_0(\mathbf{r})$  initially. The expansion (after removing all sorts of traps) is then given by the Schrödinger equation leading to

$$m(\mathbf{r}, t) = \int \frac{d^3k}{(2\pi)^3} \tilde{M}_0(\mathbf{k}) e^{i\mathbf{k}\cdot\mathbf{r}} e^{-i\frac{\hbar t}{2m}k^2}, \quad (1.24)$$

where

$$\tilde{M}_0(\mathbf{k}) = \int d^3r M_0(\mathbf{r}) e^{-i\mathbf{k}\cdot\mathbf{r}} \quad (1.25)$$

is the Fourier transform of the initial wave function. The molecule density distribution is given by

$$n(\mathbf{r}, t) = \langle \hat{m}^\dagger(\mathbf{r}, t) \hat{m}(\mathbf{r}, t) \rangle \approx m^*(\mathbf{r}, t) m(\mathbf{r}, t). \quad (1.26)$$

For a long time-of-flight expansion, when the size of the cloud is much larger than the initial size, one ends up with

$$n(\mathbf{r}, t) = \left(\frac{m}{2\pi\hbar t}\right)^3 \tilde{M}_0^* \left(\frac{m}{\hbar t} \mathbf{k}\right) \tilde{M}_0 \left(\frac{m}{\hbar t} \mathbf{r}\right) = \left(\frac{m}{2\pi\hbar t}\right)^3 \tilde{n} \left(\mathbf{k} = \frac{m}{\hbar t} \mathbf{r}\right), \quad (1.27)$$

where  $\tilde{n}(\mathbf{k})$  is the initial momentum distribution function of the molecules which is probed in time-of-flight measurements.

For a molecular condensate exhibiting FFLO correlations, the simplest possible wave function is of the form  $M_0(\mathbf{r}) = M_q(\mathbf{r})e^{-iqx}$  for a one dimensional gas.  $M_q(\mathbf{r})$  is given by the trap geometry. For convenience, we take a cigar-shaped trap with some radial confinement (along  $y$ - and  $z$ -axis)  $r_0$  and some axial confinement (along the  $x$ -axis)  $a_0$  with  $r_0 \ll a_0$ . The total wave function then reads (leaving aside normalization factors)

$$M_0(\mathbf{r}) \propto e^{-(y^2+z^2)/2r_0^2} e^{-x^2/2a_0^2} e^{-iqx}. \quad (1.28)$$

Together with Eq. (1.27) we get

$$n(\mathbf{r}, t) = \left(\frac{m}{2\pi\hbar t}\right)^3 \exp\left(-\frac{a_0^2 \left(q - \frac{mx}{\hbar t}\right)^2}{2}\right) \exp\left(-r_0^2(y^2 + z^2) \left(\frac{m}{\hbar t}\right)^2\right). \quad (1.29)$$

The resulting momentum distribution function is thus peaked around  $x = q\hbar t/m$ . In order to observe the peak, the peak width  $\Delta x = \hbar t/(a_0 m)$  has to be small enough ( $x/\Delta x \gg 1$ ), leading to the condition

$$q a_0 \gg 1. \quad (1.30)$$

As  $q \propto p$  in 1D, this means large polarization and weak confinement along the axial direction.



## 2. Quantum Quenches and Slow Ramps: Kibble-Zurek Mechanism

In this chapter, we discuss the behaviour of quantum systems taken out of equilibrium in two different ways. The first one is the so-called quantum quench, which is a sudden change of one parameter of the Hamiltonian. The other one is a slow ramp, where the parameter is changed slowly and continuously in time. In the latter case, we will discuss the situation when ramping across a critical point or a critical region in the phase diagram. For a general review of non-equilibrium dynamics in closed quantum systems, we refer to the Colloquium by Polkovnikov et al. [65] and the review of Eisert et al. [66]. A very good review in the context of the experimental progress in the field of ultracold atoms out of equilibrium is given in [67].

### 2.1. Quantum quenches

A quantum quench is a sudden change of one parameter of the Hamiltonian with a subsequent evolution of the state in time under the new Hamiltonian. To this end, consider a Hamiltonian  $\hat{H}(\lambda)$  with a parameter  $\lambda$  that we are going to change at some time  $t_0 = 0$  from  $\lambda_0$  to  $\lambda_1$ .

$$t < t_0 : \hat{H}_0 = \hat{H}(\lambda_0) \quad \rightarrow \quad t \geq t_0 : \hat{H}_1 = \hat{H}(\lambda_1) \quad (2.1)$$

Before the quench, we assume the system to be in the ground state (or, in general, an eigenstate) of  $\hat{H}_0$

$$\hat{H}_0|\psi_0\rangle = E_0|\psi_0\rangle. \quad (2.2)$$

However, after the quench, the state will not be an eigenstate any longer and the state will evolve under the new Hamiltonian  $\hat{H}_1$ .

The following time evolution can (in principle) be calculated easily provided one knows all

the eigenstates  $|\tilde{E}_i\rangle$  of the new Hamiltonian. In order to see this, we expand the pre-quench state  $|\psi_0\rangle$  in the eigenbasis of  $\hat{H}_1$

$$|\psi_0\rangle = \sum_i c_i |\tilde{E}_i\rangle. \quad (2.3)$$

In this basis, the time evolution under the new Hamiltonian becomes very simple

$$|\psi(t)\rangle = e^{-it\hat{H}_1}|\psi_0\rangle = \sum_i c_i e^{-i\tilde{E}_i t} |\tilde{E}_i\rangle. \quad (2.4)$$

From Eq. (2.4), we see that knowing the eigenbasis of the new Hamiltonian, we can calculate time evolution exactly.

## 2.2. Slow Ramps: Kibble-Zurek mechanism (KZM)

A different situation occurs when one parameter  $\lambda$  of the Hamiltonian is changed continuously in time. The main focus in this thesis lies on the case when this change involves the crossing of a critical point or a critical region in the phase diagram of the system. To this end, we consider ramps of the form

$$\lambda(t) = \lambda_1 + \frac{\lambda_1 - \lambda_0}{\tau_Q} t, \quad (2.5)$$

where  $\lambda_0$  and  $\lambda_1$  are the initial and final parameter, respectively.  $\tau_Q$  denotes the quench rate and is inversely proportional to the velocity  $v$  of the ramp. The control parameter  $\lambda$  has not been specified yet and can in principle be any parameter of the Hamiltonian associated with a (quantum) phase transition.

### 2.2.1. Kibble-Zurek mechanism

The problem of crossing a second-order phase transition at finite velocity was first studied by Kibble [49, 68] in the context of formation of domain structures in the early universe and Zurek, who extended these ideas to condensed matter systems [50, 69, 70]. The main point of the Kibble-Zurek theory is the power-law scaling of key properties like the correlation length or the density of defects introduced in the system, where the scaling exponents of these quantities are given by the equilibrium scaling exponents. In this sense, the KZ theory provides an extension of universality of equilibrium features to its dynamics.

### Adiabatic-Impulse Approximation

Consider a system that is in equilibrium in a disordered phase in the beginning. Now assume that we change the parameter relevant for the phase transition with a finite velocity until reaching the symmetry broken phase (ordered phase). KZM divides the dynamics in three regimes: the quasi-adiabatic regime in the beginning, the near-critical impulse regime, where the dynamics are 'frozen' and again the quasi-adiabatic regime in the end. This is called **adiabatic-impulse approximation**. The argument goes as follows: In the beginning, far away from the transition, the system behaves nearly adiabatic having some kind of relaxation time towards its equilibrium state. Approaching the critical point, the relaxation time diverges and the system cannot equilibrate any longer. In this sense, the dynamics is frozen, meaning that remote regions of the system are causally disconnected. One example would be cooling down a paramagnet into a ferromagnetic state. When the temperature is changed with a finite velocity, the magnetization will take different values in different regions of the system (see Fig. 2.1). Having crossed the critical point and leaving the near-critical regime, the system again behaves adiabatically, meaning that the regions will not change the values of the order parameter. Thus, we have created defects (or domain walls) in the system. KZM now provides scaling laws for the size of those domains or, equivalently, the density of defects in the system in terms of the velocity with which the phase transition has been crossed.

Even though KZM first was discussed for classical phase transitions, where the transition is controlled by temperature, it has been shown in [51] that it also applies to quantum phase transitions where the symmetry breaking is mediated by some other control parameter  $\lambda$ . For this kind of phase transition, we will derive the scaling laws of some properties and discuss the quantum Ising model as an example.

### Quantum Phase Transitions and KZM

Quantum phase transitions are defined as points of non-analyticity of the ground state energy  $E_0$  in terms of some control parameter  $\lambda$  for some system in the thermodynamic limit. This change usually comes along with a qualitative change of the nature of the correlations of the ground state. In this sense, quantum phase transitions only appear at zero temperature. Examples for quantum phase transitions are the paramagnetic to ferromagnetic transition in the quantum Ising model or the Mott-Insulator to superfluid transition in the Bose-Hubbard-Model. For second order phase transitions, there is a gap  $\Delta$  between the ground state and the first excited state which vanishes at the critical point  $\lambda_c$ .

For the case of gapless systems,  $\Delta$  is associated with the scale at which there is a qualitative change in the spectrum from low frequency to high frequency behaviour [71]. The scaling of the gap as one approaches the critical point  $\lambda_c$ , is given by

$$\Delta \sim |\lambda_c - \lambda|^{z\nu}, \quad (2.6)$$

where  $z\nu$  is the universal critical exponent, which is mostly independent of the microscopic details of the Hamiltonian. Eq. (2.6) holds on both sides of the transition ( $\lambda < \lambda_c$  and  $\lambda > \lambda_c$ ), while the prefactors in general can be different. In addition, the scaling of the correlation length near the critical point is given by

$$\xi \sim |\lambda_c - \lambda|^{-\nu}. \quad (2.7)$$

Eq. (2.6) and Eq. (2.7) provide the key ingredients for the derivation of the non-equilibrium scaling laws within Kibble-Zurek theory. To this end, let us take a more detailed look at the different regimes of the adiabatic-impulse approximation discussed above. To this end, we assume that the phase transition happens at a single critical point  $\lambda_c$  and the temporal change of the control parameter is given by

$$\lambda(t) = \lambda_c + \frac{t}{\tau_Q}, \quad t \in [-\tau_Q, \tau_Q]. \quad (2.8)$$

Here  $\tau_Q$  denotes the quench or ramp time and time is chosen such that  $t = 0$  coincides with crossing the critical point <sup>1</sup>.

**Quasi-adiabatic regime** Far away from the critical point, we consider a system, where the ground state is protected by some finite gap  $\Delta > 0$ . This gap sets a time scale for the relaxation to equilibrium, given by

$$\tau \sim \frac{1}{\Delta} \sim |\lambda - \lambda_c|^{-z\nu} = \left(\frac{|t|}{\tau_Q}\right)^{-z\nu}. \quad (2.9)$$

As long as we are far away from the critical point ( $t \ll 0$ ), the relaxation time is small and the adiabatic approximation holds. This can also be quantified by the following condition

$$\dot{\Delta} \ll \Delta^2. \quad (2.10)$$

---

<sup>1</sup>The difference to Eq. (2.5) is only in order to make the derivation clearer.

In this case, the system always remains in its respective ground state and no excitations are possible.

**Breakdown of adiabaticity** However, as we approach the critical point, at some point  $\lambda_Z$  the adiabatic approximation (Eq. (2.10)) no longer holds and the relaxation time of the system gets larger than the time  $t$  until we reach the critical point. Putting together Eq. (2.6) and Eq. (2.10), we get a scaling relation for the distance between the breakdown of adiabaticity at  $\lambda_Z$  and the critical point  $\lambda_c$ ,

$$|\lambda_Z - \lambda_c| \sim \tau_Q^{-\frac{1}{1+z\nu}}. \quad (2.11)$$

From this moment on, we consider the time evolution to be 'frozen' in the sense that it is restricted to spatial domains of the system. Sufficiently remote regions are causally disconnected and long-range correlations cannot be established any longer. One often refers to this as the impulse regime.

When crossing the critical point at  $t = 0$ , the order parameter associated with the symmetry breaking can take different values in different parts of the system, hence creating defects like kinks in a magnetic system or vortices in a superfluid. The density of these defects can be estimated by the final correlation length. As the dynamics is said to be frozen, making use of Eq. (2.7) and Eq. (2.11), we can derive the scaling of the final correlation length

$$\xi_{\text{final}} \sim \tau_Q^{\frac{\nu}{1+z\nu}}. \quad (2.12)$$

At the same time, this gives the average distance between defects in the system. As a result, for one-dimensional systems, the density of excitations (e.g. kinks or vortices) in the system is

$$n_{\text{ex}} \propto \frac{1}{\xi_{\text{final}}} \sim \tau_Q^{-\frac{\nu}{1+z\nu}}. \quad (2.13)$$

Far away in the symmetry broken phase, the adiabatic approximation again holds.

The boundaries of the frozen dynamics regime can be derived from Zurek's equation

$$\tau(\hat{t}) = \hat{t}. \quad (2.14)$$

This is represented in Fig. 2.1.

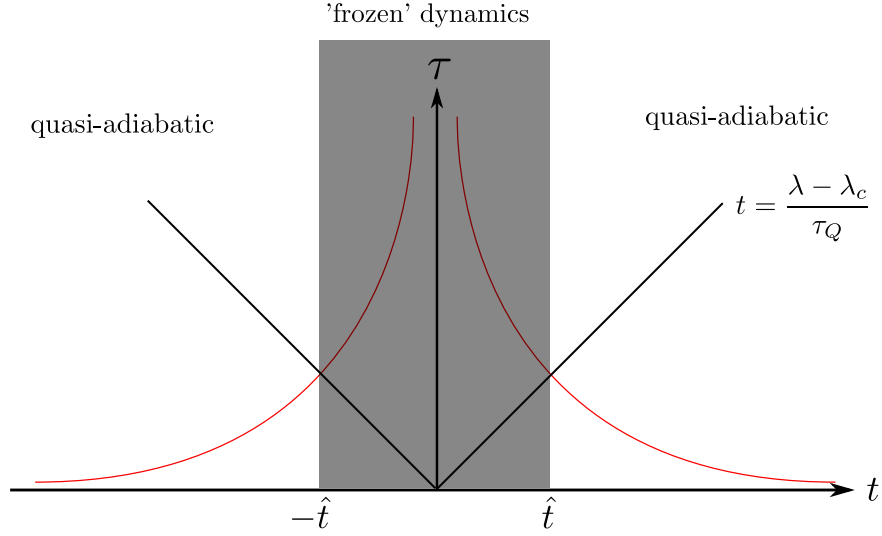


**Figure 2.1.:** Schematic view of the different regimes in KZ theory. In the grey shaded region, the dynamics can be considered 'frozen'. This is when the relaxation time  $\tau$  is larger than the time until reaching  $\lambda_c$ . The boundaries can be calculated by  $\tau(\hat{t}) = \hat{t}$ .

### Example: Quantum Ising Model in $d = 1$

As an illustrative example we want to shortly discuss the quantum Ising model with the Hamiltonian

$$\hat{H} = -\lambda(t) \sum_i \hat{\sigma}_i^x - \sum_i \hat{\sigma}_i^z \hat{\sigma}_{i+1}^z. \quad (2.15)$$

This model has two different phases:

$\lambda > 1$ : paramagnetic phase (disordered)

$0 \leq \lambda < 1$ : ferromagnetic phase (ordered),

with a critical point at  $\lambda_c = 1$ . For an infinite system ( $L \rightarrow \infty$ ), the gap is given by

$$\Delta = 2|\lambda - 1|, \quad (2.16)$$

so that  $z\nu = 1$ . The corresponding relaxation time reads

$$\tau = \frac{\tau_0}{|\lambda - 1|}. \quad (2.17)$$

The correlation length of the system is inversely proportional to the gap,  $\xi \propto |\lambda - 1|^{-1}$ , so that  $\nu = 1$  and  $z = 1$ . In the following, we use a ramp protocol  $\lambda(t)$  as in Eq. (2.8). In

order to get the boundaries of the three different regimes (quasi-adiabatic, impulse like, quasi-adiabatic), we use Zurek's equation Eq. (2.14)

$$\tau(\hat{t}) = \hat{t} \quad \Rightarrow \quad \frac{\tau_0 \tau_Q}{\hat{t}} = \hat{t} \quad \Rightarrow \quad \hat{t} = \sqrt{\tau_0 \tau_Q}. \quad (2.18)$$

The density of defects is given by

$$n_{\text{ex}} \propto \frac{1}{\xi} \propto \frac{1}{\sqrt{\tau_Q}}. \quad (2.19)$$

This result has been verified numerically in [51].

### Analogy to Landau-Zener Transitions

Even though it was shown that the (classical) approach of Kibble and Zurek to the non-equilibrium dynamics for slow ramps can be extended to quantum systems, the discussion was not really quantum mechanical. However, the Landau-Zener (LZ) theory of avoided level crossing provides a quantum mechanical analogue to the discussions above [72, 73].

The most intuitive way of looking at this is to investigate a generic two-level system, which has an avoided level-crossing at some value  $\lambda_c$  of some coupling parameter of the Hamiltonian, which leads to a finite gap  $\Delta$  (see Fig. 2.2). When ramping across this point with some ramp time  $\tau_Q$ , the probability of getting excited (ending up in  $|1\rangle$ ) is given by the Landau-Zener formula [74, 75]

$$p_{\text{ex}} = e^{-\gamma \tau_Q \Delta^2}, \quad (2.20)$$

where  $\gamma$  is a constant. From this formula it is clear that slow ramps ( $\tau_Q \rightarrow \infty$ ) lead to adiabatic behaviour in the sense that the system never gets excited. Obviously, this is only true in the case of a  $\Delta$  being finite which often is the case in finite systems. For a vanishing gap, the evolution fails to be adiabatic as the excitation probability always is one.

Remarkably, for the quantum Ising model discussed above, the scaling for the density of defects in both approaches (KZM and LZ) was shown to be equal [73].

### Kibble-Zurek physics in experiments

Experimentally, in the context of ultracold quantum gases, the physics of the Kibble-Zurek mechanism has been observed in various experiments involving atomic Bose-Einstein

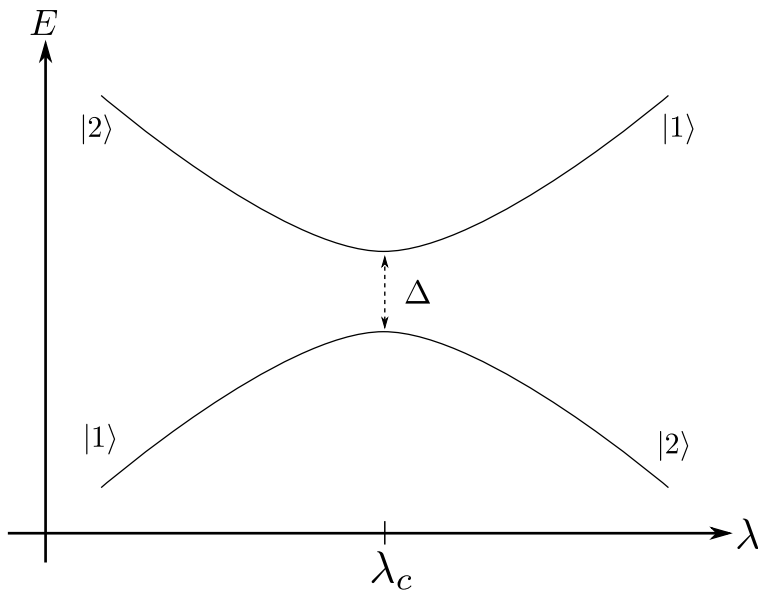


**Figure 2.2.:** Avoided level crossing at  $\lambda_c$

condensates [76–82]. Quite recently, Braun et al. [83] have shown Kibble-Zurek scaling for the coherence length for a certain range of ramp times in the Mott insulator to superfluid transition. However, many experiments lack of direct comparison with Eq. (2.13) as the systems are for example not perfectly homogeneous. For a review about Kibble-Zurek physics in experiments, see [84].

### 2.2.2. Beyond the Kibble-Zurek mechanism

The main assumption of the Kibble-Zurek mechanism is the existence of two gapped phases that are separated by a critical point, where the gap closes. However, many systems have not gapped phases but gapless excitations such as sound modes in weakly interacting superfluids or magnon and spin-wave excitation in magnets. Especially in low-dimensional systems, low-energy excitations can be easily created due to the increasing quantum fluctuations and the large density of states at low energy in low dimensions. The possibility of non-adiabatic scaling in such low-dimensional gapless systems scaling has been discussed in [85] (see also [86] for a connection to ultracold gases).

Signatures of non-adiabatic scaling in the sense of the Kibble-Zurek mechanism for slow ramps over an extended critical region have been observed in numerical studies of the  $XXZ$ -model by Pellegrini et al. [87]. Interestingly, they observed deviations in the scaling exponent when the ramp started in the critical region as well as the emergence of a dominant

critical point during the ramp.

Deng et al. [88] showed, using the anisotropic  $XY$ -model in a transverse alternating field, that multiple level crossings within a gapless phase can completely suppress excitations.



# 3. Matrix Product States and Time Evolving Block Decimation

In order to perform numerical simulations, we use the so-called Matrix Product States (MPS) (for a review see [89]), which is a class of quantum states that can be used to efficiently represent slightly entangled states in one-dimensional quantum systems. With MPS it is also possible to approximate the real- or imaginary-time evolution of a system where we use the Time Evolving Block Decimation (TEBD) algorithm originally proposed by Vidal [47, 48]. Vidal also proposed an extension to systems in the thermodynamic limit, the infinite TEBD (iTEBD) [90], which we will discuss in Section 3.6. The following discussion will be closely related to the review by Schollwöck and the original papers of Vidal. We will also present a rather detailed discussion of implementing and making use of Abelian conserved quantities (good quantum numbers) in the TEBD framework.

## 3.1. Singular value decomposition and Schmidt decomposition

The key ingredient in TEBD is the singular value decomposition (SVD) which decomposes an arbitrary (rectangular) matrix  $M$  with dimensions  $N_A$  and  $N_B$  into

$$M = USV^\dagger. \tag{3.1}$$

Here,  $U$  (of dimension  $N_A \times \min(N_A, N_B)$ ) has orthonormal columns, so that  $U^\dagger U = I$ , whereas  $V$  (of dimension  $\min(N_A, N_B) \times N_B$ ) has orthonormal rows, so that  $VV^\dagger = I$ . The central matrix  $S = \text{diag}(s_1, s_2, \dots, s_r, 0, \dots)$  is diagonal and the non-negative elements  $s_i$  are called the singular values of  $M$ . The number of non-zero elements will play a crucial role in the truncation step introduced later.

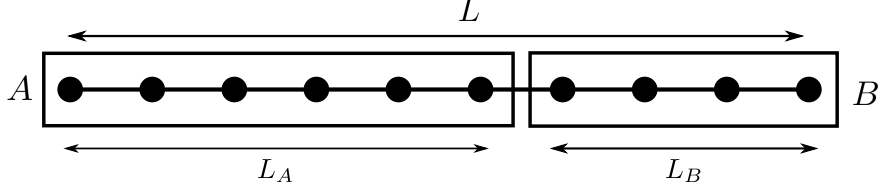


**Figure 3.1.:** Decomposition of a system of length  $L$  into two subsystems  $A$  and  $B$  with length  $L_A$  and  $L_B$  respectively

Assume now a pure quantum state of a system decomposed into two parts  $A$  and  $B$  (see Fig. 3.1)

$$|\psi\rangle = \sum_{i,j} c_{i,j} |i\rangle_A |j\rangle_B \quad (3.2)$$

with  $\{|i\rangle_A\}$  and  $\{|j\rangle_B\}$  orthonormal bases of the subsystems  $A$  and  $B$  that have dimensions  $N_A$  and  $N_B$ . Performing a SVD on the matrix  $c_{i,j}$  we get

$$|\psi\rangle = \sum_{i,j} \sum_{\alpha=1}^r U_{i,\alpha} S_{\alpha,\alpha} (V^\dagger)_{\alpha,j} |i\rangle_A |j\rangle_B = \sum_{\alpha=1}^r s_\alpha |\alpha\rangle_A |\alpha\rangle_B, \quad (3.3)$$

where we defined new basis states  $|\alpha\rangle_A = \sum_i U_{i,\alpha} |i\rangle_A$  and  $|\alpha\rangle_B = \sum_j (V^\dagger)_{\alpha,j} |j\rangle_B$ . The representation Eq. (3.3) is called the Schmidt decomposition of rank  $r$ . In the case of  $r = 1$ ,  $|\psi\rangle$  is a product state and for  $r > 1$ ,  $|\psi\rangle$  is an entangled state.

Usually, for arbitrary quantum states,  $r$  can become exponentially large which makes the numerical implementation inefficient. However, we can try to approximate the state  $|\psi\rangle$  by another state

$$|\tilde{\psi}\rangle = \sum_{\alpha=1}^D s_\alpha |\alpha\rangle_A |\alpha\rangle_B, \quad (3.4)$$

with  $D < r$ . To this end, consider the reduced density matrix  $\rho_A = \text{Tr}_B \rho$  of subsystem  $A$  where  $\rho = |\psi\rangle\langle\psi|$ . Using the Schmidt decomposition Eq. (3.3) we obtain

$$\rho_A = \sum_{\alpha=1}^r s_\alpha^2 |\alpha\rangle_A \langle\alpha|_A. \quad (3.5)$$

Analogously, for the state  $|\tilde{\psi}\rangle$  we get

$$\rho_A = \sum_{\alpha=1}^D s_\alpha^2 |\alpha\rangle_A \langle\alpha|_A. \quad (3.6)$$

The error introduced by approximating the state  $|\psi\rangle$  with the state  $|\tilde{\psi}\rangle$  is then given by

$$\| |\psi\rangle - |\tilde{\psi}\rangle \|_2^2 = \varepsilon = \sum_{\alpha=D+1}^r s_\alpha^2 = 1 - \sum_{\alpha=1}^D s_\alpha^2, \quad (3.7)$$

where  $\|\cdot\|_2^2$  is the so-called 2-norm.

The question that arises by looking at this equation is how big or small one can choose  $D$  in order to still have an accurate description of the original state. If the spectrum of the reduced density matrix decays fast enough which is the case for short-ranged Hamiltonians in one dimension, it is possible to choose  $D$  on the order of just a few hundred or a few thousand kept states without being too inaccurate. In the implementation used in this thesis,  $D$  is defined implicitly by defining a maximum discarded weight  $\varepsilon_{\max} = 10^{-8}$  in order to choose always the optimal  $D$ . In addition, there also will be a maximum value of  $D$  in order to prevent exponential growth.

## Entanglement

There is a very profound connection between entanglement and DMRG or MPS. Calculating the entanglement entropy for a bipartition of a system as in Fig. 3.1, from Eq. (3.5) we get

$$S_{AB} = -\text{Tr}_A \rho_A \log_2 \rho_A = -\sum_{\alpha=1}^r s_\alpha^2 \log_2 s_\alpha^2. \quad (3.8)$$

Area laws predict that the entanglement entropy of the ground state for a system of size  $L$  in  $\mathcal{D}$  dimensions grows like  $S_{AB} \sim L^{\mathcal{D}-1}$  for gapped and short-ranged Hamiltonians [91]. Thus, for a one dimensional system, the entanglement entropy of the ground state is constant and independent of the system size. In this case, the truncation introduced above is indeed possible as in the worst case,  $D \sim e^S = \text{const.}$  For critical points of the system, we get logarithmic corrections of the form  $S = \frac{c}{6} \log_2 L + \text{const.}$ , where  $c$  is the so-called central charge accounting for the number of gapless excitations in the system. Here, we have  $D \sim L$  at worst.

As we also want to perform time-dependent simulations, we are interested in the possible growth of entanglement during an out-of-equilibrium time-evolution of the system. Following the Lieb-Robinson theorem [92], in global quantum quenches, the entanglement of the system grows linearly in time

$$S(t) = S(0) + vt \quad (3.9)$$

where  $v$  is the velocity of an excitation propagating through the system. Thus, it can be argued that in this case  $D$  grows exponentially in time,  $D(t) \sim 2^t$ . This exponential growth of  $D$  is the reason why tensor network methods like TEBD cannot go to arbitrarily long times. In Section 3.7.1, we will encounter an example for this with the time evolution of a system after a quantum quench.

## 3.2. Matrix Product States (MPS)

As the TEBD algorithm is completely formulated in the language of MPS we shortly introduce how we can express an arbitrary pure state in terms of MPS. To this end, consider a one-dimensional lattice of size  $L$  where each site  $i$  has a local  $d$ -dimensional Hilbert space  $\mathcal{H}_i$  with basis  $\{|\sigma_i\rangle\}$ . Then the whole Hilbert space  $\mathcal{H} = \otimes_i \mathcal{H}_i$  has dimension  $d^L$  with basis states  $\{|\sigma_1, \sigma_2, \dots, \sigma_L\rangle\}$ . As shorthand notation, we introduce  $|\sigma_1, \dots, \sigma_L\rangle \equiv |\boldsymbol{\sigma}\rangle$ .

With this notation, an arbitrary quantum state  $|\psi\rangle$  can be written as

$$|\psi\rangle = \sum_{\boldsymbol{\sigma}} c_{\boldsymbol{\sigma}} |\boldsymbol{\sigma}\rangle, \quad (3.10)$$

where we consider  $c_{\boldsymbol{\sigma}}$  as a matrix with  $d^L$  elements. Decomposing this state into MPS (for details see [89]) we arrive at the general form

$$|\psi\rangle = \sum_{\sigma_1, \dots, \sigma_L} M^{\sigma_1} \dots M^{\sigma_L} |\sigma_1, \dots, \sigma_L\rangle \quad (3.11)$$

where  $M^{\sigma_i} = M_{a_{i-1}, a_i}^{\sigma_i}$  is a local tensor belonging to site  $i$ . Throughout this thesis, unlike otherwise stated, we always imply matrix multiplication in expressions like Eq. (3.11). In order to be consistent, we assign dummy indices 1 to the first and last tensor, so that on site 1 we have  $M_{1, a_1}^{\sigma_1}$  and on site  $L$  we have  $M_{a_{L-1}, 1}^{\sigma_L}$ , respectively. In Eq. (3.11), we assumed open boundary conditions, which will be done throughout the thesis unlike otherwise stated.

There exists a very beautiful graphical representation of MPS which illustrates all the basic concepts and will prove very useful for the case of conserved quantities in the system. In Fig. 3.2, the tensors occurring in Eq. (3.11) are represented graphically. Vertical lines correspond to the physical indices  $\sigma_i$  and horizontal lines to the auxiliary bond indices  $a_i$ . We also impose the rule that we contract over connected lines. The MPS in Eq. (3.11) can thus be represented as shown in Fig. 3.3.

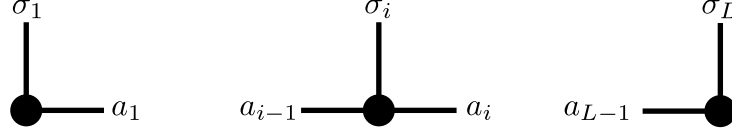


**Figure 3.2.:** Graphical representation of the tensors in MPS. Vertical lines correspond to physical indices and horizontal lines correspond to bond indices. At the edges (left and right images) each tensor has only two legs sticking out due to the open boundary conditions.

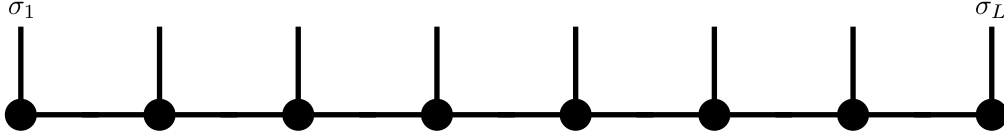


**Figure 3.3.:** Graphical representation of an MPS. The rule is that connected legs are summed over.

### 3.2.1. Examples

**a) Product State** Consider the state  $|\psi\rangle = |\uparrow\downarrow\rangle$  where we have one spin pointing up at site 1 and one spin pointing down on site 2. The MPS representation of this state is very simple

$$M^{\uparrow 1} = 1, M^{\downarrow 1} = 0, M^{\uparrow 2} = 0, M^{\downarrow 2} = 1. \quad (3.12)$$

As  $|\psi\rangle$  is a product state, the matrices all have dimension  $1 \times 1$  and are thus scalars.

**b) Entangled State** Consider the entangled state  $|\psi\rangle \propto |\downarrow\uparrow\rangle + |\uparrow\downarrow\rangle$  leaving aside normalization for the moment. In order to express this state as an MPS, we have the following conditions for the coefficients  $M^{\sigma_i}$ .

$$M^{\downarrow 1} M^{\downarrow 2} = 0, M^{\uparrow 1} M^{\uparrow 2} = 0, M^{\uparrow 1} M^{\downarrow 2} = 1, M^{\downarrow 1} M^{\uparrow 2} = 1 \quad (3.13)$$

Obviously, these conditions cannot be satisfied by simple scalars. Instead, we have

$$M^{\downarrow 1} = \begin{pmatrix} 1 & 0 \end{pmatrix}, M^{\uparrow 1} = \begin{pmatrix} 0 & 1 \end{pmatrix}, M^{\downarrow 2} = \begin{pmatrix} 0 \\ 1 \end{pmatrix}, M^{\uparrow 2} = \begin{pmatrix} 1 \\ 0 \end{pmatrix} \quad (3.14)$$

Now, the coefficients of the MPS are not scalars anymore but vectors of dimension  $1 \times 2$  and  $2 \times 1$  respectively. This is due to the fact that  $|\psi\rangle$  is entangled.

### 3.2.2. Normalization

Up to now, we have not imposed any normalization condition onto the MPS in Eq. (3.11). Therefore, we rename all  $M$  matrices  $B$  and impose the following (right) normalization condition

$$\sum_{\sigma_i} B^{\sigma_i} B^{\sigma_i \dagger} = I. \quad (3.15)$$

Similarly, we can use the (left) normalization condition

$$\sum_{\sigma_i} A^{\sigma_i \dagger} A^{\sigma_i} = I, \quad (3.16)$$

where we renamed  $M \rightarrow A$ . An MPS only consisting of tensors obeying Eq. (3.15) is called right canonical, whereas an MPS consisting of tensors obeying Eq. (3.16) is called left canonical.

A mixed canonical MPS has one site  $i$  for which all tensors on the left are left canonical and all tensors on the right are right canonical. Another very useful representation is the Vidal representation (see Section 3.4.2) which can be transformed into either of the above three representations.

### 3.2.3. Calculation of expectation values and correlations

As we are interested in physical quantities of our systems, we have to calculate local expectation values  $\langle \psi | \hat{O}_i | \psi \rangle$  or in some cases correlations of the form  $\langle \psi | \hat{O}_i \hat{O}_j | \psi \rangle$ . With the help of the graphical representation introduced above, we can nicely express these operations. At first, we write an operator  $\hat{O}$  in the local basis

$$\hat{O}_i = \sum_{\sigma_i, \sigma'_i} O^{\sigma_i, \sigma'_i} |\sigma_i\rangle \langle \sigma'_i|. \quad (3.17)$$

Then the graphical representation of expectation values and correlations is given as in Fig. 3.4. The square box denotes the operator acting on a single site.

## 3.3. Matrix Product Operators (MPO)

The concept of decomposing an arbitrary quantum state into an MPS can also be considered for operators that not necessarily have to be local. Consider a general (non-local) operator

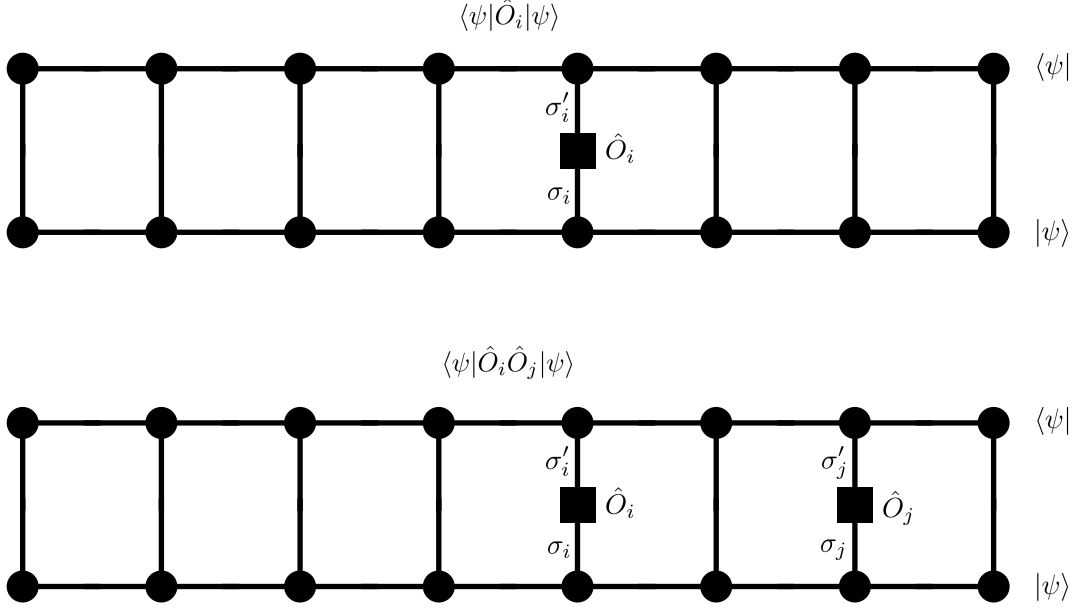


**Figure 3.4.:** Graphical representation of a local expectation value (top) and correlator (bottom) for an MPS

$\hat{O}$  (e.g. Hamiltonian,...) which can be decomposed into an MPO

$$\hat{O} = \sum_{\sigma, \sigma'} W^{\sigma_1, \sigma'_1} \dots W^{\sigma_L, \sigma'_L} |\sigma\rangle \langle \sigma'|. \quad (3.18)$$

For non-local operators like Hamiltonians,  $W^{\sigma_i, \sigma'_i}$  will in general be matrices. However, for local operators like  $\hat{O}_i$  they will be scalars and except for site  $i$ , they will be unity.

As for MPS, any operator can be decomposed into an MPO with a certain bond dimension  $D_W$ . In addition, there exists a similar graphical representation (see Fig. 3.5), that we will make use of in the case of conserved quantities (see Section 3.5).

### Example

To put the concept of MPO to a more practical aspect, consider the following Bose-Hubbard Hamiltonian

$$\hat{H} = -t \sum_{i=1}^{L-1} (\hat{b}_i^\dagger \hat{b}_{i+1} + \text{h.c.}) + U \sum_{i=1}^L \hat{n}_i (\hat{n}_i - 1). \quad (3.19)$$

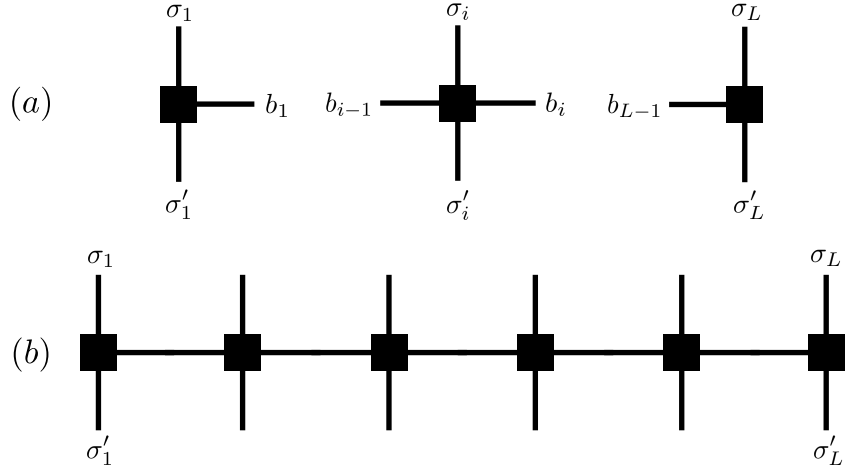


**Figure 3.5.:** Graphical representation of an MPO. (a): Basic tensors for the MPO. In general, each tensor has bond indices  $b_i$  like MPS. (b): Complete representation of MPO. The connected legs indicate summation over these indices.

Here,  $\hat{b}_i^{(\dagger)}$  denotes the bosonic annihilation (creation) operator on site  $i$  and  $\hat{n}_i = \hat{b}_i^\dagger \hat{b}_i$  counts the number of particles at site  $i$ . Formally, one should write

$$\hat{H} = -t \hat{b}_1^\dagger \otimes \hat{b}_2 \otimes \hat{I} \otimes \hat{I} \otimes \cdots \otimes \hat{I} - t \hat{I} \otimes \hat{b}_2^\dagger \otimes \hat{b}_3 \otimes \hat{I} \otimes \cdots \otimes \hat{I} + \cdots \quad (3.20)$$

Going through the chain, we encounter four different scenarios. In the first scenario, we only have identity operators on the right of the actual site. In the second and third one, we either have  $\hat{b}$  or  $\hat{b}^\dagger$  just to the right. As fourth and last possibility, we can complete the hopping term by  $\hat{b}^\dagger$  or  $\hat{b}$  or can have the interaction term which is purely local. This can be encoded in four possible states so that we end up with the following matrices in the MPO form .

$$W^1 = \begin{pmatrix} U \hat{n}(\hat{n} - 1) & -t \hat{b}^\dagger & -t \hat{b} & \hat{I} \end{pmatrix} \quad W^i = \begin{pmatrix} \hat{I} & 0 & 0 & 0 \\ \hat{b} & 0 & 0 & 0 \\ \hat{b}^\dagger & 0 & 0 & 0 \\ U \hat{n}(\hat{n} - 1) & -t \hat{b}^\dagger & -t \hat{b} & \hat{I} \end{pmatrix}$$

$$W^L = \begin{pmatrix} \hat{I} \\ \hat{b} \\ \hat{b}^\dagger \\ U \hat{n}(\hat{n} - 1) \end{pmatrix} \quad (3.21)$$

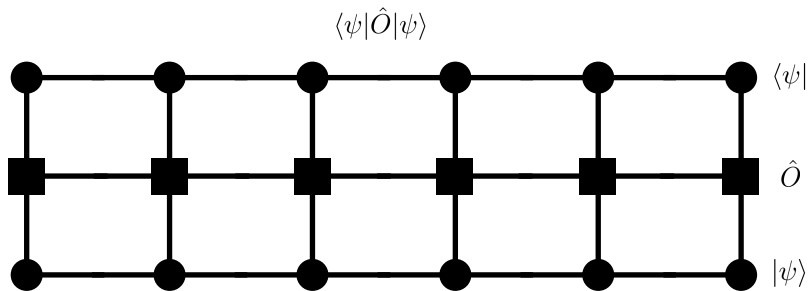


**Figure 3.6.:** Generalization of calculating overlaps with MPO. Operator  $\hat{O}$  is decomposed into local tensors  $W_{b_{i-1}, b_i}^{\sigma_i, \sigma'_i}$ . For a local operator or a product of operators like  $\hat{O} = \hat{O}_i \hat{O}_j$ , we have  $b_i = 1$ .

Due to the non-locality of the Hamiltonian, we had to introduce some kind of bond dimension  $D_W = 4$  just as in the case of MPS above.

The generalization of expectation values to operators that are written in MPO form compared to them discussed in Section 3.2.3 is then straightforward and pictorially given in Fig. 3.6.

## 3.4. Time Evolving Block Decimation

### 3.4.1. Trotter-Suzuki decomposition

Performing time evolution of a system under a given Hamiltonian  $\hat{H}$ , we need the time evolution operator  $\hat{U}(\delta t) = \exp(-i\delta t \hat{H})$ , with  $\delta t$  a small timestep. Very often one is only interested in short-ranged Hamiltonians with only nearest-neighbour interactions

$$\hat{H} = \sum_i \hat{h}_i, \quad (3.22)$$

where  $\hat{h}_1$  acts on sites  $i$  and  $i + 1$ , or put differently, operates only on bond  $i$ . Therefore, we can split the Hamiltonian into two parts, one only operating on even bonds of the chain while the other part acts only on the odd bonds

$$\hat{H} = \sum_{j \text{ even}} \hat{h}_j + \sum_{i \text{ odd}} \hat{h}_i = \hat{H}_{\text{even}} + \hat{H}_{\text{odd}}, \quad (3.23)$$

where  $[\hat{H}_{\text{even}}, \hat{H}_{\text{odd}}] \neq 0$ . Due to the non-commutativity, it is not possible to simply decompose the time evolution operator  $\hat{U}$  in terms of a product of operators acting on even

and odd bonds. However, one can use the first-order Trotter-Suzuki decomposition

$$\exp(-i\delta t \hat{H}) = e^{-i\delta t \hat{h}_1} e^{i\delta t \hat{h}_2} \dots e^{-i\delta t \hat{h}_{L-1}} + \mathcal{O}((\delta t)^2). \quad (3.24)$$

By this decomposition, we introduced the Trotter-error  $\mathcal{O}((\delta t)^2)$ . In order to decrease this error, in the actual implementation we use a second-order Trotter-Suzuki decomposition of the form

$$\exp(-i\delta t \hat{H}) = e^{-i\hat{H}_{\text{odd}}\delta t/2} e^{-i\hat{H}_{\text{even}}\delta t} e^{-i\hat{H}_{\text{odd}}\delta t/2} + \mathcal{O}((\delta t)^3). \quad (3.25)$$

With these ingredients, the basic algorithm for the time evolution takes the following form

- Apply  $e^{-i\hat{h}_j\delta t/2}$  (or  $e^{-\hat{h}_j\delta\tau/2}$  for imaginary time evolution) onto all odd bonds
- Apply  $e^{-i\hat{h}_j\delta t}$  (or  $e^{-\hat{h}_j\delta\tau}$  for imaginary time evolution) onto all even bonds
- Apply  $e^{-i\hat{h}_j\delta t/2}$  (or  $e^{-\hat{h}_j\delta\tau/2}$  for imaginary time evolution) onto all odd bonds

#### 3.4.2. Vidal representation

The TEBD algorithm which was first proposed by Vidal [47, 48] uses the so-called Vidal representation of an MPS

$$|\psi\rangle = \sum_{\sigma_1, \dots, \sigma_L} \Lambda^{[0]} \Gamma^{\sigma_1} \Lambda^{[1]} \Gamma^{\sigma_2} \Lambda^{[2]} \dots \Lambda^{[L-1]} \Gamma^{\sigma_L} \Lambda^{[L]} |\sigma_1, \dots, \sigma_L\rangle. \quad (3.26)$$

In this representation, the  $\Gamma$ -matrices live on the sites of the chain and the  $\Lambda$ -matrices, which are diagonal and contain the singular values, live on the bonds (see Fig. 3.7). We also introduced the scalars  $\Lambda^{[0]} = 1$  and  $\Lambda^{[L]} = 1$  in order to make the following steps more general. The beauty of this representation becomes clear when looking at different groupings of  $\Lambda$  and  $\Gamma$  matrices. Grouping  $A_{a_{i-1}, a_i}^{\sigma_i} = \Lambda_{a_{i-1}, a_i}^{[i-1]} \Gamma_{a_{i-1}, a_i}^{\sigma_i}$  and  $B_{a_{j-1}, a_j}^{\sigma_j} = \Gamma_{a_{j-1}, a_j}^{\sigma_j} \Lambda_{a_j, a_{j+1}}^{[j]}$ , at bond  $l$  we can build a valuable Schmidt decomposition

$$|\psi\rangle = \sum_{a_l} \Lambda_{a_l, a_l}^{[l]} |a_l\rangle_A |a_l\rangle_B \quad (3.27)$$

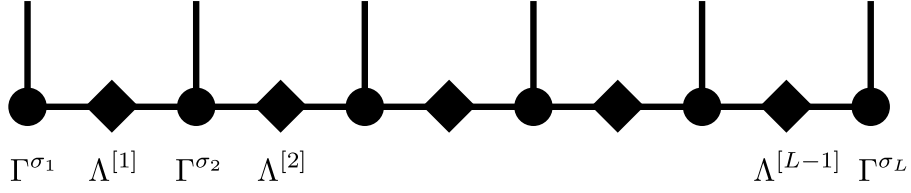


**Figure 3.7.:** Graphical representation of Eq. (3.26).  $\Lambda$  matrices live on the bonds and do not have any physical index  $\sigma_i$ .

where  $\Lambda_{a_l, a_l}^{[l]}$  contains the singular values (or Schmidt values) on the diagonal and

$$|a_l\rangle_A = \sum_{\sigma_1, \dots, \sigma_{l-1}} (A^{\sigma_1} \dots A^{\sigma_{l-1}})_{1, a_l} |\sigma_1, \dots, \sigma_{l-1}\rangle \quad (3.28a)$$

$$|a_l\rangle_B = \sum_{\sigma_l, \dots, \sigma_L} (B^{\sigma_l} \dots B^{\sigma_L})_{a_l, 1} |\sigma_l, \dots, \sigma_L\rangle \quad (3.28b)$$

are basis states of the left (A) and right (B) block respectively. In view of local updates during the TEBD algorithm, we decompose this state further by writing

$$\begin{aligned} |\psi\rangle &= \sum_{a_{l-1}, a_{l+1}, \sigma_l, \sigma_{l+1}} \left( \Lambda^{[l-1]} \Gamma^{\sigma_l} \Lambda^{[l]} \Gamma^{\sigma_{l+1}} \Lambda^{[l+1]} \right)_{a_{l-1}, a_{l+1}} |a_{l-1}\rangle_A |a_{l+1}\rangle_B \\ &= \sum_{a_{l-1}, a_{l+1}, \sigma_l, \sigma_{l+1}} \Psi_{a_{l-1}, a_{l+1}}^{\sigma_l, \sigma_{l+1}} |a_{l-1}\rangle_A |a_{l+1}\rangle_B. \end{aligned} \quad (3.29)$$

where the definition of  $|a_{l-1}\rangle_A$  and  $|a_{l+1}\rangle_B$  should be obvious from Eq. (3.28).

### 3.4.3. TEBD update process

For any kind of time evolution (real or imaginary), we have to apply operators of the form  $e^{-i\delta t \hat{h}_l}$  (cf. Eq. (3.24)) on the MPS. Calculating the matrix elements of such a two-site-operator yields

$$U_{\sigma'_l, \sigma'_{l+1}}^{\sigma_l, \sigma_{l+1}} = \langle \sigma_l \sigma_{l+1} | e^{-i\hat{h}_l \delta t} | \sigma'_l \sigma'_{l+1} \rangle. \quad (3.30)$$

Together with Eq. (3.29) this local update on bond  $l$  reads

$$|\phi\rangle = \sum_{a_{l-1}, a_{l+1}, \sigma_l, \sigma_{l+1}} \Phi_{a_{l-1}, a_{l+1}}^{\sigma_l, \sigma_{l+1}} |a_{l-1}\rangle_A |a_{l+1}\rangle_B, \quad (3.31)$$

where

$$\Phi_{a_{l-1}, a_{l+1}}^{\sigma_l, \sigma_{l+1}} = \sum_{\sigma'_l, \sigma'_{l+1}} U_{\sigma'_l, \sigma'_{l+1}}^{\sigma_l, \sigma_{l+1}} \Psi_{a_{l-1}, a_{l+1}}^{\sigma'_l, \sigma'_{l+1}}. \quad (3.32)$$

### 3. Matrix Product States and Time Evolving Block Decimation

---

Going to the next bond, we have to restore the old  $\Gamma$  -  $\Lambda$ -representation and therefore have to perform an SVD on  $\Phi$  which is reshaped into  $\Phi_{(a_{l-1}\sigma_l),(\sigma_{l+1}a_{l+1})}$  and has dimensions  $dD \times dD$ . Singular value decomposition then leads to

$$\Phi_{(a_{l-1}\sigma_l),(\sigma_{l+1}a_{l+1})} = \sum_{a_l} U_{(a_{l-1}\sigma_l),a_l} \Lambda_{a_l,a_l}^{[l]} (V^\dagger)_{a_l,(\sigma_{l+1}a_{l+1})}. \quad (3.33)$$

After the SVD, the number of singular values has increased to  $dD$  and therefore has to be truncated. Comparing Eq. (3.3), Eq. (3.7) and Eq. (3.27), we immediately see that the truncation error is given by

$$\varepsilon = 1 - \sum_{a_l=1}^D \lambda_{a_l}^2 \quad (3.34)$$

with  $\lambda_{a_l}$  the singular values on bond  $l$ . In practice, we use this equation to define  $D$  implicitly by fixing on the one hand the maximum error we can accept and on the other hand imposing some global maximum value of  $D = D_{\max}$ . In order to keep the state and the singular values properly normalized, we have to renormalise the truncated Schmidt values according to

$$\lambda'_{a_l} = \frac{\lambda_{a_l}}{\sqrt{\sum_{a_l=1}^D \lambda_{a_l}^2}}. \quad (3.35)$$

Further normalization issues due to non-unitarity in the imaginary-time-evolution are discussed in Section 3.4.4.

However, we are not finished yet still having to restore the correct Vidal representation. This can be done by writing

$$\Gamma_{a_{l-1},a_l}^{\sigma_l} = (\Lambda^{[l-1]})_{a_{l-1},a_{l-1}} U_{a_{l-1},a_l}^{\sigma_l} \quad \Gamma_{a_l,a_{l+1}}^{\sigma_{l+1}} = (V^\dagger)_{a_l,a_{l+1}}^{\sigma_{l+1}} (\Lambda^{[l+1]})_{a_{l+1},a_{l+1}} \quad (3.36)$$

Even though this might look innocent, in the case of very small singular values inverting the  $\Lambda$ -matrices can lead to numerical instabilities. Luckily, for infinite system TEBD (see Section 3.6) there has been proposed a workaround [93] that can easily be adapted to our case [89].

The complete time evolution update algorithm for the second-order Trotter decomposition thus reads

- Apply  $e^{-i\hat{h}_i\delta t/2}$  on all odd bonds
  - Build the tensor  $\Phi = U_T\Psi$ , where  $U_T$  is the matrix representation of the time evolution operator.

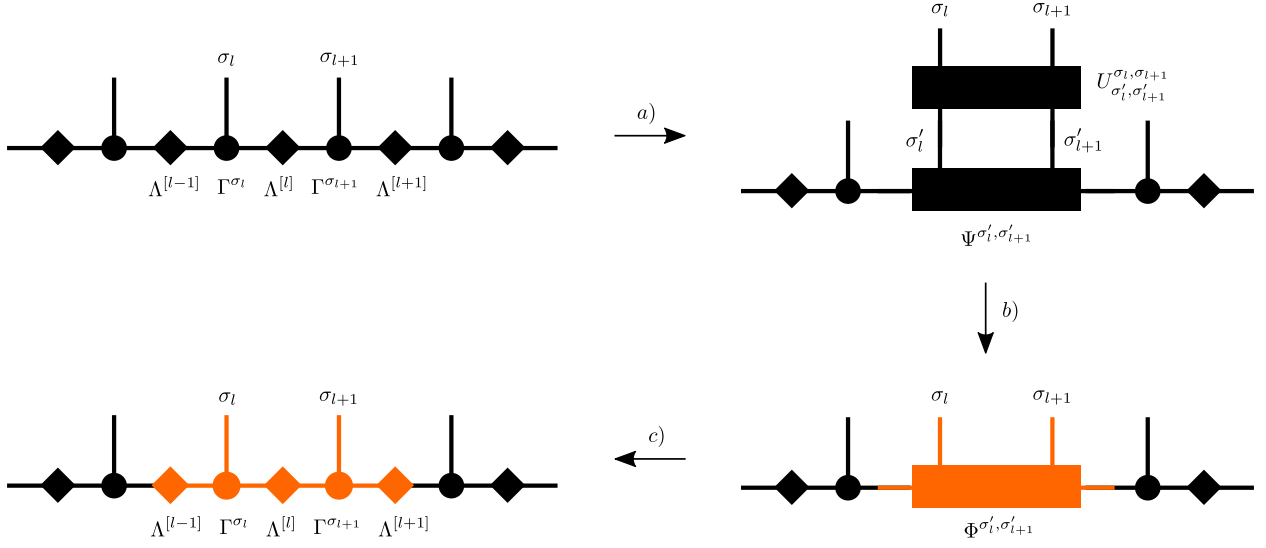


**Figure 3.8.:** Graphical representation of the TEBD update process: a) Build the two site tensor  $\Psi$ . b) Apply the time evolution operator  $U$ . c) Perform SVD on  $\Phi$ , truncate singular values and update tensors  $\Gamma^{\sigma_l}$  and  $\Gamma^{\sigma_{l+1}}$

- Subject  $\Phi$  to an SVD yielding  $\Phi = USV^\dagger$
- Truncate the  $dD$  singular values down to  $D$  and properly normalize the truncated singular values, also properly truncate the columns and rows of  $U$  and  $V^\dagger$  respectively.
- Calculate the updated tensors  $\Gamma^{\sigma_l} = (\Lambda^{[l-1]})^{-1}U$  and  $\Gamma^{\sigma_{l+1}} = V^\dagger(\Lambda^{[l+1]})^{-1}$ .
- Do the same steps when applying  $e^{-i\hat{h}_j\delta t}$  on all even bonds
- Do the same steps when applying  $a^{-i\hat{h}_j\delta t/2}$  on all odd bonds

As the update process in each sweep factorizes on every second bond, this can be parallelized (which, however, has not been done in the actual implementation). Graphically, the update process can be visualized as in Fig. 3.8.

### 3.4.4. Ground state search with TEBD

The TEBD algorithm can not only be used to do real-time evolution of a quantum system but also for calculating the ground state of the system by evolving in imaginary-time. Substituting  $\tau = it$  in the above formulas, we arrive at the so-called imaginary time  $\tau$  which also can be related to a temperature by  $\tau = \beta = 1/k_B T$ , where  $k_B$  is the Boltzmann

constant and  $T$  the temperature. In this sense,  $T \rightarrow 0$  corresponds to  $\tau \rightarrow \infty$ . Then formally, the ground-state of the system can be written as

$$|E_0\rangle = \lim_{\tau \rightarrow \infty} \frac{e^{-\tau \hat{H}} |\phi\rangle}{\|e^{-\tau \hat{H}} |\phi\rangle\|}. \quad (3.37)$$

Where  $|\phi\rangle$  is some (random) initial state. Expanding  $|\phi\rangle$  into the eigenbasis  $\{|E_i\rangle\}$  of  $\hat{H}$ , we get

$$e^{-\tau \hat{H}} |\phi\rangle = \sum_i e^{-\tau E_i} c_i |E_i\rangle = e^{-\tau E_0} c_0 |E_0\rangle + e^{-\tau E_0} \sum_i e^{-\tau(E_i - E_0)} c_i |E_i\rangle. \quad (3.38)$$

Neglecting degeneracies, we have  $E_0 < E_i$  for all  $i \neq 0$  so that  $E_i - E_0 > 0$ . All excited states get damped when increasing  $\tau$  during the imaginary-time evolution. For the ground-state to be resolved, we need  $\tau \gg \frac{1}{E_1 - E_0}$  which can be challenging as for gapless systems, with increasing system size the gap between both states vanishes. This leads to very large values of  $\tau$  or equivalently many iterations during the imaginary-time evolution. However, in contrast to other schemes like DMRG or variational MPS, the only condition for imaginary-time evolution using the TEBD algorithm is a non-vanishing overlap of the initial state  $|\phi\rangle$  with the ground-state

$$\langle E_0 | \phi \rangle \neq 0 \quad (3.39)$$

which can be achieved very easily by using a random state in the beginning. This makes the imaginary-time evolution rather stable whereas the variational MPS scheme is liable to get stuck in local minima, which can be circumvented by different schemes [89].

In order to speed up convergence, for actual implementations it is useful to start with rather large values of  $\delta\tau$  in the beginning to reach large  $\tau$  and then decrease the step size during the imaginary-time evolution in order to reduce the Trotter error  $\mathcal{O}((\delta\tau)^3)$ . The time step is decreased each time the difference between two successive steps is below a certain threshold.

#### Normalization issues in imaginary-time evolution

As the time evolution operator for imaginary time evolution is not unitary, neither the norm of the state nor the orthonormality of the bases of left and right blocks is preserved [94].

The first problem can be easily circumvented by explicitly normalizing the  $\Phi$ -matrix

$$\tilde{\Phi}_{(a_{l-1}\sigma_l),(\sigma_{l+1}a_{l+1})} = \frac{\Phi_{(a_{l-1}\sigma_l),(\sigma_{l+1}a_{l+1})}}{\sqrt{\sum_{\sigma_l, \sigma_{l+1}, a_{l-1}, a_{l+1}} |\Phi_{a_{l-1}, a_{l+1}}^{\sigma_l, \sigma_{l+1}}|}}. \quad (3.40)$$

The second issue can be solved by applying a slight modification of the TEBD algorithm which then explicitly restores orthonormality. In order to understand the problem, let us take a closer look at the update process. During the TEBD-step, the basis states  $|a_l\rangle_A$  and  $|a_l\rangle_B$  are explicitly orthonormalized. However, basis states of blocks that contain site  $l$  or site  $l + 1$  (e.g.  $|a_{l+1}\rangle_A$ ) lose their orthogonality. In the second order Trotter decomposition, we proceed with sites  $l + 2$  and  $l + 3$  so that  $\{|a_{l+1}\rangle_A\}$  is not an orthonormal set of states. In order to sidestep this problem, we do not skip the bond  $l + 1$  but apply an identity operation onto sites  $l + 1$  and  $l + 2$ . As the identity is a unitary operator we do not have any normalization issues and can proceed to sites  $l + 2$  and  $l + 3$  having properly normalised states.

The new scheme then goes as follows: First we apply the odd site operator on sites 1 and 2 followed by application of the identity operation on sites 2 and 3, then we again apply the odd site operator on sites 3 and 4 and so on. For the backward sweep, we apply the even site operator on even sites and identity operations on the odd sites. The third sweep is then equal to the first one. At the end, one single sweep with only the identity operator on all sites is done. Of course, the matrix  $\Phi$  has still to be normalized at each step.

For the ground state search, the time step decreases towards the end so that the time evolution operator becomes close to being unitary and the issues due to non-unitarity play a minor role.

### 3.4.5. Error sources

During the time evolution two major error sources arise. The first one is the error due to the Trotter step which can be decreased by higher-order Trotter decompositions. For example, the error for a second-order Trotter decomposition scales with  $\mathcal{O}((\delta t)^3)$ . The number of steps for simulating up to some time  $t$  is  $t/\delta t$  so that the accumulated error is  $\mathcal{O}((\delta t)^2 t)$ , scaling linearly in time and being independent of the system size  $L$ . However, by choosing the time step small enough, this should not be a problem in practice.

The more severe error comes from the truncation of singular values during one TEBD step. In Section 3.1, we discussed that the entanglement in the system during time evolution

grows linearly in time,  $S(t) = S(0) + vt$  leading to an exponential increase of the bond dimension,  $D \sim 2^t$ . For a simulation time  $t$ , one needs  $\mathcal{O}(Lt/\delta t)$  local applications of the two-site time evolution operator  $U$ . The total accumulated error due to truncation after some time  $t$  is  $\mathcal{O}((1 - \varepsilon)^{Lt/\delta t})$  where  $\varepsilon$  is the maximum error during one TEBD step (see Eq. (3.7)). We see immediately that the error due to the truncation scales exponentially in time as well as in the system size. The only possibility to reduce this error is to increase the maximum bond dimension  $D$  reducing  $\varepsilon$ . The standard procedure in all calculations is therefore to run simulations with different  $D$  and consider the results more and more exact in the limit  $D \rightarrow \infty$  (see [95]).

### 3.5. MPS with conserved quantum numbers

The bottleneck in the TEBD update process obviously is the SVD performed on the  $dD \times dD$  matrix  $\Phi$  with complexity  $\mathcal{O}(d^3 D^3)$ . For large local Hilbert spaces or large bond dimensions this gets inefficient and slow very soon. Many models, however, respect symmetries that can be used to speed up calculations very drastically. In this thesis, we consider  $U(1)$ -symmetries like particle number or  $S_z$  conservation.

Assume that the Hamiltonian we are considering conserves the total particle number  $N$  of the system. For any decomposition of our system into two subblocks  $A$  and  $B$  (cf. Fig. 3.1) we have the constraint

$$N(A) + N(B) = N \tag{3.41}$$

where  $N(A)$  and  $N(B)$  are the particle numbers in block  $A$  and  $B$ , respectively. Put differently, each basis state of block  $A$  and  $B$  has some definite particle number and we can group the states into blocks corresponding to the same particle number. Choosing local basis states  $|\sigma_l\rangle$  that are eigenstates of the operator corresponding to the symmetry (e.g.  $|n_l\rangle$  for particle number conservation), the elements  $M_{a_{l-1}, a_l}^{\sigma_l}$  of a tensor  $M^{\sigma_l}$  are only non-zero for

$$N(a_{l-1}) + N(\sigma_l) = N(a_l). \tag{3.42}$$

Here we assume block growth from the left, so that  $|a_l\rangle_A = |a_{l-1}\rangle_A \otimes |\sigma_l\rangle$ . For the boundary terms, we have  $N(a_0) = 0$  and  $N(a_L) = N$ . These constraints can also be encoded in the graphical representation introduced above by assigning arrows corresponding to the 'flux of quantum numbers' in the system (see Fig. 3.9).

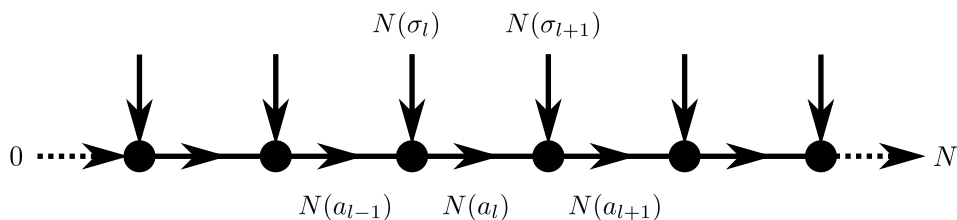


**Figure 3.9.:** Graphical representation of an MPS with quantum number conservation. On each site, we assign arrows to the legs of the tensors that correspond to the flux of the quantum numbers. At the first site, we introduce an initial quantum number 0 and at the end we have the target quantum number  $N$

### 3.5.1. TEBD update process

From these observations, it follows immediately that the elements  $\Phi_{a_{l-1}, a_{l+1}}^{\sigma_l, \sigma_{l+1}}$  of  $\Phi$  are only non-zero if

$$N(a_{l-1}) + N(\sigma_l) + N(\sigma_{l+1}) = N(a_{l+1}). \quad (3.43)$$

Looking at Eq. (3.42) and noting that  $N(a_{l-1}) - N(\sigma_{l+1}) = N(a_l) \equiv N_l$  we can group the elements of  $\Phi$  into blocks  $\Phi^{N_l}$  that are labeled by the number of particles in the left block when splitting the system at bond  $l$ . Each block contains only elements fulfilling Eq. (3.42) and Eq. (3.43). In addition, the reduced density matrix  $\rho_A$  which can be calculated from  $\rho_A = \Phi\Phi^\dagger$  (or equivalently  $\rho_B = \Phi^\dagger\Phi$ ) takes a block diagonal form. As subjecting  $\Phi$  to an SVD is equivalent to diagonalizing  $\rho_A$  (or  $\rho_B$ ), we can simply perform the SVD on each block  $\Phi^{N_l}$  individually. Even though the scaling of the SVD does not change, the blocks  $\Phi^{N_l}$  are usually much smaller than  $dD \times dD$  leading to a decrease of computational effort.

The complete update process is summarized in the following steps:

- (1) Calculate all possible values of  $N_l$  at bond  $l$ . This can also be done at the beginning of the sweeping process as these values are fixed.
- (2) Build the two-site tensor  $\Phi_{a_{l-1}, a_{l+1}}^{\sigma_l, \sigma_{l+1}}$  calculating only the non-zero elements according to Eq. (3.43).
- (3) Reshape  $\Phi$  as in the ordinary update process and group elements into blocks  $\Phi^{N_l}$  for all previously calculated values of  $N_l$ .
- (4) Perform SVD on each block individually. In the worst case this still scales with  $\mathcal{O}(d^3 D^3)$  but usually is much faster as the block dimensions are much smaller than the dimensions of the whole  $\Phi$ .

- (5) Keep the  $D$  largest singular values of **all** blocks and truncate.
- (6) Update the tensors  $\Gamma^{\sigma_l}$  and  $\Gamma^{\sigma_{l+1}}$  as in Eq. (3.36).

For models with more conserved quantum numbers (e.g. Bose-Fermi-Resonance model with  $N$  and  $S_z$  conserved) the discussion from above can be generalized by using vectors  $\vec{N}_l = (N_l, S_{z,l})$ . The constraints Eq. (3.42) and Eq. (3.43) then simply have to be fulfilled component by component.

### 3.5.2. Examples

In order to see how the procedure discussed above translates into practice, we want to give some examples. First, we discuss how to set up the list of possible particle numbers at all bonds. To this end, consider for example a system, where we locally have the basis states  $|0\rangle$  and  $|1\rangle$  so that on one site we have  $N(\sigma_l) = 0, 1$ . Further, assume we have a system of length  $L = 4$  and total particle number  $N = 2$ . Then we have  $N_0 = 0$  and  $N_4 = 2$ . On the sites in between, we can have

$$N_1 = 0, 1 \quad N_2 = 0, 1, 2 \quad N_3 = 1, 2. \quad (3.44)$$

We also know that all non-zero elements of a tensor  $M^{\sigma_l}$  have to fulfill Eq. (3.42). This means that this tensor has some kind of block structure, whose blocks are labelled by  $(N(\sigma_l), N(a_{l-1}), N(a_l))$ .

site 1	site 2	site 3	site 4
(0,0,0)	(0,0,0)	(0,1,1)	(0,2,2)
(1,0,1)	(0,1,1)	(0,2,2)	(1,1,2)
	(1,0,1)	(1,0,1)	
	(1,1,2)	(1,1,2)	

**Table 3.5.1.:** Possible blocks for  $L = 4$  and  $N = 2$  for  $N(\sigma) = 0, 1$

The simplest way to implement this kind of block-structured MPS is to build lists of valid blocks on each site, where each element of the list maps to some tensor

$$(N(\sigma_l), N(a_{l-1}), N(a_l)) \rightarrow M_{\alpha_{l-1}, \alpha_l}^{x_l}. \quad (3.45)$$

In this notation,  $x_l$  is kind of a dummy index, usually being 1. However, there are cases where two or more states of the local Hilbert space have the same quantum number  $N(\sigma)$ .

As a very simple example, we take the Néel state  $|\psi\rangle = |1010\rangle$ . From Table 3.5.1 we immediately see the blocks that contain non-zero elements

$$M_{(1,0,1)}^1 = 1, \quad M_{(0,1,1)}^2 = 1, \quad M_{(1,1,2)}^3 = 1, \quad M_{(0,2,2)}^4 = 1. \quad (3.46)$$

## 3.6. iTEBD

Approaching the thermodynamic limit by increasing  $L$  numerically is very costly, as the computational effort scales linearly in system size. Vidal [90] proposed an algorithm that generalizes the ordinary time evolving block decimation to infinite systems (iTEBD). The basic assumption is that we are dealing with a translationally invariant system and are only looking at one unit cell of the system. For Hamiltonians with only nearest-neighbour interaction, the unit cell only contains two sites. The Vidal representation of this state then reads

$$|\psi\rangle = \sum_{a_{l-1}, a_{l+1}, \sigma_l, \sigma_{l+1}} \left( \Lambda^{[l-1]} \Gamma^{\sigma_l} \Lambda^{[l]} \Gamma^{\sigma_{l+1}} \Lambda^{[l+1]} \right)_{a_{l-1}, a_{l+1}} |a_{l-1}\rangle_A^\infty |a_{l+1}\rangle_B^\infty, \quad (3.47)$$

where  $|a_{l-1}\rangle_A^\infty$  and  $|a_{l+1}\rangle_B^\infty$  are now basis states of semi-infinite subsystems with sites  $\{-\infty, \dots, l-1\}$  and  $\{l+1, \dots, \infty\}$ . As the state is invariant under shifts of two lattice sites, the  $\Gamma$  and  $\Lambda$  matrices are basically independent of  $l$  and we can choose

$$\Gamma^{\sigma_{2l}} = \Gamma^{\sigma_A}, \quad \Lambda^{[2l]} = \Lambda^A, \quad \Gamma^{\sigma_{2l+1}} = \Gamma^{\sigma_B}, \quad \Lambda^{[2l+1]} = \Lambda^B. \quad (3.48)$$

The iTEBD update process is then equal to the TEBD update with the only change that when applying even-site operations we simply interchange the roles of  $A$  and  $B$  in the labelling of the  $\Gamma$  and  $\Lambda$  matrices.

### 3.6.1. Comparison between TEBD and iTEBD

One of the main differences between conventional TEBD and iTEBD is the computational cost for simulating time-dependent quantum systems. For finite systems, the computational cost for one time step is  $\mathcal{O}(Ld^3D^3)$  due to the SVD performed on each bond, whereas in the infinite system case we have  $\mathcal{O}(d^3D^3)$  since we are only concerned with two sites. Also the storage for the MPS decreases by some factor proportional to the system size.

One possible problem comes up when working, for example, with constant particle number

(density) or magnetization. For an implementation of TEBD with conservation of quantum numbers, this can be done by simply setting the total particle number or magnetization. In iTEBD, with a unit cell consisting of two sites, it is only possible to vary, for example, the density in steps of one half. In order to set the density to other values, one has to increase the unit cell, leading to more computational effort.

However, this problem only arises for the ground state search with imaginary-time evolution. Theoretically, as the Hamiltonian conserves total particle number, by setting up an initial state with definite particle number, the particle number should stay constant during the time evolution. Practically, the time evolution operator  $e^{-\tau\hat{H}}$  is not unitary, leading to numerical errors that can drive the state out of the symmetry sector thus mixing states with different particle numbers. To this end, one has to add a term  $-\mu\hat{N}$  with chemical potential  $\mu$  coupling to the total particle number. This leads to a grand-canonical system, where the particle number is fixed only on average. In the actual implementation, this led to non-conservation of particle number in the real-time evolution in the BFRM model due to contributions of different symmetry sectors.

## 3.7. Implementation and test results

The code was written using Python 2.7.6 and Numpy 1.8.2. We implemented both an iTEBD code as well as an TEBD code, which was further optimized by making use of conserved quantum numbers ( $N$  and  $S_z$ ). For the conserved quantum numbers, we wrote an own tensor module that deals with the contraction of tensors in block structure labeled by quantum numbers.<sup>1</sup> All other tensor operations as well as SVD are done using the `numpy` module.

The code provides the calculation of ground states with imaginary time evolution, real time evolution as well as local expectation values, correlations and expectation values for operators in MPO form.

While doing calculations for the BFRM, we became aware of some bugs in the Numpy SVD function which caused an error in some cases due to possibly ill-conditioned matrices. As a workaround, we used a wrapper for the LAPACK function DGESVD for real matrices and ZGESVD for complex ones.

---

<sup>1</sup>However, this turned out to be very inefficient in Python due to for-loops.

### 3.7.1. Testing the code

For testing the code, we use the so-called XXZ model which is a spin-1/2-chain with non-isotropic coupling of the  $z$ -components of neighbouring spins

$$\hat{H}_{\text{XXZ}} = J \sum_i \left\{ \hat{S}_i^x \hat{S}_{i+1}^x + \hat{S}_i^y \hat{S}_{i+1}^y + \Delta \hat{S}_i^z \hat{S}_{i+1}^z \right\} = J \sum_i \left\{ \frac{1}{2} \left( \hat{S}_i^+ \hat{S}_{i+1}^- + \hat{S}_i^- \hat{S}_{i+1}^+ \right) + \Delta \hat{S}_i^z \hat{S}_{i+1}^z \right\}. \quad (3.49)$$

Here,  $\hat{S}_i^x$ ,  $\hat{S}_i^y$  and  $\hat{S}_i^z$  are spin-1/2 operators on site  $i$  and  $\hat{S}_i^+ = \hat{S}_i^x + i\hat{S}_i^y$  and  $\hat{S}_i^- = \hat{S}_i^x - i\hat{S}_i^y$  are spin-flip operators.

With the help of the Jordan-Wigner transformation [96] we can map this model onto spinless fermions with nearest neighbour interaction

$$\hat{H} = -J \sum_i \frac{1}{2} \left( \hat{c}_i^\dagger c_{i+1} + \text{h.c.} \right) + \Delta \left( \hat{n}_i - \frac{1}{2} \right) \left( \hat{n}_{i+1} - \frac{1}{2} \right) \quad (3.50)$$

with fermionic annihilation and creation operators  $\hat{c}_i$  and  $\hat{c}_i^\dagger$ .

This Hamiltonian conserves the total magnetization (XXZ) or the total particle number (spinless fermions) so that we can use the optimized TEBD code with particle number conservation for our simulations.

In the following, we will simulate the relaxation of local magnetization after a quantum quench from a Néel state to the isotropic case ( $\Delta = 0$ ). Further, we calculate the ground state energy with imaginary-time evolution for selected values of  $\Delta$ . All results are compared with analytical expressions.

#### Quench in the XXZ model

First, we want to do a quantum quench starting with a Néel state  $|101010101\dots\rangle$  at  $t = 0$  which is an eigenstate of Eq. (3.50) in the case of  $\Delta = \infty$ . However, for  $t > 0$  we chose  $\Delta = 0$  so that the state will evolve in time. The analytical expression for the local magnetization after the quench is given by [97]

$$m(t) = \frac{1}{2} J_0(2t) \quad (3.51)$$

where  $J_0$  is the zeroth-order Bessel function of the first kind.

In Fig. 3.10, we compare the time evolution using the iTEBD and the TEBD algorithm with the analytical result. For the TEBD simulation we use  $L = 100$  in order to reduce the

finite size effects, we also use conservation of particle number (magnetization) in order to speed up the calculations. As a result, we see that both simulations fit very well to the analytical expression. However, at large times, the entanglement in the system is too large for the state to be accurately approximated (see Section 3.4.5). In Fig. 3.11, we see that the simulation time can be pushed to higher values by increasing the bond dimension  $D$  with  $D \rightarrow \infty$  giving exact results for all times.

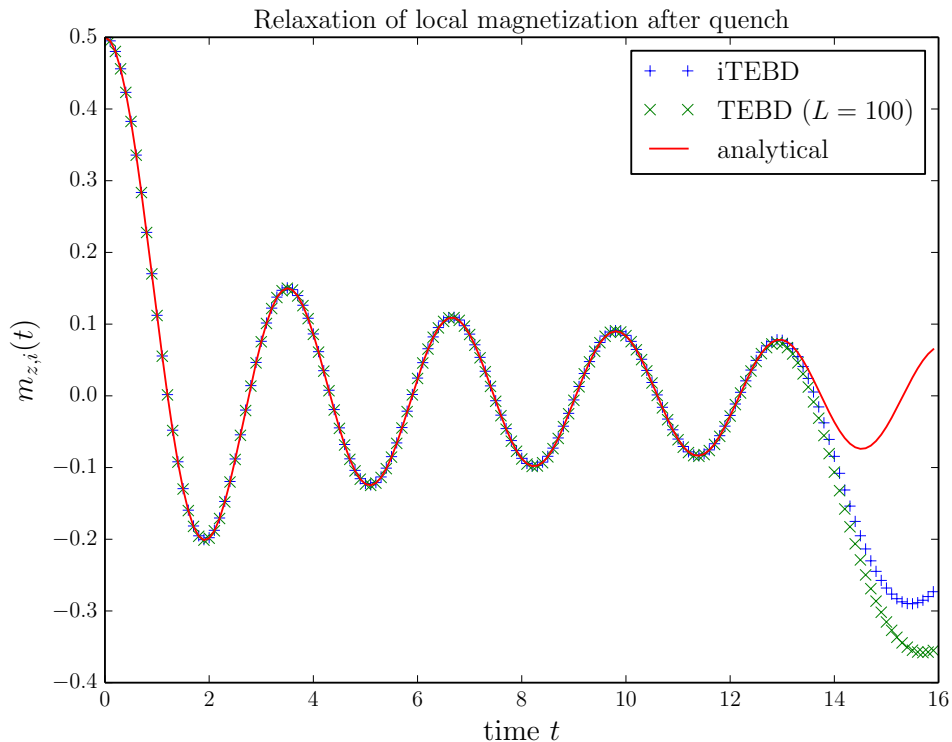


**Figure 3.10.:** Relaxation of the local magnetization after a quantum quench from the Néel state to  $\Delta = 0$ . Comparison between iTEBD and TEBD and analytical results ( $D = 512$ ,  $\delta t = 0.1$ )

### Groundstate search

For the ground state search with imaginary time evolution we used some optimized scheme which goes as follows. We first chose a rather large time step  $\delta\tau$  in order to get close to the ground state. As soon as the difference in energy between two subsequent Trotter steps is smaller than some predefined value  $\delta E$  we decrease the time step. This procedure is done until some lower bound for  $\delta\tau$  is reached.

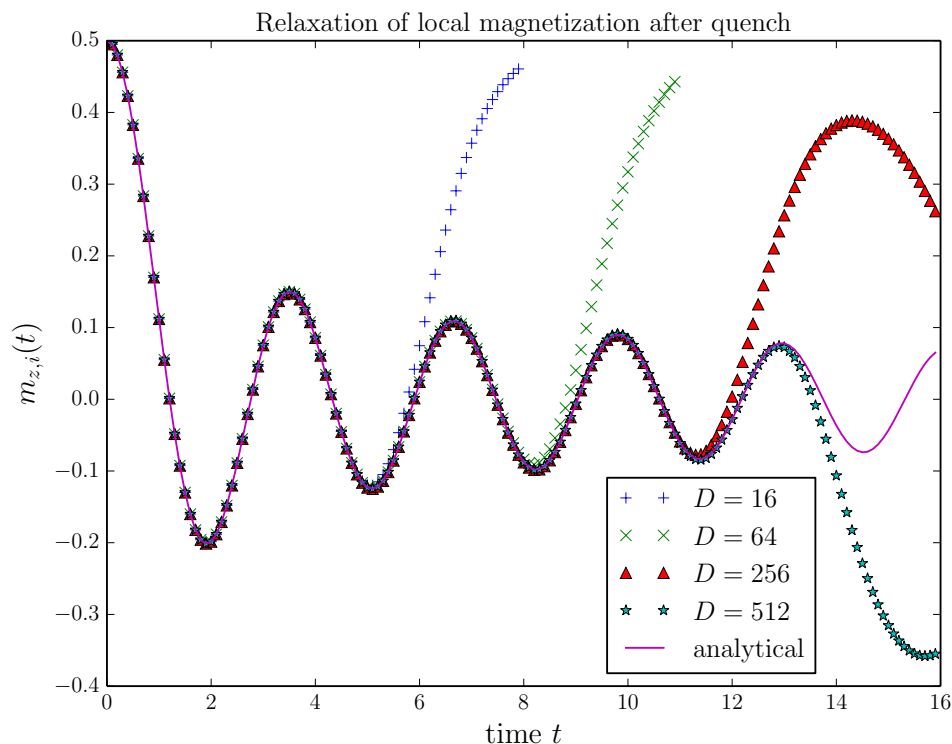


**Figure 3.11.:** Relaxation of the local magnetization after a quantum quench from the Néel state to  $\Delta = 0$  for different values of  $D$  with TEBD ( $\delta t = 0.1$ )

**iTEBD** In Fig. 3.12, one can see how the energy converges towards the ground state energy of the system. The jumps indicate the points, at which the time step  $\delta\tau$  is changed. The number of iterations needed for convergence does not only depend on the value of  $\Delta$  but it also depends strongly on the maximum bond dimension one allows.

In the case of no anisotropy or, equivalently, no interactions in the fermionic case, we immediately can write down the groundstate energy of the system

$$E_0 = -J \sum_{k \leq k_F} \cos(k). \quad (3.52)$$

For a half-filled system in the thermodynamic limit, this becomes

$$\frac{E_0}{L} = -\frac{1}{\pi} \approx -0.31831 J. \quad (3.53)$$

For  $\Delta \leq -1$ , the groundstate energies can be calculated with Bethe-ansatz [98]. In

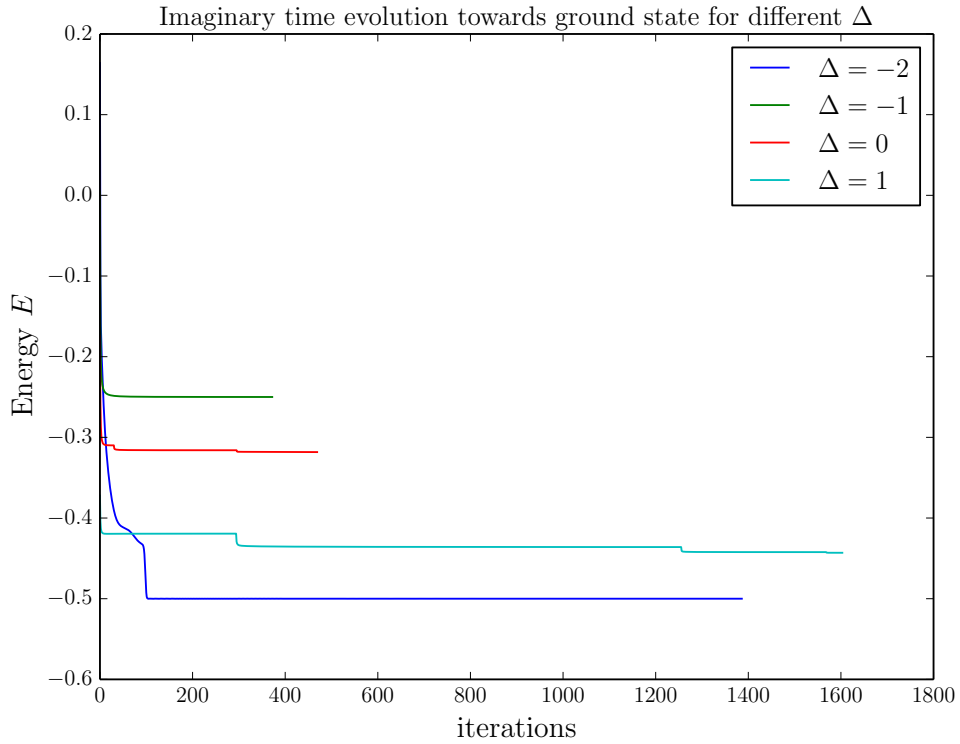


**Figure 3.12.:** Ground state search with imaginary-time evolution for different values of anisotropy with iTEBD. Jumps denote changes in the size of the timestep  $\delta\tau$ . All calculations are done with  $D = 512$  and the Néel state as initial state. The time step was changed when the difference in energy of two subsequent steps was below  $10^{-7}$  from  $\tau_0 = 0.4$  to  $\tau_{\text{final}} = 10^{-4}$ .

Table 3.7.1, we show the computed and analytical values of the groundstate energy. The results match quite well while the precision can be tuned by adjusting the parameters (making  $D$  larger, setting a lower threshold  $\delta E$ , ...).

$\Delta$	$E_{0,\text{exact}}[J]$	$E_{0,\text{numerical}}[J]$	$(E_{0,\text{exact}} - E_{0,\text{numerical}})/E_{0,\text{exact}}$
0	-0.31831	-0.31826	0.00016
1	-0.44315	-0.44307	0.00018
-1	-0.2500	-0.24996	0.00016
-2	0.5000	-0.5000	0.0000

**Table 3.7.1.:** Comparison between analytical values of the groundstate energy and values computed with iTEBD and imaginary-time evolution.  $\tau_0 = 0.4/J$ ,  $\tau_{\text{final}} = 10^{-4}/J$ ,  $\delta E = 10^{-7} J$  and  $D = 512$

**TEBD** In order to compare the calculations done in TEBD with the values obtained for a system in the thermodynamic limit, we perform extrapolation to  $L \rightarrow \infty$ . In Fig. 3.13, we show the computed groundstate energies and the corresponding fit with a function

$$E\left(\frac{1}{L}\right) = \frac{a}{L} + \tilde{E}_0. \quad (3.54)$$

In the thermodynamic limit ( $L \rightarrow \infty$ ),  $\tilde{E}_0$  is the groundstate energy of the infinite system. From the fit, we get

$$\tilde{E}_0/J = -0.31827833 \quad (3.55)$$

with a variance on the order of  $10^{-6}$ . This is in good agreement with the values obtained from the analytical calculation as well as from the iTEBD simulation.

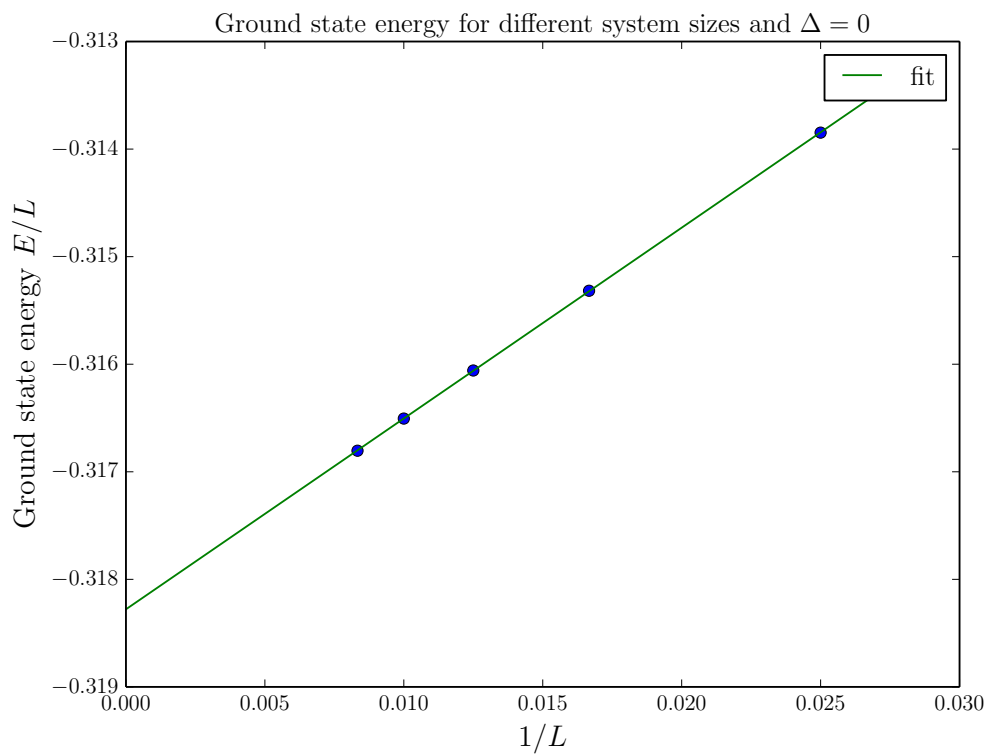


**Figure 3.13.:** Groundstate energies for different system sizes with TEBD and imaginary-time evolution. Extrapolation for  $L \rightarrow \infty$  was performed.  $\tau_0 = 0.4/J$ ,  $\tau_{\text{final}} = 10^{-4}/J$ ,  $\delta E = 10^{-7} J$  and  $D = 512$

## 4. Numerical Results

In this part, we want to study the dynamics when we ramp from the BCS side to the BEC side of the resonance, where we especially focus on the survival of FFLO correlations in the molecule momentum distribution function. To this end, we first locate the resonance region, reproducing the results from [44]. We then study the number of created molecules during the ramp for different ramp times and polarizations. Further, we extend the results obtained in [45] to the case of a larger system and compare them to the results obtained in [45, 46]. In order to understand the dynamics during the ramp better, we discuss the emergence of adiabaticity and the connection to the Kibble-Zurek theory as discussed in Section 2.2.

### 4.1. Ramps across the resonance

First, we want to locate the resonance region by studying the number of molecules present in the ground state (Fig. 4.1), where we reproduce the results obtained in [44] with the parameters chosen in [45] in order to be able to compare our results to previous work.

Clearly, the number of molecules saturates for large detuning in the BEC limit but decreases with the given polarization of the system. This is obvious as the number of down-fermions decreases. Interestingly, for large polarizations, the number of molecules saturates already on the BCS side ( $\nu < 0$ ). These results were also obtained in [44]. In the following, we take the region from  $\nu_0 = -3t$  to  $\nu_1 = t$  as our ramp region as the number of molecules is almost zero in the beginning and reaches its maximum value at the final detuning. This is in accordance to the phase boundaries calculated in [44], where, for  $g = t/2$ , the phase boundary between the FFLO phase and the BEC+PP LL phase extends from  $\nu \approx -1.5t$  for small polarizations down to  $\nu \approx -2.5t$  for an almost fully polarized system<sup>1</sup>. The second boundary between the BEC+PP LL phase and the BEC+FP FG

---

<sup>1</sup>The binding energy on resonance is  $\varepsilon^* \approx 0.197t$  for  $g = t/2$  and has been calculated from Eq. (1.23).

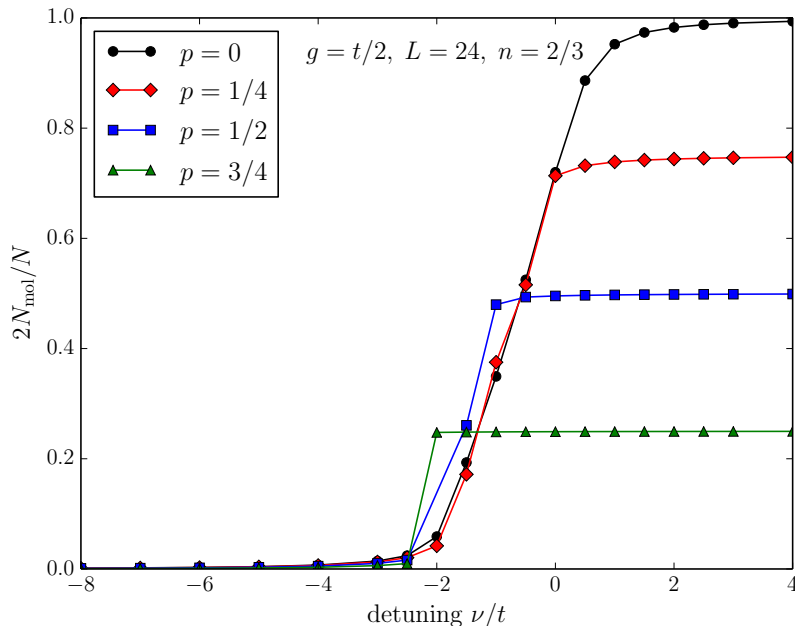


**Figure 4.1.:** Number of molecules in the ground state vs. detuning  $\nu$  for different polarizations (TEBD:  $D = 256$ ,  $\varepsilon = 10^{-8}$ ,  $\delta E = 10^{-8} t$ ,  $\tau_0 = 0.4/t$ ,  $\tau_f = 10^{-4}/t$ )

phase varies from  $\nu \approx 0.5 t$  for small  $p$  to  $\nu \approx -2.5 t$  for an almost fully polarized system. Thus, our choice for the initial and final value of the detuning for the ramp should be able to capture the whole resonance region, including the intermediate BEC+PP LL phase. Further, we want to stay close enough to resonance in order to still have strong interactions. This is motivated by the observation in [46] that FFLO correlations are most pronounced for initially strong interactions.

Recalling the discussion from Section 1.2, we comment on the type of the resonance, where the limit of a broad Feshbach resonance is characterized by the condition  $nr^* \ll 1$ , where  $r^*$  is essentially the size of the bound state at resonance (in units of the lattice spacing) and can be calculated from  $\varepsilon^*/(2t) = 1/(r^*)^2$ . The limit of a broad Feshbach resonance also corresponds to the strong-coupling limit. The opposite case of a narrow Feshbach resonance is characterized by  $nr^* \gg 1$ . For the parameters we are using,  $g = t/2$  and  $n = 2/3$ , we get  $nr^* \approx 2$  such that we are clearly not in the limit of a broad resonance. To reach this limit, we would have to either decrease the density or increase the Feshbach coupling  $g$ , leading to a higher binding energy at resonance (cf. also [44]). Going to smaller densities, however, would lead to a smaller total number of molecules being created during the ramp. As we already discuss rather small system sizes (up to  $L = 24$ ), we do not

decrease the density. The choice of  $g$  is motivated by previous work as discussed above.

The ramp across the resonance is performed linearly in time according to

$$\nu(t) = \nu_0 + \frac{\nu_1 - \nu_0}{\tau_r} t, \quad (4.1)$$

where  $\tau_r$  is the ramp time and  $\frac{\nu_1 - \nu_0}{\tau_r}$  can be seen as the ramp velocity. As we fix  $\nu_0$  and  $\nu_1$  for all ramp times, large ramp times  $\tau_r$  correspond to slow ramps and vice versa.

In the following, we will have a look at different observables in order to understand the dynamics during the ramp and to figure out how to optimally perform the ramp in order to detect the FFLO correlations in the momentum distribution function of the molecules after the ramp.

#### 4.1.1. Number of molecules

We first turn to the number of molecules during the ramp as experimentally, it is desirable to transform all paired fermions into molecules in order to enhance the signal in the momentum distribution function. The number of molecules for  $p = 1/4$  and  $p = 3/4$  for different ramp times is plotted in Fig. 4.2.

For both polarizations, the number of molecules reaches its maximum value  $N_{\min} = N_{\downarrow}$  for long ramp times, where  $N_{\downarrow}$  is the number of minority fermions in the BCS limit,  $\nu \rightarrow \infty$ . For large polarization ( $p = 3/4$ ), we observe small oscillations for a ramp time  $\tau_r = 512/t$ , which appear independent of the number of states we keep (verified also for  $D = 1024$ ).

Interestingly, the number of molecules seems to saturate even for intermediate ramp times,  $\tau_r \sim 64/t$ , which indicates some 'adiabatic' behaviour in the molecule number. In order to quantify the degree of adiabaticity in the number of molecules we introduce the rescaled number of molecules

$$N_{\text{mol}}^{\text{res}} = \frac{N_{\text{mol}}(\nu = t) - N_{\text{mol}}^0(\nu = -3t)}{N_{\text{mol}}^0(\nu = t) - N_{\text{mol}}^0(\nu = -3t)}, \quad (4.2)$$

where we look at the difference between the number of molecules after the ramp (at  $\nu = t$ ) and the number of molecules in the ground state,  $N_{\text{mol}}^0$ , at  $\nu = -3t$ , normalized by both ground state values. With this definition,  $N_{\text{mol}}^{\text{res}} \rightarrow 1$  indicates adiabatic behaviour whereas  $N_{\text{mol}}^{\text{res}} = 0$  in the case of completely diabatic (impulse like) behaviour. As can be seen from Fig. 4.3, the rescaled molecule number saturates at unity for large ramp times and even for intermediate ramp times in the case of large polarizations. The observation that  $N_{\text{mol}}^{\text{res}}$

## 4. Numerical Results

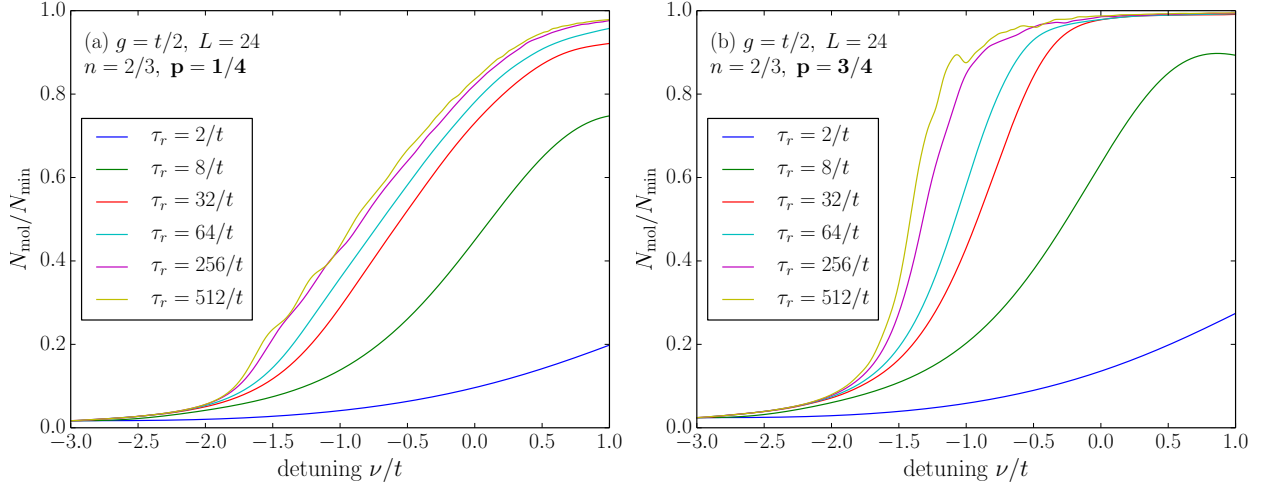


**Figure 4.2.:** Number of molecules during the ramp normalized by  $N_{\downarrow}$  in the BCS limit for various ramp times and polarizations (a)  $p = 1/4$  and (b)  $p = 3/4$ . (TEBD:  $D = 512$ ,  $\varepsilon = 10^{-8}$ ,  $n_{\text{steps}} = 2560$  ( $\tau_r \leq 256/t$ ) and  $n_{\text{steps}} = 5120$  ( $\tau_r = 512/t$ ))

does not saturate for smaller polarizations may be related to the fact that the number of molecules in the ground state has not completely saturated at  $\nu = t$  for smaller polarizations (cf. Fig. 4.1).

If we include  $N_{\text{mol}}^0(\nu)$  (Fig. 4.4), we can compare the time evolution of the number of molecules to the ground state values.  $N_{\text{mol}}^0$  features two kinks at  $\nu \approx -2.4t$  and  $\nu \approx -2.1t$  for  $p = 3/4$ . At the first kink, a few of the composite fermions form molecules and the system should be in the intermediate BEC+PP LL phase, the second kink indicates the transition to the BEC+FP FG phase. Compared to the phase diagram in [44], we get transition points that are smaller which may be due to finite size effects. The location of the kinks can also be determined by the breakdown of the FFLO correlations in the momentum distribution function in the ground state (see next section).

Following the evolution of  $N_{\text{mol}}$ , at the beginning of the ramp, the number of molecules follows the ground state value up to the first kink. However, for very short ramp times, it seems as if the system cannot follow adiabatically even before the first transition. From this point on to the second kink, the system cannot follow the ground state due to the transition point. At the second kink, it can be seen that for large ramp times, the system tries to reach the ground state value of the molecule number, whereas for intermediate ramp times it still overshoots.

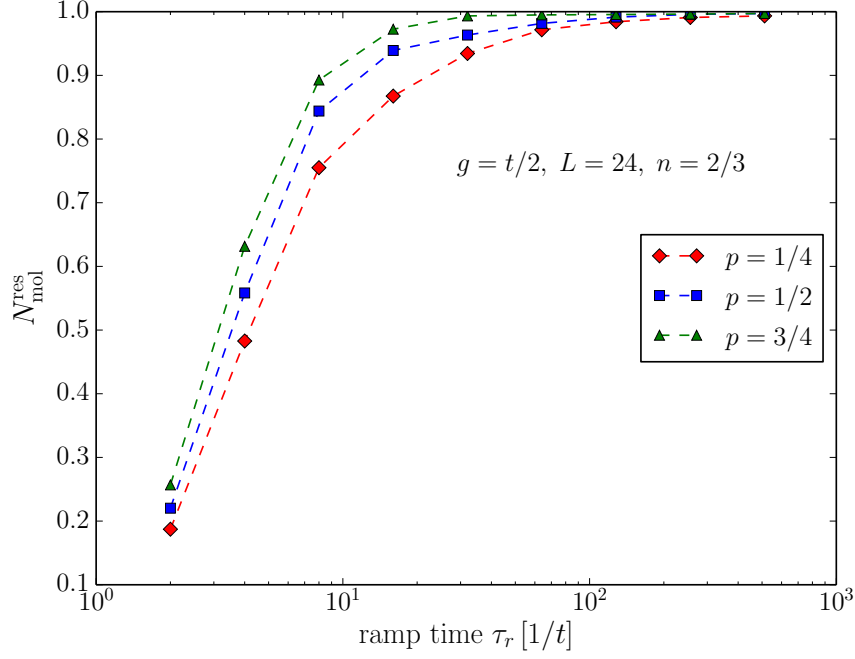


**Figure 4.3.:**  $N_{\text{mol}}^{\text{res}}$  vs ramp time for different polarizations. (TEBD:  $D = 512$ ,  $\varepsilon = 10^{-8}$ ,  $n_{\text{steps}} = 2560$  ( $\tau_r \leq 256/t$ ) and  $n_{\text{steps}} = 5120$  ( $\tau_r = 512/t$ ))

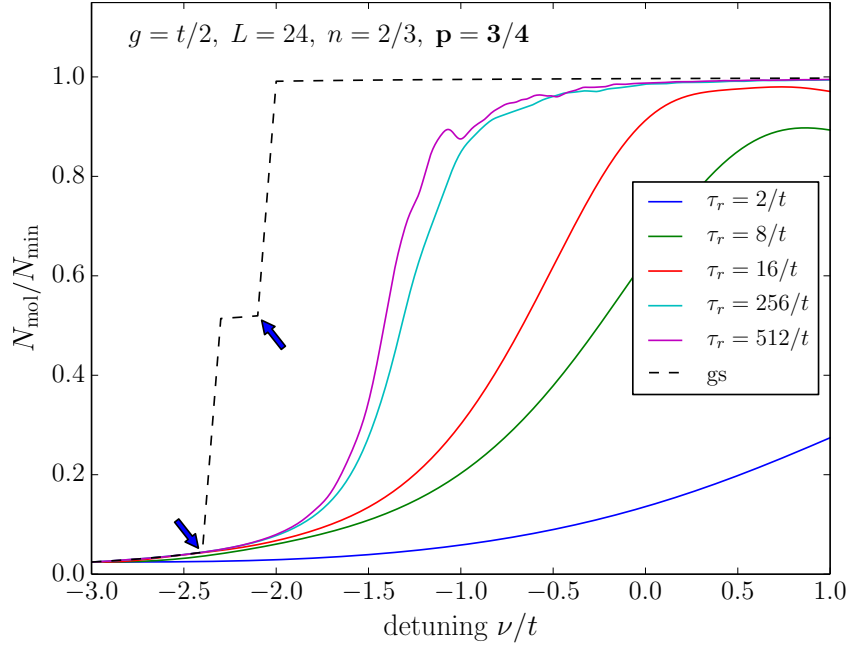


**Figure 4.4.:**  $N_{\text{mol}}/N_{\text{min}}$  vs detuning for  $p = 3/4$  and different ramp times. Dashed line corresponds to  $N_{\text{mol}}$  in the ground state.  $N_{\text{mol}}^0(\nu)$  features two kinks (indicated by the arrows) at  $\nu \approx -2.4t$  and  $\nu \approx -2.1t$ . (TEBD:  $D = 512$ ,  $\varepsilon = 10^{-8}$ ,  $n_{\text{steps}} = 2560$  ( $\tau_r \leq 256/t$ ) and  $n_{\text{steps}} = 5120$  ( $\tau_r = 512/t$ ). GS:  $D = 256$ ,  $\varepsilon = 10^{-8}$ ,  $\delta E = 10^{-8}t$ ,  $\tau_0 = 0.4/t$ ,  $\tau_f = 10^{-4}/t$ )

### 4.1.2. Momentum distribution function

As discussed in Section 1.2.3, one possible detection scheme for the observation of FFLO correlations would be the projection of the pair momentum distribution function  $n_k^{\text{pair}}$  which features FFLO correlations on the BCS side of the resonance onto the molecules on the BEC side, in order to probe their momentum distribution function,  $n_k^{\text{mol}}$ . Therefore, we define the momentum distribution function (MDF)

$$n_k = \frac{1}{L} \sum_{l,m} e^{-ik(l-m)} \rho_{lm}, \quad (4.3)$$

where  $k = n\frac{2\pi}{L}$  ( $n = -L/2 + 1, \dots, L/2$  for even  $L$ ) and  $\rho_{lm}$  is the one-particle density matrix (OPDM) defined as

$$\rho_{lm}^{\text{pair}} = \langle \hat{c}_{l,\uparrow}^\dagger \hat{c}_{l,\downarrow}^\dagger \hat{c}_{m,\downarrow} \hat{c}_{m,\uparrow} \rangle \quad (4.4)$$

$$\rho_{lm}^{\text{mol}} = \langle \hat{m}_l^\dagger \hat{m}_m \rangle. \quad (4.5)$$

Obviously,  $n_k$  is symmetric with respect to  $k = 0$  due to the hermiticity of the OPDM such that, in the following, we will only show the part of the MDF with non-negative momentum.

We first have a look at the molecule momentum distribution function of the ground state, reproducing the results of [44]. On the BCS side, as a consequence of the FFLO correlations, the molecule momentum distribution function is also peaked at the FFLO wavevector  $q = \pi np$  (Fig. 4.5a). On the BEC side of the resonance (Fig. 4.5b), as expected,  $n_k^{\text{mol}}$  is peaked around  $k = 0$  indicating that the particles form a condensate. The disappearance of the FFLO correlations happens at  $\nu \approx -2.4t$ , where we also found a kink in the number of molecules in the ground state (Fig. 4.4). This point is associated with the phase boundary between the FFLO phase and the intermediate BEC+PP LL phase as discussed in [44].

### MDF during ramp

The momentum distribution function of the molecules,  $n_k^{\text{mol}}$ , during the ramp is shown in Fig. 4.6 for various ramp times and a polarization of  $p = 3/4$ . For this polarization and a density of  $n = 2/3$ , the FFLO peak is expected at  $q = \pi/2$ . For small ramp times,  $n_k^{\text{mol}}$  resembles its initial form which is peaked around  $k = q$  and has a tail for  $k \rightarrow 0$ . However, for intermediate ramp times,  $n_k^{\text{mol}}$  gets sharply peaked around  $k = q$  indicating that the

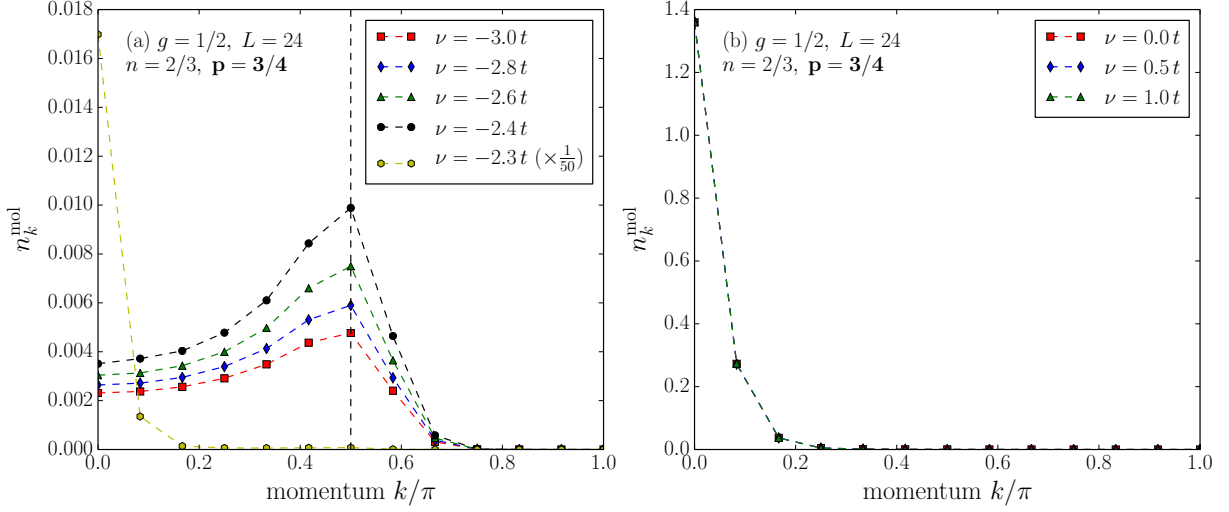


**Figure 4.5.:** (a)  $n_k^{\text{mol}}$  of the ground state on the BCS side of the resonance. Below  $\nu \approx -2.3t$ ,  $n_k^{\text{mol}}$  features FFLO correlations. The FFLO momentum,  $q = \pi/2$  is indicated by the dashed line. (b)  $n_k^{\text{mol}}$  of the ground state on the BEC side of the resonance. (TEBD:  $D = 256$ ,  $\varepsilon = 10^{-8}$ ,  $\delta E = 10^{-8}t$ ,  $\tau_0 = 0.4/t$ ,  $\tau_f = 10^{-4}/t$ )

FFLO correlations of the paired fermions have been projected onto the molecules. For larger ramp times ( $\tau_r = 256/t$ ), the peak is shifted towards smaller values of  $k$  and the momentum distribution function gets smeared out a little bit. For very large ramp times ( $\tau_r = 1024/t$ ), the peak almost completely vanishes and is shifted towards even smaller values of  $k$ .

For smaller polarizations ( $p = 1/2$  in Fig. 4.7), it can be seen that for intermediate ramp times,  $n_k^{\text{mol}}$  does not get peaked sharply around  $k = q$  but is smeared out. At the same time, the peak is shifted towards  $k = 0$  for smaller ramp times compared to the case of  $p = 3/4$ . In the limit of large ramp times, a BEC-like momentum distribution that is peaked around  $k = 0$  develops.

The molecule momentum distribution function for a smaller system of size  $L = 12$  is shown in Fig. 4.8 for  $p = 3/4$  and  $\tau_r = 32/t$  (a),  $\tau_r = 64/t$  (b) and  $\tau_r = 512/t$  (c). The results are directly compared to the ones obtained for the larger system ((d)-(f)), respectively. We observe similar behaviour for different system sizes for equal ramp times. For intermediate ramp times ( $\tau_r = 32/t$  and  $64/t$ ), for both system sizes, a peak develops at momentum  $k = q = \pi/2$ . For larger ramp times ( $\tau_r = 512/t$ ), the position of the peak gets shifted to smaller values, while in the case of the larger system, the peak is also smeared out and has a tail towards  $k = 0$ .

For the case of  $L = 12$  and  $p = 1/2$ , the figures are shown in Fig. D.3.

### Visibility

A quantity that is of experimental interest, too, is the so-called visibility of the momentum distribution function, which is defined as

$$V_{\text{mol}} = \frac{n_{k=q}^{\text{mol}} - n_{k=0}^{\text{mol}}}{n_{k=q}^{\text{mol}} + n_{k=0}^{\text{mol}}}. \quad (4.6)$$

Here,  $q$  is the momentum where the FFLO peak is expected. The visibility can also become negative, which means that the momentum distribution function is peaked around  $k = 0$  rather than  $k = q$ .

In Fig. 4.9, we compare the visibility  $V$  of  $n_k^{\text{mol}}$  for the case  $p = 1/2$  with the one of  $p = 3/4$  for different ramp times. It can be seen that for small ramp times, the visibility behaves equally in both cases. However, for intermediate ramp times ( $\tau_r = 32/t$  and  $\tau_r = 64/t$ ), the visibility for larger polarization reaches some constant value which is about as twice as large as its initial value while in the case of  $p = 1/2$ , the visibility at the end of the ramp is close to its initial value. For large ramp times ( $\tau_r = 256/t$ ) and  $p = 1/2$ , the visibility even becomes negative which is a consequence of the peak moving to  $k = 0$  and forming the above discussed BEC-like MDF.

A very interesting feature of the visibility for both polarizations is the maximum at  $\nu \approx -1.6t$ , after which the visibility drops except for the case of intermediate ramp times in the case of larger polarizations.

The strong oscillations for  $p = 3/4$  and  $\tau_r = 256/t$  are also present if we increase the number  $D$  of states kept during the truncation in the TEBD update process. This has been checked for  $D$  up to 1024, where we do not find any difference to the case of  $D = 512$  (see Fig. 4.11).

For a comparison between different system sizes, we show the visibility for  $p = 3/4$  in the case of  $L = 12$  (Fig. 4.10(a)) and  $L = 24$  Fig. 4.10(b)). For intermediate ramp times, the visibility at the end of the ramp is enhanced for both system sizes, while for long ramp times, the visibility drops for the larger system featuring oscillations. In addition, the visibility for the smaller system features very strong oscillations for large ramp times. This could be explained by the fact that the resolution for the momentum is very bad for this system size, where the spacing is given by  $\Delta k = \pi/6$ .

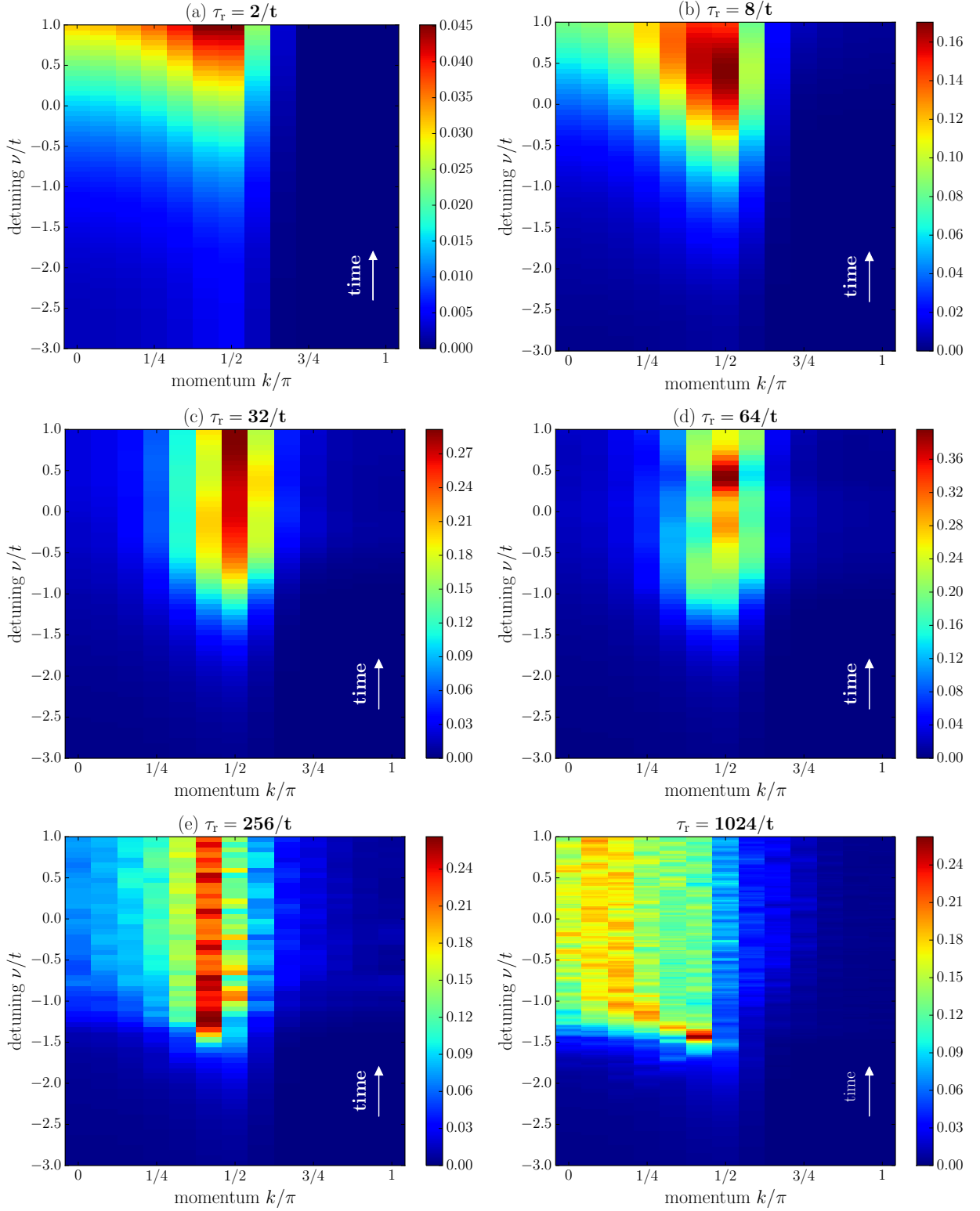


**Figure 4.6.:**  $n_k^{\text{mol}}$  during the ramp for  $\mathbf{p} = \mathbf{3}/4$  and different ramp times  $\tau_r$ . The white arrow indicates the direction of time. FFLO momentum is at  $k = q = \pi/2$ . (TEBD:  $g = t/2$ ,  $L = 24$ ,  $n = 2/3$ ,  $D = 1024$ ,  $\varepsilon = 10^{-8}$ ,  $n_{\text{steps}} = 2560$  ( $\tau_r \leq 256/t$ ) and  $n_{\text{steps}} = 10240$  ( $\tau_r = 1024/t$ ))

#### 4. Numerical Results

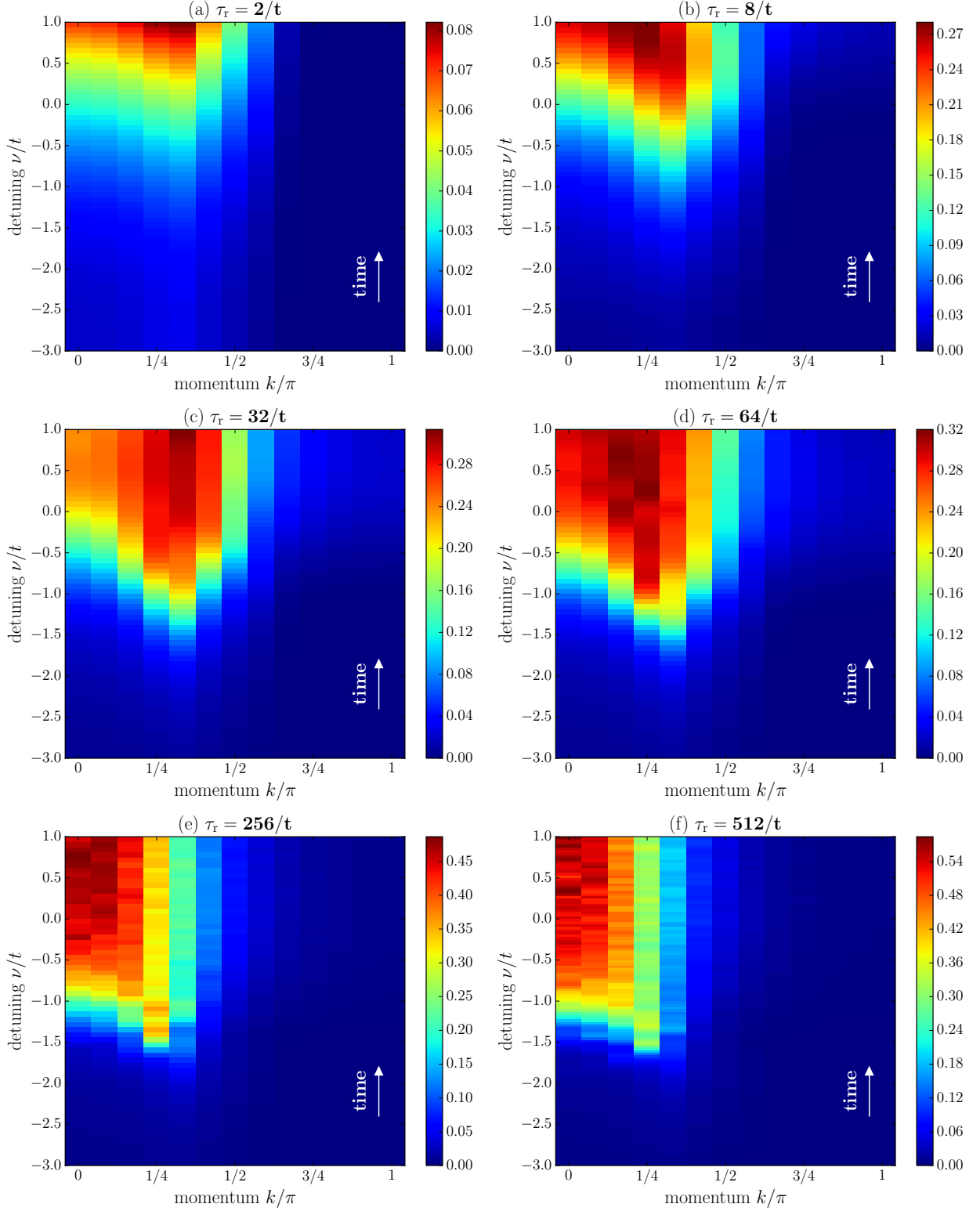


**Figure 4.7.:**  $n_k^{\text{mol}}$  during the ramp for  $\mathbf{p} = 1/2$  and different ramp times  $\tau_r$ . The white arrow indicates the direction of time. FFLO momentum is at  $k = q = \pi/3$ . (TEBD:  $g = t/2$ ,  $L = 24$ ,  $n = 2/3$ ,  $D = 1024$ ,  $\varepsilon = 10^{-8}$ ,  $n_{\text{steps}} = 2560$  ( $\tau_r \leq 256/t$ ) and  $n_{\text{steps}} = 10240$  ( $\tau_r = 1024/t$ ))

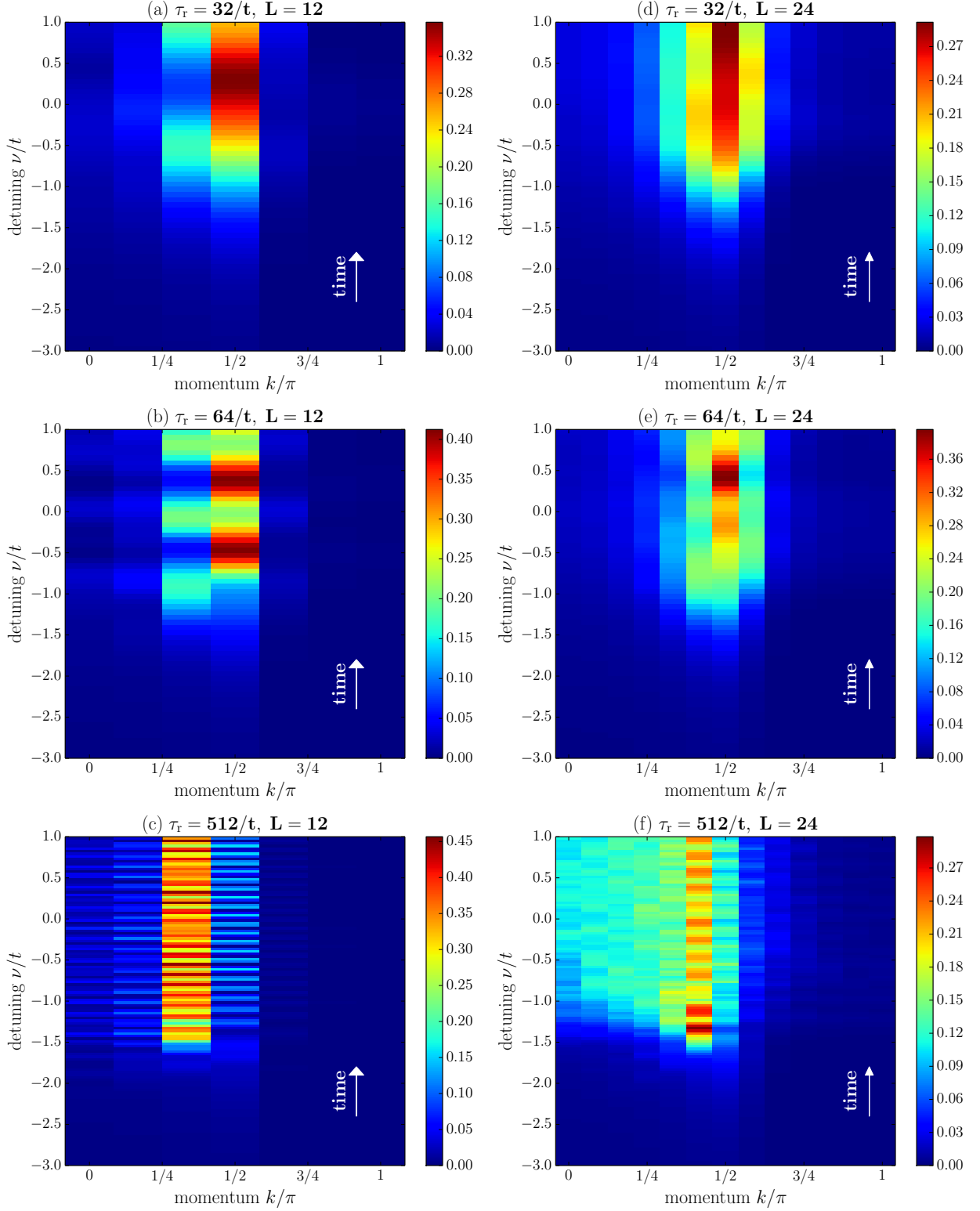


**Figure 4.8.:**  $n_k^{\text{mol}}$  during the ramp for  $\mathbf{p} = 3/4$ . (a)-(c):  $L = 12$ . (d)-(f)  $L = 24$ . The white arrow indicates the direction of time. FFLO momentum is at  $k = q = \pi/2$ . (TEBD:  $g = t/2$ ,  $n = 2/3$ ,  $D = 512$  ( $L = 12$ ),  $D = 1024$  ( $L = 24$ ),  $\varepsilon = 10^{-8}$ ,  $n_{\text{steps}} = 2560$  ( $\tau_r \leq 256/t$ ) and  $n_{\text{steps}} = 5120$  ( $\tau_r = 512/t$ ))

#### 4. Numerical Results

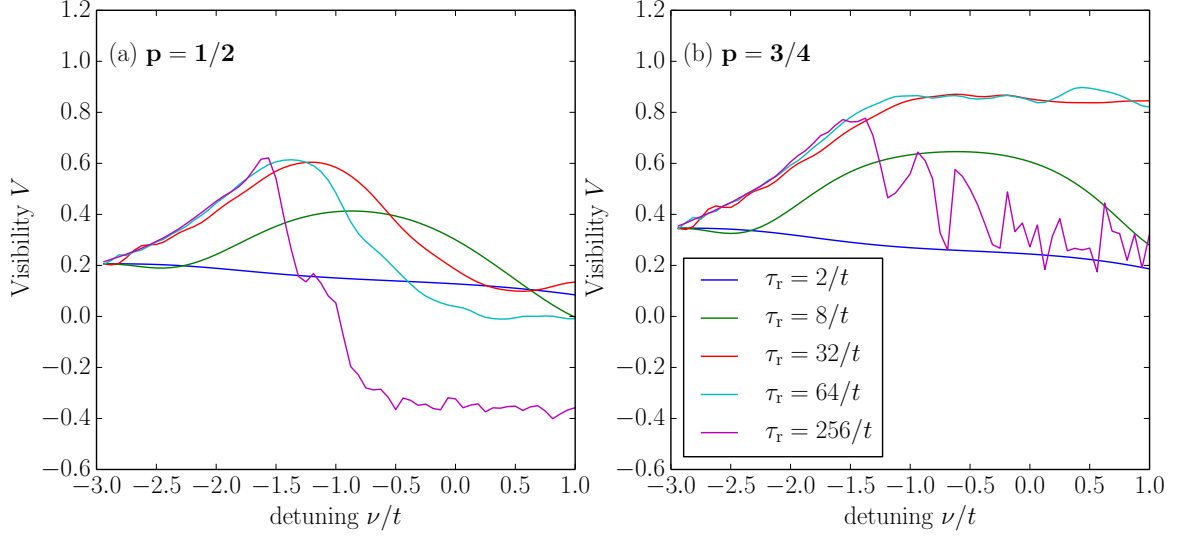


**Figure 4.9.:** (a) Visibility  $V_{\text{mol}}$  during ramp for  $\mathbf{p} = \mathbf{1/2}$  and different ramp times  $\tau_r$ . (b) Visibility  $V_{\text{mol}}$  during ramp for  $\mathbf{p} = \mathbf{3/4}$  and different ramp times  $\tau_r$ . (TEBD:  $g = t/2$ ,  $L = 24$ ,  $n = 2/3$ ,  $D = 1024$ ,  $\varepsilon = 10^{-8}$ ,  $n_{\text{steps}} = 2560$ )

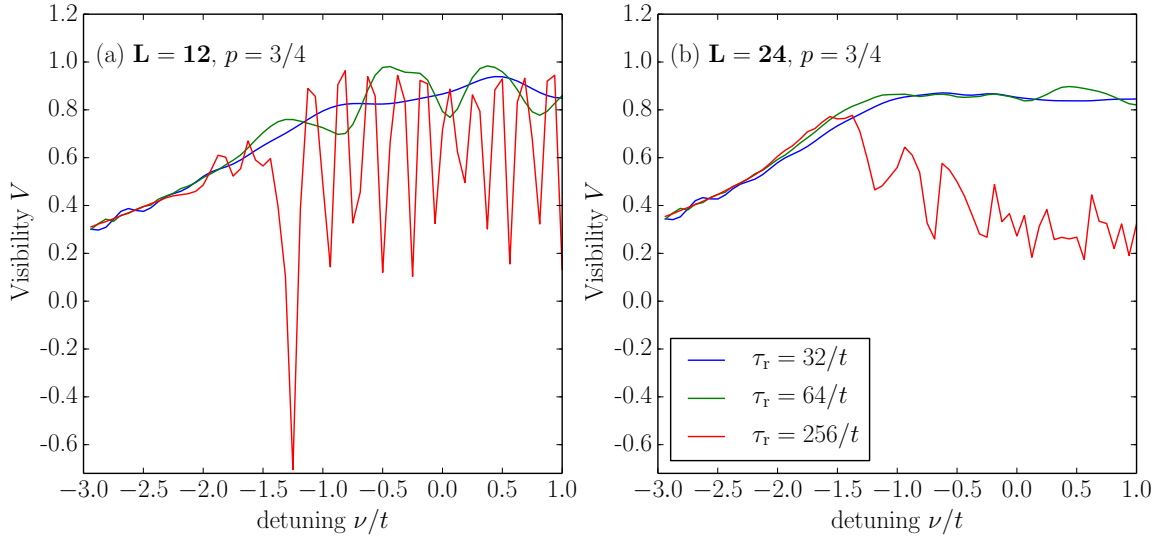


**Figure 4.10.:** Visibility  $V_{\text{mol}}$  during ramp for (a)  $\mathbf{L} = \mathbf{12}$  and (b)  $\mathbf{L} = \mathbf{24}$ , for a polarization of  $p = 3/4$ . (TEBD:  $g = t/2$ ,  $n = 2/3$ ,  $D = 1024$ ,  $\varepsilon = 10^{-8}$ ,  $n_{\text{steps}} = 2560$ )

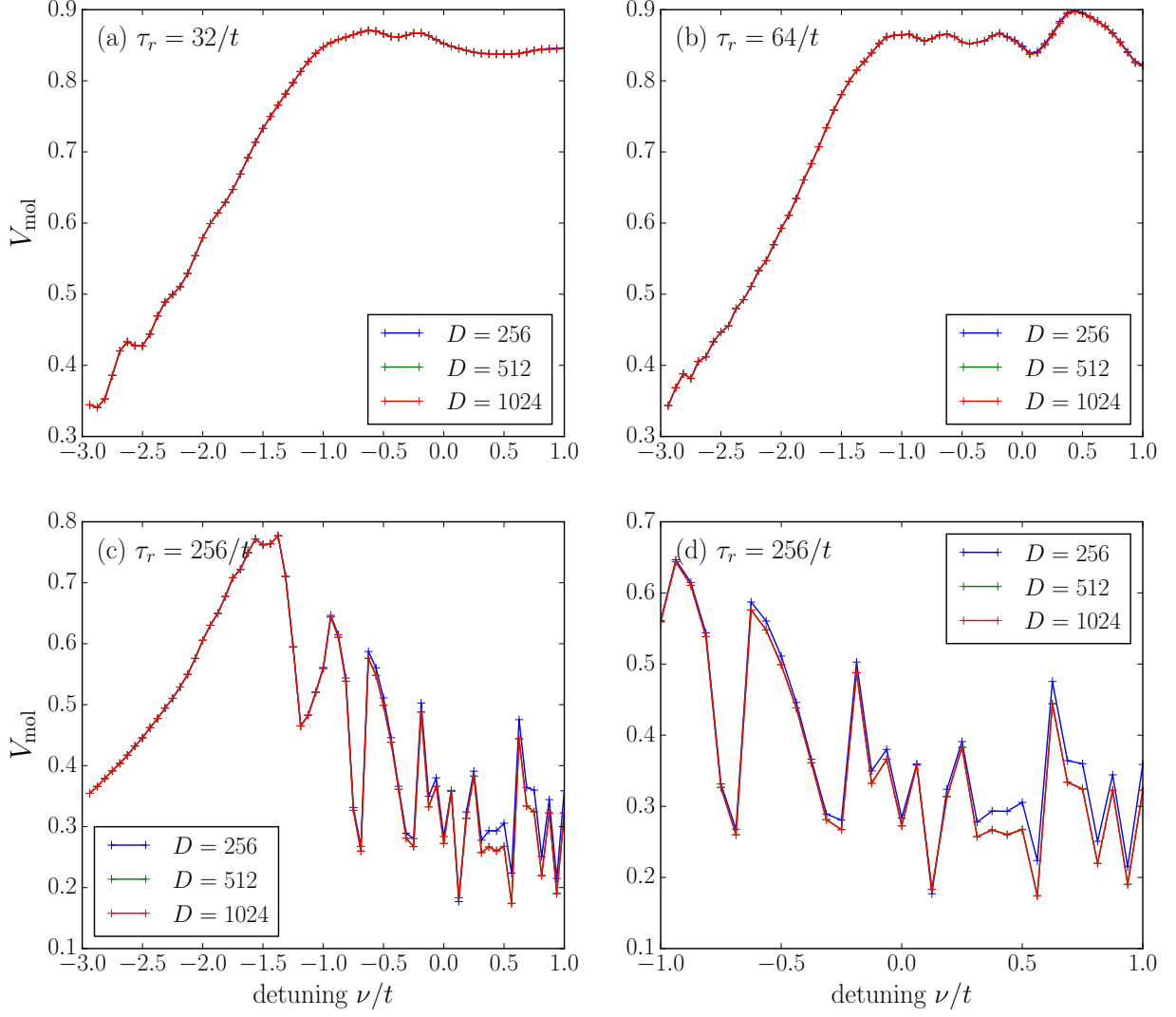


**Figure 4.11.:** Visibility  $V_{\text{mol}}$  for  $L = 24$  and  $\mathbf{p} = \mathbf{3}/4$ . (a),(b) For intermediate ramp times, the curves show no difference for different number of kept states. (c) For larger ramp times, at the end of the ramp, the curve shows no difference for  $D = 512$  and  $D = 1024$ . (d) Same as (c) but with enlarged region where errors occur. (TEBD:  $g = t/2$ ,  $n = 2/3$ ,  $\varepsilon = 10^{-8}$ )

### Comparison to previous work

The results obtained for the ramps across the resonance in the two-channel Bose-Fermi resonance model (BFRM) are in contrast to the ones obtained in [46], where both ramps and quenches have been studied in the single-channel Fermi-Hubbard model. While we observe an enhancing effect for intermediate ramp times, there, a monotonic decrease in the visibility of the FFLO correlations for increasing ramp times was observed. This can be explained by the fact that the single-channel model does not account for the possibility of having a phase with the coexistence of molecules and unpaired fermions close to the resonance.

Compared to the results in [45] for the BFRM, we get a similar correlation enhancing effect for intermediate ramp times. However, both for  $L = 12$  and  $L = 24$ , the visibility is not enhanced for intermediate polarization ( $p = 1/2$ ) at the end of the ramp and also the visibility drops for large ramp times for all polarizations opposed to the ED studies in [45], where the visibility is enhanced for intermediate ramp times and intermediate polarization. For large polarization, the visibility is also enhanced for large ramp times. Nevertheless, we want to stress, that we only focussed on the correlations during the ramp, while previous work [45, 46] was concerned with the long-time average after the ramp or the quench, respectively. In addition to that, we note that for our work, we used open boundary conditions while they were using periodic boundary conditions. Commenting on the numerical quality of our data, we want to emphasize that all of our results have been checked to be at least qualitatively independent of the truncation error and the Trotter error (see Appendix C).

### 4.1.3. Adiabaticity

In the discussion of the ramp dynamics in terms of the number of molecules as well as the momentum distribution function, we observed that in the long ramp time limit, the observables seemed to converge more and more to their ground state values at the end of the ramp. On the other hand, during the evolution, the dynamics is not adiabatic at all as can be seen from Fig. 4.2, Fig. 4.7 and Fig. 4.6.

This leads to the question whether one can bring up the notion of an 'adiabatic limit' in the sense that for infinitely long ramp times, all observables can become arbitrarily close to their ground state values. To this end, we look at the energy in order to determine where diabatic behaviour may come from and whether there is an 'adiabatic' limit in which the system suppresses any kind of excitation.

#### Energy during the ramp

In Fig. 4.12, we show the energy during the ramp for a polarization  $p = 3/4$  and different ramp times. For this polarization, the ground state energy has two kinks appearing related to the kinks in the number of molecules as seen in Fig. 4.2. At the first transition, the ramp energy overshoots the ground state energy and the system is not evolving adiabatically any longer. Asymptotically, the ground state energy is proportional to the detuning. Interestingly, the ramp energy also becomes proportional to the detuning for large ramp times and  $\nu \gtrsim -0.5t$ , but still has an offset with respect to the ground state energy that decreases with larger ramp times.

In order to analyze this behaviour for long ramp times and at the end of the ramp, we recall the Hamiltonian of the system in its time dependent version

$$\begin{aligned}
 H_{\text{BFM}}(T) = & -t \sum_i \sum_{\sigma} \left( \hat{c}_{i,\sigma}^{\dagger} \hat{c}_{i+1,\sigma} + \text{h.c.} \right) - \frac{t}{2} \sum_i \left( \hat{m}_i \hat{m}_{i+1} + \text{h.c.} \right) \\
 & - (\nu(T) + 3t) \sum_i \hat{m}_i^{\dagger} \hat{m}_i + g \sum_i \left( \hat{m}_i^{\dagger} \hat{c}_{i,\uparrow} \hat{c}_{i,\downarrow} + \text{h.c.} \right), \quad (4.7)
 \end{aligned}$$

where  $T$  denotes the time and  $\nu(T)$  is given in Eq. (4.1). The energy of the system then is given by

$$E(T) = E_{\text{kin}}(T) + E_{\text{fesh}}(T) - (\nu(T) + 3t)N_{\text{mol}}(T). \quad (4.8)$$

As we have seen in Fig. 4.2, the number of molecules saturates at the end of the ramp for large ramp times reaching its post-ramp ground state value such that the excess energy has

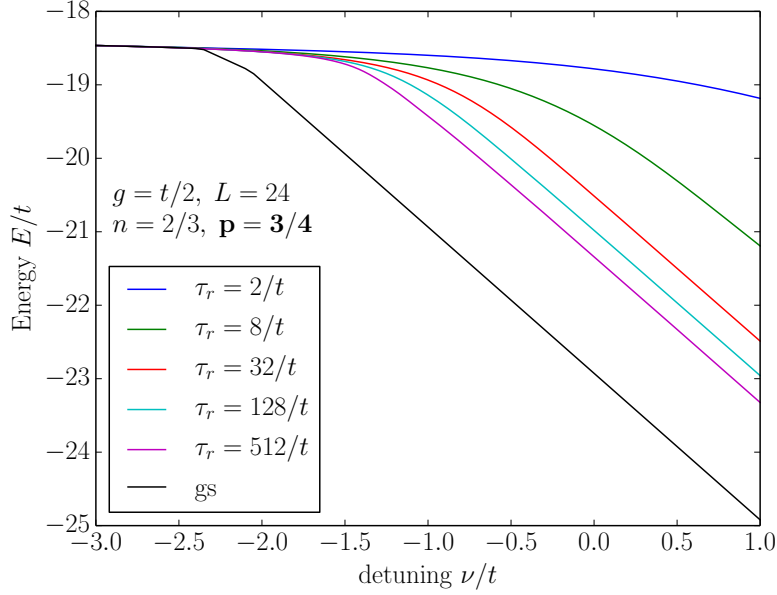


**Figure 4.12.:** Energy during the ramp for different ramp times  $\tau_r$  and a polarization of  $\mathbf{p} = \mathbf{3/4}$ . Black line corresponds to the ground state energy. (TEBD:  $g = t/2$ ,  $L = 24$ ,  $n = 2/3$ ,  $D = 1024$ ,  $\varepsilon = 10^{-8}$ ,  $n_{\text{steps}} = 2560$  ( $\tau_r \leq 256/t$ ) and  $n_{\text{steps}} = 5120$  ( $\tau_r = 512/t$ ) GS:  $D = 256$ ,  $\varepsilon = 10^{-8}$ ,  $\delta E = 10^{-8}t$ ,  $\tau_0 = 0.4/t$ ,  $\tau_f = 10^{-4}/t$ )

to come from the first two terms,  $E_{\text{kin}}(T)$  and  $E_{\text{fesh}}(T)$ . This also implies, that we have excitations in the system that can change the correlations of the many-body system. The excess energy of the system at the end of the ramp decreases with increasing ramp times.

As a measure for the excess energy, we introduce the rescaled energy, defines as

$$\bar{E}_{\text{res}}(T) = \frac{\langle \psi(T) | \hat{H}(T) | \psi(T) \rangle - \langle \psi_0 | \hat{H}(T) | \psi_0 \rangle}{\langle \psi_{\text{in}} | \hat{H}(T) | \psi_{\text{in}} \rangle - \langle \psi_0 | \hat{H}(T) | \psi_0 \rangle} = \frac{E(T) - E_0(T)}{E_{\psi_0}(T) - E_0(T)}. \quad (4.9)$$

Here,  $\hat{H}(T)$  denotes the Hamiltonian at some time  $T$  given in Eq. (4.7).  $|\psi(T)\rangle$  is the time evolved state at time  $T$ , while  $|\psi_0\rangle$  is the instantaneous ground state of the Hamiltonian  $\hat{H}(T)$ .  $|\psi_{\text{in}}\rangle$  is the initial state at the beginning of the ramp. With this definition,  $\bar{E}_{\text{res}}$  is directly proportional to the density of defects. The adiabatic limit is given by  $\bar{E}_{\text{res}} \rightarrow 0$ , while complete diabatic (impulse-like) behaviour is given by  $\bar{E}_{\text{res}} \rightarrow 1$ .

In Fig. 4.14 and Fig. 4.15, we compare the energy during the ramp and the evolution of the rescaled energy as a function of the instantaneous detuning for a large ramp time,  $\tau_r = 512/t$  and the polarizations  $p = 1/2$  and  $p = 3/4$ . First, we observe that at the beginning of the ramp, before the first transition point (indicated by the first dashed

line), the evolution is fully adiabatic. As soon as the first transition point is crossed, the evolution becomes more and more adiabatic due to the kink in the ground state energy. For intermediate polarization ( $p = 1/2$ ), there are four kinks in the ground state energy, where each kink corresponds to the creation of one additional molecule in the ground state. The first kink should correspond to the phase boundary between the FFLO phase and the BEC+PP LL phase as at this point, the peak at  $k = 0$  in the momentum distribution function becomes dominant. At the value of the detuning where the last kink appears, we observe the disappearance of  $N_{\min}$  in the ground state similar to the case of  $p = 3/4$  (cp. Fig. 4.4 and [44]). Thus, this kink should correspond to the phase boundary between BEC+PP LL and BEC+FP FG. Interestingly, in the small regions between the kinks, the rescaled energy seems to try to saturate before the next kink is hit. At the end of the ramp ( $\nu \rightarrow t$ ), the rescaled energy saturates at a non-zero value.

In the case of larger polarization ( $p = 3/4$  in Fig. 4.15), there are only two kinks in the ground state energy. However, the rescaled energy does not saturate between both transition points. Further, it can be seen that the slope of the rescaled energy does not change much compared to the intermediate phase between both transitions. This is interesting as it may be interpreted as if the first transition point is the dominant one, where all of the diabatic behaviour comes from. Nevertheless, this should be further studied by for example starting the ramp in the intermediate phase, only crossing the second point. At the end of the ramp, the rescaled energy saturates as in the case of smaller polarization.

## 4.2. Connection to Kibble-Zurek theory

As discussed in Section 2.2, in Kibble-Zurek theory, the density of defects obeys a power-law for large ramp times

$$n_{\text{ex}} \sim \tau_r^{-\frac{\nu}{1+\nu z}}. \quad (4.10)$$

The rescaled energy is directly proportional to the density of excitations or defects such that we can plot the excess energy as a function of the ramp time for different polarizations (Fig. 4.16). For very short ramp times, the behaviour is the same for each polarization where the limit  $\tau_r \rightarrow 0$  corresponds to a quantum quench such that the rescaled energy goes to unity indicating fully impulse-like behaviour. A possible explanation for this behaviour independent of  $p$  is that due to the very fast ramp time, the evolution of the system is impulse like as in a quantum quench such that the system itself has no notion of the exact structure of the critical region, in this case the intermediate BEC+PP LL phase.

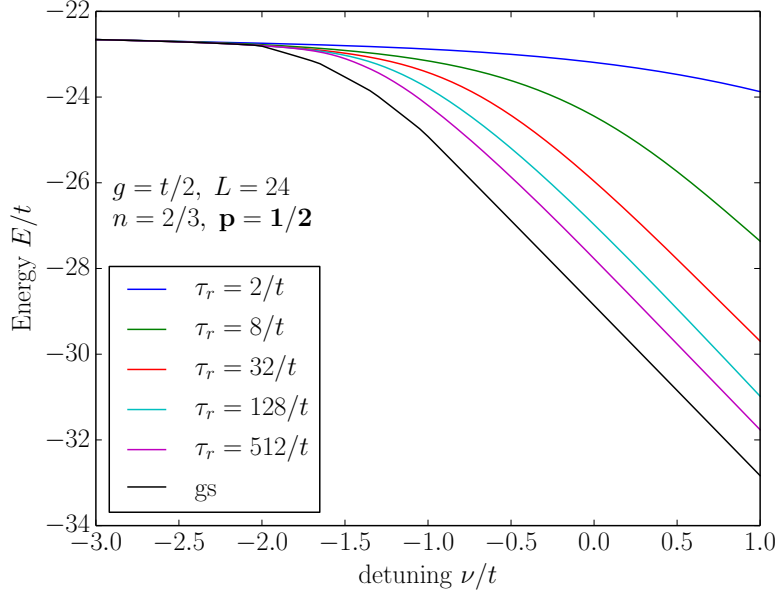


**Figure 4.13.:** Energy during the ramp for different ramp times  $\tau_r$  and a polarization of  $\mathbf{p} = \mathbf{1}/2$ . Black line corresponds to the ground state energy. (TEBD:  $g = t/2$ ,  $L = 24$ ,  $n = 2/3$ ,  $D = 1024$ ,  $\varepsilon = 10^{-8}$ ,  $n_{\text{steps}} = 2560$  ( $\tau_r \leq 256/t$ ) and  $n_{\text{steps}} = 5120$  ( $\tau_r = 512/t$ ) GS:  $D = 256$ ,  $\varepsilon = 10^{-8}$ ,  $\delta E = 10^{-8}t$ ,  $\tau_0 = 0.4/t$ ,  $\tau_f = 10^{-4}/t$ )

In the long ramp time limit<sup>2</sup>,  $1/\tau_r \rightarrow 0$ , however, the rescaled energy seems to obey the power-law expected from Kibble-Zurek theory with

$$\bar{E}_{\text{res}} \sim \tau_r^{-\frac{\nu}{1+\nu z}} = \tau_r^{-\alpha}. \quad (4.11)$$

By fitting the power-law behaviour with the data for the four largest ramp times (beginning with  $\tau_r = 128/t$ ), we extract the scaling exponents for a system size of  $L = 24$

$$\alpha(p = 1/4) \approx 0.40, \quad (4.12a)$$

$$\alpha(p = 1/2) \approx 0.38, \quad (4.12b)$$

$$\alpha(p = 3/4) \approx 0.15, \quad (4.12c)$$

with an error of about one percent in all three cases. Interestingly, the parameters for both polarizations,  $p = 1/4$  and  $p = 1/2$ , are approximately the same, while the exponent

<sup>2</sup>At least for ramp times up to  $\tau_r = 512/t$  for the smaller polarizations.

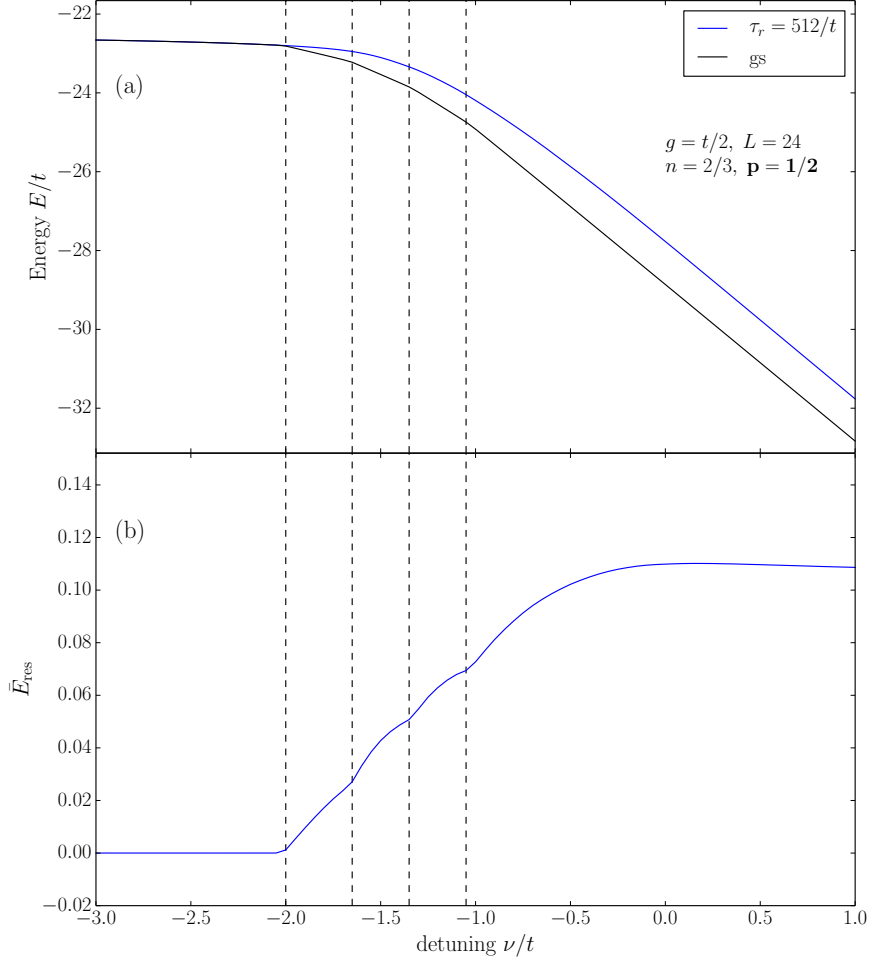


**Figure 4.14.:** (a) Ramp energy vs detuning for  $\mathbf{p} = 1/2$  and a ramp time of  $\tau_r = 512/t$ . Black line corresponds to the ground state energy. (b) Rescaled energy  $\bar{E}_{\text{res}}$  vs detuning for  $\mathbf{p} = 1/2$  and a ramp time of  $\tau_r = 512/t$ . Dashed lines indicate kinks in the ground state energy and have been determined by the kinks in  $N_{\text{mol}}$  and the disappearance of FFLO correlations in  $n_k^{\text{mol}}$  of the ground state (see Fig. 4.5). (TEBD:  $g = t/2, L = 24, n = 2/3, D = 1024, \varepsilon = 10^{-8}, n_{\text{steps}} = 2560$  ( $\tau_r \leq 256/t$ ) and  $n_{\text{steps}} = 5120$  ( $\tau_r = 512/t$ ) GS:  $D = 256, \varepsilon = 10^{-8}, \delta E = 10^{-8}t, \tau_0 = 0.4/t, \tau_f = 10^{-4}/t$ )

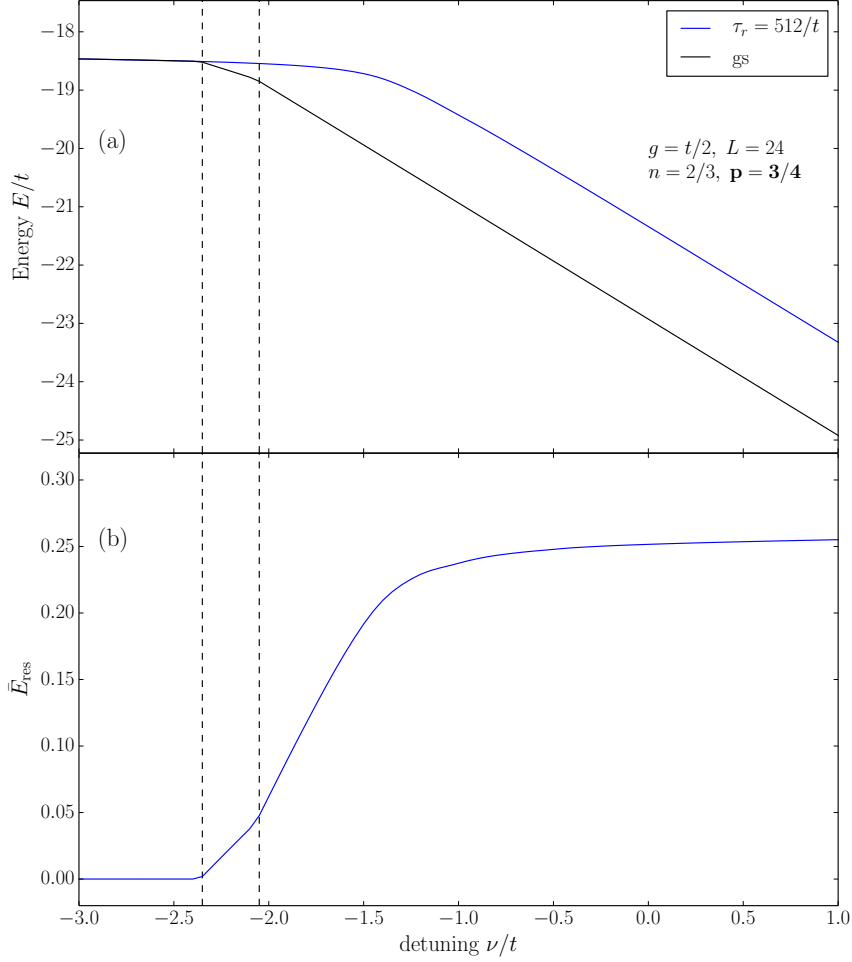


**Figure 4.15.:** (a) Ramp energy vs detuning for  $\mathbf{p} = \mathbf{3}/4$  and a ramp time of  $\tau_r = 512/t$ . Black line corresponds to the ground state energy. (b) Rescaled energy  $\bar{E}_{\text{res}}$  vs detuning for  $\mathbf{p} = \mathbf{3}/4$  and a ramp time of  $\tau_r = 512/t$ . Dashed lines indicate kinks in the ground state energy and have been determined by the kinks in  $N_{\text{mol}}$  (see Fig. 4.2) and the disappearance of FFLO correlations in  $n_k^{\text{mol}}$  of the ground state (see Fig. 4.5). (TEBD:  $g = t/2$ ,  $L = 24$ ,  $n = 2/3$ ,  $D = 1024$ ,  $\varepsilon = 10^{-8}$ ,  $n_{\text{steps}} = 2560$  ( $\tau_r \leq 256/t$ ) and  $n_{\text{steps}} = 5120$  ( $\tau_r = 512/t$ ) GS:  $D = 256$ ,  $\varepsilon = 10^{-8}$ ,  $\delta E = 10^{-8}t$ ,  $\tau_0 = 0.4/t$ ,  $\tau_f = 10^{-4}/t$ )

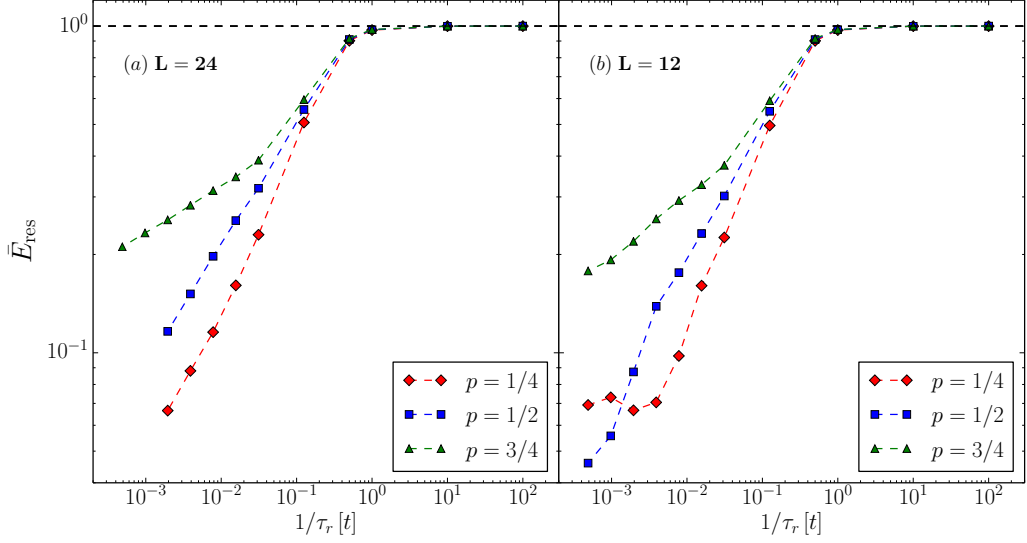


**Figure 4.16.:** (a) Rescaled energy  $\bar{E}_{\text{res}}$  as a function of the inverse ramp time for different polarizations and  $\mathbf{L} = 24$ . (TEBD:  $g = t/2$ ,  $n = 2/3$ ,  $D = 1024$ ,  $\varepsilon = 10^{-8}$ ,  $n_{\text{steps}} = 2560$  ( $\tau_r \leq 256/t$ ). For  $\tau_r \geq 512$ , we have  $\delta T = 0.1/t$ .) (b) Rescaled energy  $\bar{E}_{\text{res}}$  as a function of the inverse ramp time for different polarizations and  $\mathbf{L} = 12$ . (TEBD:  $g = t/2$ ,  $n = 2/3$ ,  $D = 512$ ,  $\varepsilon = 10^{-8}$ ,  $n_{\text{steps}} = 2560$  ( $\tau_r \leq 256/t$ ). For  $\tau_r \geq 512$ , we have  $\delta T = 0.1/t$ .)

for the largest polarization in our simulations,  $p = 3/4$  is significantly smaller. Another interesting feature is the kink in the curve for  $p = 3/4$  and a ramp time of  $\tau_r = 32/t$ .

Comparing the behaviour for different system sizes, we find that for a smaller system ( $L = 12$  in Fig. 4.16(b)), there is no adiabatic scaling in the large ramp time limit for small polarization and intermediate polarization, where the curves even cross. This behaviour persists also for larger  $D$  (checked for  $D = 800$ ).

For large polarization, the scaling of the rescaled energy seems to be almost adiabatic in the long ramp time limit, while for smaller polarization, there obviously is no adiabatic scaling. Thus, we can only extract the scaling exponents for  $L = 12$  and  $L = 24$  for  $p = 3/4$ ,

$$\alpha(p = 3/4, L = 12) \approx 0.19, \quad (4.13a)$$

$$\alpha(p = 3/4, L = 24) \approx 0.15. \quad (4.13b)$$

Interestingly, both exponents are very similar and an extension to larger systems would be of interest. Together with a proper finite-size scaling theory, one would be able to extract the scaling exponent in the thermodynamic limit. Another interesting aspect would be the

scaling exponents of smaller polarizations, in order to see whether they become equal for all polarizations in the thermodynamic limit.

In the discussion above, we have seen that Kibble-Zurek theory can be applied to our case, at least for the larger system we considered and up to ramp times  $\tau_r = 512/t$ . Nevertheless, one has to keep in mind that we are dealing with finite systems and not with the thermodynamic limit. For a finite system ( $L = 12$ ), there is a gap in all three phases that closes at the transition points [45]. Thus, an application of the Kibble-Zurek theory seems to be reasonable as we are dealing with the crossing of critical points, where the phases separated by the critical point are gapped. In such a case, the generation of excitations can be understood in terms of the Kibble-Zurek theory and the theory of Landau-Zener transitions (cf. Section 2.2).

However, these gaps are only present in the case of a finite system, while in the thermodynamic limit, the spectrum should be gapless, as we will see in the next section. Thus, it is not clear whether Kibble-Zurek theory really applies in the thermodynamic limit. This should be further investigated by either performing a proper finite-size analysis of the rescaled energy and the scaling exponents or by directly simulating the system in the thermodynamic limit with iTEBD [90], for example.

In addition, it would be interesting, whether for finite systems, in the long ramp time limit, there is some ramp time  $\tau_{\max}$  above which the rescaled energy saturates due to finite size effects. However, we were not able to find this limit in the case of a larger system (checked for  $\tau_r$  up to 2048 in the case of  $p = 3/4$ ). Clearly, it seems as if there is some limit for small polarizations for a small system ( $L = 12$ ), where also the other polarizations tend to saturate in the rescaled energy.

### 4.3. Central charge

In order to characterize the different phases that are crossed during the ramp, we study the spectrum of the different phases in the phase diagram given in Fig. 1.12 and extend the work done in [44]. For a coupling parameter of  $g = t$ , the binding energy at resonance is given by  $\varepsilon^* \approx 0.49t$ . We calculate the polarization curve  $p(h)$  for three different values of the detuning,  $\nu = -3t, -t, 0t$ , as in [44]. In Fig. 1.12, this corresponds to  $\nu' = -6, -2, 0$ . The curves are shown in Fig. 4.17.

For the largest negative detuning,  $\nu = -3t$ , we get a nearly linear increase of the polarization with increasing magnetic field. The linear dependence of the polarization on the magnetic field in attractively interacting fermionic systems in 1D is consistent with [99, 100].

Right at resonance,  $\nu = 0$ , the polarization is zero up to a critical field  $h_c$  associated with the spin gap  $\Delta = 2h_c$  [22] and the polarization follows a square root behaviour,  $p(h) \propto \sqrt{h - h_c}$  near the critical field, consistent with [44]. Above the critical field, the molecules form a BEC that is immersed in a fully polarized Fermi gas.

For a detuning  $\nu = -t$  right below resonance (Fig. 4.17(b)), we also identify a spin gap. In addition, two kinks in the polarization curve occur (indicated by the arrows). These kinks indicate the phase boundaries between the 1D FFLO phase and the BEC+PP LL phase, as well as the BEC+FP FG phase (cf. Fig. 1.12). A finite-size scaling analysis performed in [44] shows that the critical fields associated with the two kinks are well separated and the difference remains finite in the thermodynamic limit [44].

The spectrum of the different phases can be studied by calculating the so-called central charge coming from conformal field theory (CFT), which can be seen as a measure for the number of gapless excitations in a system. It can be calculated from the entanglement entropy of a system by the Calabrese-Cardy formula [101] for open boundary conditions

$$S = \frac{c}{6} \log \left( \frac{L}{\pi} \sin \left( \frac{\pi l}{L} \right) \right) + S_b, \quad (4.14)$$

where  $c$  is the central charge,  $L$  is the system size,  $l$  is the bond at which the entropy is calculated and  $S_b$  is associated with the boundary entropy [102].

In Fig. 4.18, we plot the entropy profiles for a detuning of  $\nu = -t$  for selected values of the magnetic field. For vanishing magnetic field, we are in the standard BCS regime, where one expects a central charge  $c = 1$ . This is due to the fact that in a one-dimensional two-

component Fermi gas with equal spin population ( $p = 0$ ), we have spin-charge separation with the charge (density) excitations being gapless, while the spin excitations are gapped due to the formation of Cooper pairs. Such a system is known as a Luther-Emery liquid [58]. Fitting the entropy profile with Eq. (4.14), we get a slightly larger value  $c = 1.38 \pm 0.07$ . However, we want to stress that shrinking the fitting region leads to values, that are closer to unity with a similar error such that the deviation from the expected value may come from the oscillating contributions at the edges of the profile.

In the FFLO phase ( $h/t = 0.4$ ), we get a central charge  $c \approx 2$  as the spin gap closes for finite polarization. The fitting value also depends on the fitting region and is slightly smaller for smaller fitting regions.

In the intermediate phase, where molecules and paired fermions coexist ( $h/t = 0.75$ ), we get a central charge of  $c \approx 3$ . From the physical point of view, we have paired fermions in the FFLO phase coexisting with molecules in a BEC. The fermions behave like a Luttinger liquid, where both the spin and charge excitations are gapless. In addition, the molecules add one gapless excitation in the form of sound modes.

In the BEC+FP FG, one would again expect a central charge of  $c = 2$ , however, the entropy profiles,  $S_{vN}(l)$ , in this phase are unable to verify this.

At very large magnetic fields ( $h/t = 2.5$ ), the system is fully polarized and the central charge is close to unity again.

For a system deep in the BEC phase ( $\nu = 5t$ ) (Fig. 4.19), we find a central charge  $c \approx 1$ . In this case, we have a BEC of molecules that behave like hard-core bosons and form a so-called Tonks-Girardeau gas, where we only have one gapless excitation [103].

### 4.3.1. Consequences for a Kibble-Zurek interpretation

From the discussion about the central charge, we have seen that the spectrum in the thermodynamic limit is gapless with two gapless excitations in the FFLO and the BEC+FP FG phase and three gapless excitations in the intermediate BEC+PP LL phase. From this point of view, it is not clear whether Kibble-Zurek theory still can be applied in the thermodynamic limit. In Section 4.2, we have observed adiabatic scaling for a system with  $L = 12$  and  $L = 24$  at least for ramp times up to  $\tau_r = 1024/t$ . Interestingly, the scaling exponent is smaller for a larger system which is why a finite-size scaling of the exponents would be of interest in order to see whether the scaling exponent is still finite in the thermodynamic limit or approaches zero. Of further interest would be the relation to the kink appearing in the rescaled energy around  $\tau_r \approx 32/t$  as for these ramp times,

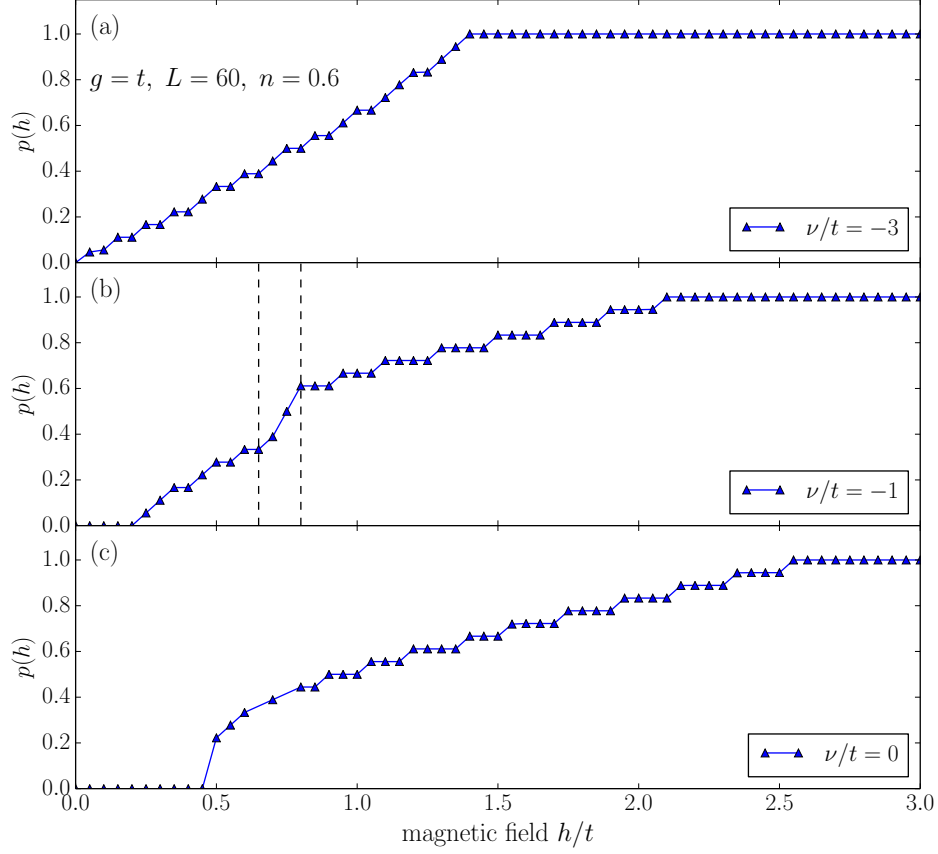


**Figure 4.17.:** Polarization curves  $p(h)$  for different detunings (a)  $\nu = -3t$ , (b)  $\nu = -t$  and (c)  $\nu = 0t$ . (a): The polarization increases almost linearly with the applied magnetic field until the system is fully polarized. (b): For small magnetic field, there is a small spin gap. At  $h/t \approx 0.65$  and  $h/t \approx 0.8$ , the polarization features two kinks in accordance with [44]. (c): For small magnetic field, there is a spin gap, after which the polarization scales like  $p \sim \sqrt{h - h_c}$  (cf. [44]). ( $D = 256$ ,  $\varepsilon = 10^{-8}$ ,  $\delta E = 10^{-8}t$ ,  $\tau_0 = 0.4/t$ ,  $\tau_f = 10^{-4}/t$ )

the visibility has been found to be enhanced at the end of the ramp. Then, if the scaling exponent decreases further with increasing system size, it might be possible to observe the FFLO correlations in the momentum distribution at even larger ramp times.

#### 4. Numerical Results

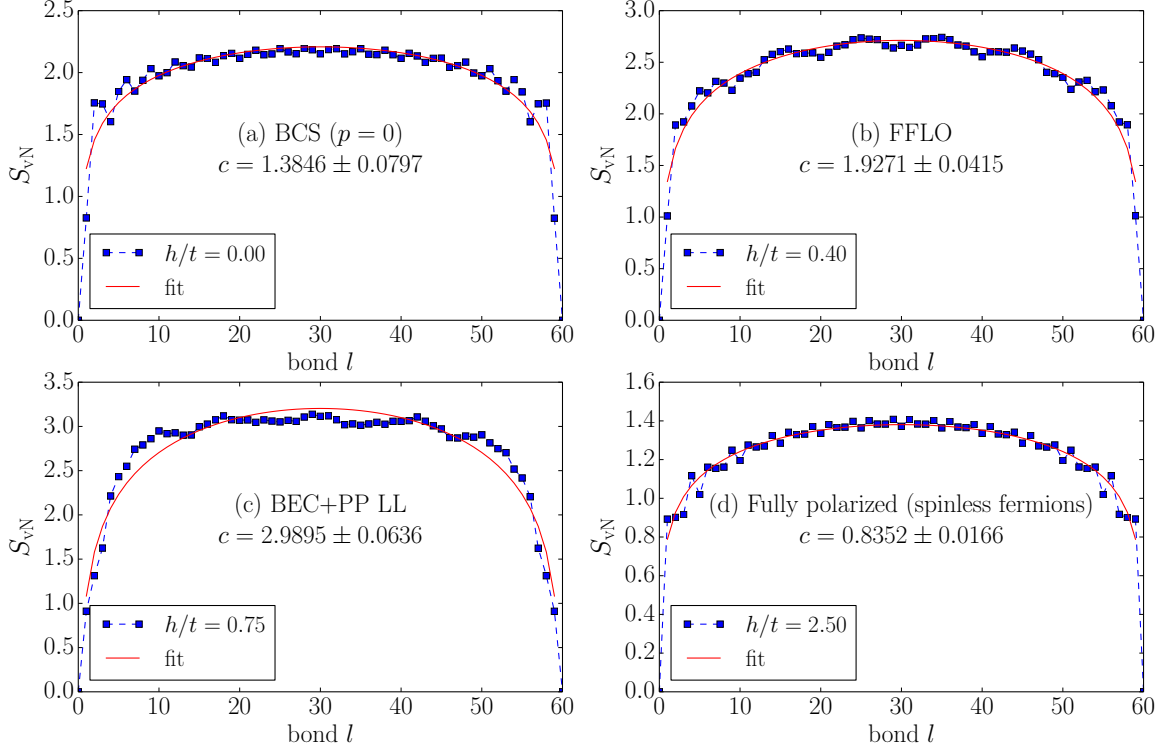


**Figure 4.18.:** Entropy profiles for  $L = 60$ ,  $n = 0.6$ ,  $g = t$  and  $\nu = -t$ . (a) Vanishing magnetic field corresponds to BCS-BEC phase in Fig. 1.12. (b)  $h/t = 0.4$  corresponds to the FFLO phase, (c)  $h/t = 0.75$  corresponds to the intermediate BEC+PP LL phase and (d)  $h/t = 2.5$  corresponds to the fully polarized phase with spinless fermions. For the BEC+FP FG phase, our data did not allow for the determination of the central charge. ( $D = 256$ ,  $\varepsilon = 10^{-8}$ ,  $\delta E = 10^{-8}t$ ,  $\tau_0 = 0.4/t$ ,  $\tau_f = 10^{-4}/t$ )

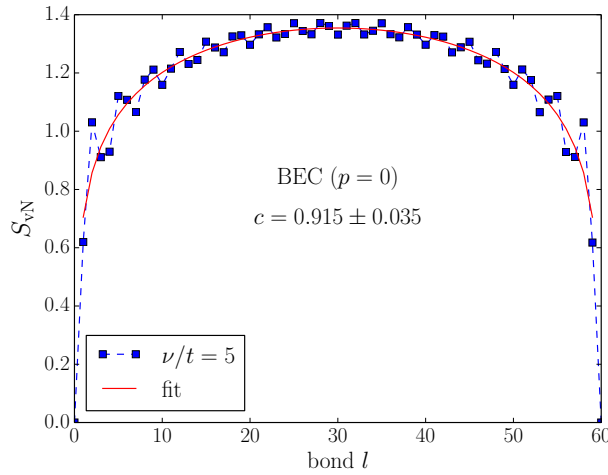


**Figure 4.19.:** Entropy profile for the ground state in the BEC phase at  $p = 0$  and  $\nu = 5t$ . ( $L = 60$ ,  $n = 0.6$ ,  $g = t$ ,  $D = 800$ ,  $\varepsilon = 10^{-8}$ ,  $\delta E = 10^{-8}t$ ,  $\tau_0 = 0.4/t$ ,  $\tau_f = 10^{-4}/t$ )

## 4.4. Summary

In this chapter, we studied the non-equilibrium dynamics in the Bose-Fermi resonance model by numerically simulating the system when ramping from the BCS side onto the BEC side of the resonance. To this end, we first determined the size of the resonance region for the parameters used ( $L = 24$ ,  $n = 2/3$ ,  $g = t/2$ ), in order to set the range of the detuning for the ramp. The parameters were chosen such that a comparison to [45] is easier.

During the ramp, we observed that the number of created molecules depends on the ramp time and saturates for long ramp times, independent of the polarization of the system. We also compared the time evolution of the number of molecules during the ramp with the ground state value, finding diabatic behaviour during the ramp, while the number of molecules reaches the ground state value at the end of the ramp for large ramp times.

For the momentum distribution function, we found that FFLO correlations are present and enhanced in the molecule momentum distribution function at large polarization,  $p = 3/4$  and intermediate ramp times. For larger ramp times, the position of the FFLO peak is shifted towards the ground state value of the BEC at  $k = 0$ . Compared to the case of quenches and ramps in the Fermi-Hubbard model done in [46], we found a correlation enhancing effect for large polarization and intermediate ramp times, both for  $L = 12$  and  $L = 24$ . Our observations, however, are not in complete accordance to the results obtained in [45], where the BFRM was studied using ED. There, a correlations enhancing effect even for intermediate polarization and intermediate ramp times was found. Concerning the quality of our numerical data, we want to point out that all results are at least qualitatively independent of the number of states kept during the ramp (truncation error) and the time step chosen (Trotter error). For an error analysis, we refer to Appendix C. One possible explanation for the different behaviour compared to [45] for the same model may be the use of different boundary conditions (we use open boundary conditions, while in [45] there were used periodic boundary conditions). Further, we only looked at the MDF during the ramp, while in [45], the long time average after the ramp was studied.

In order to understand the emergence of adiabatic behaviour in the long ramp time limit, we studied the energy during the ramp, as well as the properly rescaled energy as a quantity directly related to the density of defects in the system. In line with the observations for the number of molecules during the ramp, we observed beginning diabatic behaviour as soon as the first phase boundary is hit. For long ramp times, at the end of the ramp,

the energy is shifted with respect to the ground state energy which we interpret as the change in correlations of the system. For the rescaled energy, we additionally observed adiabatic scaling in the long ramp time limit, where we also extracted the power-law exponent. Interestingly, this exponent is approximately the same for  $p = 1/4$  and  $p = 1/2$ , while it is significantly smaller for  $p = 3/4$ . This should be compared with the enhanced FFLO correlations during the ramp, as a smaller exponent is connected with less adiabatic behaviour. However, one should be careful with these results, as we only studied a rather small system such that all results have to be confirmed for even larger system sizes. Up to now, it seems that Kibble-Zurek theory may be applied here.

Additionally, in order to characterize the phases that are crossed during the ramp, we calculated the central charge of the different phases, which is connected with the number of gapless excitations in the system. We found that for the FFLO phase, the central charge is  $c = 2$ , with both the spin as well as the charge excitations being gapless in the polarized case. In the intermediate phase (BEC+PP LL), we found  $c = 3$ , which is expected as the molecules also exhibit one gapless excitation (sound modes). For the BEC+FP FG phase, we were unable to extract the central charge from our data. We further discussed the consequences for a possible interpretation of our results for the rescaled energy in terms of the Kibble-Zurek theory.

# Summary

In this thesis, we studied the non-equilibrium dynamics of a spin-polarized Fermi gas with resonant interaction in one dimension. As the underlying model, we used the Bose-Fermi resonance model (BFRM). The thesis itself is motivated by experiments in spin-polarized ultracold Fermi gases and the desired experimental observation of the theoretical predicted FFLO phase and extends an earlier ED analysis [45].

For the relevant numerical simulations, we implemented from scratch Vidal's Time Evolving Block Decimation algorithm (TEBD) [47, 48] in the Python programming language. The code provided the use of conserved quantum numbers,  $N$  and  $S_z$ , in order to improve the performance. For the calculation of ground states, we used the imaginary-time evolution. Using the  $XXZ$ -model, we tested the code and compared numerical results to analytical values for the time evolution after a quench as well as the ground state energy with the TEBD algorithm and the extension for translationally invariant systems, iTEBD. The general theory of the TEBD algorithm in terms of Matrix Product States (MPS) was reviewed in Chapter 3. We further included a discussion about the use of conserved Abelian quantities.

The physics of the FFLO phase [1, 2], especially its characteristic correlations and the pairing mechanism was reviewed. We further discussed the two-channel Bose-Fermi resonance model [39, 40], which encompasses the resonance region of the BCS-BEC crossover in a quasi-1D geometry correctly and includes a molecular channel in addition to the fermionic one used in the Gaudin-Yang model.

In order to account for the quantum phase transitions appearing in the spin-imbalanced case, we shortly reviewed the Kibble-Zurek mechanism [49–51, 68–70], which provides a framework to study time-dependent crossings of (quantum) phase transitions with finite velocity and provides a quantitative description for the density of created defects in terms of a power-law scaling. Recent experiments [83] and extensions to extended critical regions [87] were mentioned, too.

For the numerical results, we performed ramps across the resonance region, starting from the BCS side of the resonance, in order to see whether one can project the FFLO correlations of the pairs on the BCS side onto the molecules on the BEC side of the resonance and to verify the results found in [45]. Using the TEBD algorithm, we found that the number of molecules created during the ramp saturates at its maximum value at the end of the ramp even for intermediate ramp times, independent of the polarization used. For the momentum distribution function (MDF) of the molecules, we found that for large polarizations ( $p = 3/4$ ), the FFLO correlations of the molecules are strongly enhanced only for intermediate ramp times while the position of the characteristic peak in the MDF gets shifted towards the ground state value,  $k = 0$ , for large ramp times. For smaller polarizations, we have not observed such an effect.

In contrast to the case of interaction quenches and linear ramps in the single-channel Fermi-Hubbard model done in [46], where a monotonic decay of the time-averaged post-ramp visibility with increasing ramp time was found, we observed, using the two-channel BFRM, a correlation enhancing effect in the molecule momentum distribution function for intermediate ramp times and large polarization. These results, however, are not in full accordance with [45], where a correlation enhancing effect was found for intermediate ramp times and intermediate polarization. A possible explanation of this discrepancy could lie in the different use of boundary conditions (periodic BC in [45] compared to open BC in this thesis) or in the fact that we studied the momentum distribution during the ramp, while in the previous work, the post-quench average was studied. Concerning the quality of our data, we want to point out that all results shown in this thesis were checked to be at least qualitatively independent of the number of states kept during the update process as well as the time step, resulting in the Trotter error.

The question of adiabaticity in the context of crossing a quantum phase transition with finite velocity was addressed by looking at the energy during the ramp as well as a quantity, that we called the rescaled energy, which is directly related to the density of defects in the system. In the long ramp time limit, we found adiabatic scaling with power-law exponents that were similar for smaller polarizations ( $p = 1/4, 1/2$ ) but significantly smaller for large polarizations ( $p = 3/4$ ). Analyzing the different phases, we calculated the central charge of those phases and found that the FFLO phase exhibits two gapless excitations (spin and charge) as expected [23]. On the BEC side, we also expect the same number of gapless excitations which, however, we were not able to verify from our data. In the intermediate phase, we found that this phase exhibits three gapless excitations. However, we still lack

an understanding of how the number of gapless excitations and the adding of a mode in the intermediate phase is related to the applicability of the Kibble-Zurek mechanism and the enhancing of FFLO correlations for intermediate ramp times and large polarizations.

All of the results were obtained using rather small system sizes such that the effects have to be confirmed for larger systems in order to make reliable predictions for experiments. In addition, trapping potentials have to be included to account for the actual experimental setup. Another important aspect is the post-ramp dynamics which has not been addressed in this thesis but is important as the correlations in the molecule MDF may get lost during the time evolution after the ramp.



# A. Implementation details

In this section of the appendix, we want to give an overview of the implementation of the TEBD algorithm and discuss some of the details not covered in the main chapter.

The core part of the code consists of two classes (QN\_MPS and QN\_TEBD) and two modules (QN\_TENSOR and QN\_INDEX). Further, model specific modules with corresponding operators also in quantum number conserving format were written for the XXZ-model and the BFRM.

All of the code uses conservation of quantum numbers in order to speed up calculations. Up to now only total particle number and total spin conservation have been implemented whereby implementations of further conserved quantities is straightforward.

## Modules

### QN\_MPS

This class creates an instance `qn_mps` that contains an MPS that respects the conservation of quantum numbers. Tensors on each site have block structure and are labeled by  $(N(\sigma), N(a_{l-1}), N(a_l))$  where the block labels are calculated by QN\_INDEX according to the given model. It takes as input parameters:  $d, D, (N, S_z), L$ .

Usually, the MPS is initialized in random and unnormalized form but other initial states like the Néel state for the XXZ-model and some polaron configurations for the BFRM can be chosen.

This class also includes methods for saving and loading the MPS in compressed and uncompressed format. It also provides a method to calculate the entanglement entropy at a given bond.

## **QN\_TEBD**

This class contains functions for performing time evolution (real and imaginary) as well as calculation of expectation values with local operators, operators in MPO form, overlaps for wavefunctions and calculation of correlators.

Several functions like calculation of local expectation values and correlators have been optimized if the MPS is in Vidal representation. It also provides a function to transform the MPS in Vidal representation.

The class uses the quantum number conserving tensor operations defined in `QN_TENSOR`.

## **QN\_TENSOR**

In this class, all basic tensor operations (contraction, inverting, reshaping) are included in a way that conserves the block structure and keeps track of the quantum numbers.

## **QN\_INDEX**

The index class calculates all possible indices and the labels for the MPS. To this end, the local contribution of the physical indices  $N(\sigma)$  as well as possible degeneracies have to be known and are included for the XXZ model and the BFRM.

## **Model specific modules**

In the model specific modules, operators and Hamiltonians with respect to a certain basis which respects the conservation of quantum numbers are defined. In addition, operators are stored as dictionaries with physical indices as keys and the corresponding matrix elements as values.

For this thesis, the XXZ model as a test model and the BFRM have been implemented.

## **Tensor operations**

The basic operations for the simulation of quantum systems with the TEBD algorithm are SVDs, tensor contractions and the reshaping of tensors. In order to preserve the quantum number conserving block structure of the MPS and to keep track of all indices, it is necessary to implement corresponding quantum number conserving tensor functions. In this section, we will discuss how these functions can be implemented. Of course, there may be other, even

---

better, implementations also depending on the language one uses. In this sense, Python is by far not an optimal language as we are forced to define matrix multiplication in Python instead of being able to push it to pure C using Numpy and LAPACK.

## Tensor contraction

In the TEBD algorithm, we are faced with tensor contractions like

$$M_{a_{l-1}, a_{l+1}}^{\sigma_l, \sigma_{l+1}} = \sum_{a_l} B_{a_{l-1}, a_l}^{\sigma_l} B_{a_l, a_{l+1}}^{\sigma_{l+1}}. \quad (\text{A.1})$$

For tensors in block structure, the sum can be rewritten in the following way

$$M_{N_{l-1}, N_{l+1}}^{\sigma_l, \sigma_{l+1}} = \sum_{N_l} B_{N_{l-1}, N_l}^{\sigma_l} B_{N_l, N_{l+1}}^{\sigma_{l+1}}, \quad (\text{A.2})$$

where we use  $\sigma_l$  also as a shorthand notation for  $N(\sigma_l)$  which should be clear by context. The sum now runs over all the blocks with quantum number  $N_l$  as last or second index, respectively. However, each block itself has to be contracted in the appropriate way as in a usual tensor multiplication. Schematically, this can be seen in Eq. (A.3), where a contraction like in Eq. (A.2) is shown and the resulting blocks have labels  $(N(\sigma_l), N_{l-1}, N(\sigma_{l+1}), N_{l+1})$ .

$$\sum_{N_l} B_{N_{l-1}, N_l}^{\sigma_l} B_{N_l, N_{l+1}}^{\sigma_{l+1}} = \begin{Bmatrix} (0, 0, 0) \\ (0, 1, 1) \\ (1, 0, 1) \\ (1, 1, 2) \end{Bmatrix} \cdot \begin{Bmatrix} (0, 1, 1) \\ (0, 0, 0) \\ (0, 2, 2) \\ (1, 0, 1) \\ (1, 1, 2) \\ (1, 2, 3) \end{Bmatrix} = \begin{Bmatrix} (0, 0, 0) \star (0, 0, 0) \\ (0, 0, 0) \star (1, 0, 1) \\ (0, 1, 1) \star (0, 1, 1) \\ (0, 1, 1) \star (1, 1, 2) \\ (1, 0, 1) \star (0, 1, 1) \\ (1, 0, 1) \star (1, 1, 2) \\ (1, 1, 2) \star (0, 2, 2) \\ (1, 1, 2) \star (1, 2, 3) \end{Bmatrix} = \begin{Bmatrix} (0, 0, 0, 0) \\ (0, 0, 1, 1) \\ (0, 1, 0, 1) \\ (0, 1, 1, 2) \\ (1, 0, 0, 1) \\ (1, 0, 1, 2) \\ (1, 1, 0, 2) \\ (1, 1, 1, 3) \end{Bmatrix} \quad (\text{A.3})$$

The first step is to find the matching blocks and then contract the underlying tensors (indicated by the star). At the end, new blocks occur, that fulfill the condition

$$N_{l-1} + N(\sigma_l) + N(\sigma_{l+1}) = N_{l+1}. \quad (\text{A.4})$$

The scheme also applies to contractions over more than one axis, which scales better than doing one after another. In this case, one simply has to look for all blocks that match the corresponding axes.

## Reshaping

Another important tensor operation is reshaping a tensor with four indices into a matrix with only two in order to be able to perform an SVD

$$\Phi_{a_{l-1}, a_{l+1}}^{\sigma_l, \sigma_{l+1}} \rightarrow \Phi_{(a_{l-1}\sigma_l), (\sigma_{l+1}a_{l+1})}. \quad (\text{A.5})$$

As discussed in Section 3.5,  $\Phi$  has block structure with blocks labeled by  $N_l = N(a_{l-1}) + N(\sigma_l)$ . Then  $(N_{l-1}, N(\sigma_l))$  are the block row indices and  $(N(\sigma_{l+1}), N_{l+1})$  correspond to the indices of the block columns. As an example, we look at Eq. (A.3) where we have  $N_l = 0, 1, 2$ . The corresponding blocks are (in order  $(N(\sigma_l), N_{l-1}, N(\sigma_{l+1}), N_{l+1})$ ):

$$\begin{aligned} N_l = 0: & \quad (0, 0, 0, 0), (0, 0, 1, 1) \\ N_l = 1: & \quad (0, 1, 0, 1), (0, 1, 1, 2), (1, 0, 0, 1), (1, 0, 1, 2) \\ N_l = 2: & \quad (1, 1, 0, 2), (1, 1, 1, 3). \end{aligned} \quad (\text{A.6})$$

Let us focus on  $N_l = 2$ , where we have the row indices  $(0, 1)$  and  $(1, 0)$  and the column indices  $(0, 1)$  and  $(1, 2)$ . Thus the reshaped matrix has the following form

$$\Phi^{N_l=2} = \begin{matrix} & \begin{matrix} (0, 1) & (1, 2) \end{matrix} \\ \begin{matrix} (0, 1) \\ (1, 0) \end{matrix} & \begin{pmatrix} M_{(0,1),(0,1)} & M_{(0,1),(1,2)} \\ M_{(1,0),(0,1)} & M_{(1,0),(1,2)} \end{pmatrix} \end{matrix} \quad (\text{A.7})$$

If some block  $(N(\sigma_l), N_{l-1}, N(\sigma_{l+1}), N_{l+1})$  does not exist yet, it will be simply set to zero but has to be kept. In this way, new blocks can be created during the time evolution. The ordering of row and column labels is not changed during the SVD such that reshaping the matrices  $U_{(a_{l-1}\sigma_l), a_l}$  and  $(V^\dagger)_{a_l, (\sigma_{l+1}a_{l+1})}$  back into tensors  $U_{a_{l-1}, a_l}^{\sigma_l}$  and  $(V^\dagger)_{a_l, a_{l+1}}^{\sigma_{l+1}}$  respectively, can be done as all quantum number labels are known. However, one needs the dimension of the corresponding blocks that have to be stored in the first reshaping process.

Of course, the corresponding tensor for each label  $(N(\sigma_l), N_{l-1}, N(\sigma_{l+1}), N_{l+1})$  has to be reshaped properly as well.

## B. BFRM and FFLO

### Molecule momentum distribution function after time-of-flight

In this section, we want to give a detailed derivation of Eq. (1.29) for the momentum distribution function of the molecules after some time-of-flight. We start with an initial molecular wave function  $M_0(\mathbf{r})$  that describes the condensate. After some time  $t$  of free evolution (governed by the free Schrödinger equation), we arrive at

$$m(\mathbf{r}, t) = \int \frac{d^3k}{(2\pi)^3} \tilde{M}_0(\mathbf{k}) e^{i\mathbf{k}\cdot\mathbf{r}} e^{-i\frac{\hbar t}{2m}k^2}, \quad (\text{B.1})$$

with the Fourier transform  $M_0(\mathbf{k})$  of the initial wave function given by

$$\tilde{M}_0(\mathbf{k}) = \int d^3r M_0(\mathbf{r}) e^{-i\mathbf{k}\cdot\mathbf{r}}. \quad (\text{B.2})$$

The density distribution of the molecules is given by

$$n(\mathbf{r}, t) = \langle \hat{m}^\dagger(\mathbf{r}, t) \hat{m}(\mathbf{r}, t) \rangle \approx m^*(\mathbf{r}, t) m(\mathbf{r}, t). \quad (\text{B.3})$$

We now shift  $\mathbf{k} \rightarrow \mathbf{k} + \frac{m\mathbf{r}}{\hbar t}$  in Eq. (B.1) and Eq. (B.2), leading to

$$\begin{aligned} m(\mathbf{r}, t) &= \int \frac{d^3k}{(2\pi)^3} M_0\left(\mathbf{k} + \frac{m\mathbf{r}}{\hbar t}\right) e^{i(\mathbf{k} + \frac{m\mathbf{r}}{\hbar t})\cdot\mathbf{r}} e^{-i\frac{\hbar t}{2m}(\mathbf{k} + \frac{m\mathbf{r}}{\hbar t})^2} \\ &= \int \frac{d^3k}{(2\pi)^3} M_0\left(\mathbf{k} + \frac{m\mathbf{r}}{\hbar t}\right) e^{-i\frac{m\mathbf{r}^2}{2\hbar t}} e^{-i\frac{\hbar t}{2m}k^2} \end{aligned} \quad (\text{B.4})$$

and

$$M_0\left(\mathbf{k} + \frac{m\mathbf{r}}{\hbar t}\right) = \int d^3r' M_0(\mathbf{r}') e^{-i\mathbf{k}\cdot\mathbf{r}'} e^{-i\frac{m}{\hbar t}\mathbf{r}\cdot\mathbf{r}'} \equiv \tilde{M}_0(\mathbf{k}). \quad (\text{B.5})$$

Plugging these results into Eq. (B.3) yields

$$\begin{aligned}
 m^*(\mathbf{r}, t)m(\mathbf{r}, t) &= \int \frac{d^3k}{(2\pi)^3} \int \frac{d^3k'}{(2\pi)^3} \tilde{M}_0^*(\mathbf{k})\tilde{M}_0(\mathbf{k}')e^{i\frac{\hbar t}{2m}(k^2-k'^2)} \\
 &= \int d^3r' \int d^3r'' M_0^*(\mathbf{r}')M_0(\mathbf{r}'')e^{i\frac{m}{\hbar t}\mathbf{r}(\mathbf{r}'-\mathbf{r}'')} \\
 &\quad \times \underbrace{\int \frac{d^3k}{(2\pi)^3} \int \frac{d^3k'}{(2\pi)^3} e^{i(\mathbf{k}\mathbf{r}'-\mathbf{k}'\mathbf{r}'')} e^{i\frac{\hbar t}{2m}(k^2-k'^2)}}_{F(\mathbf{r}', \mathbf{r}'')}. \tag{B.6}
 \end{aligned}$$

The function  $F(\mathbf{r}', \mathbf{r}'')$  can be calculated by introducing new variables  $\mathbf{q}$  and  $\mathbf{p}$  such that  $\mathbf{k} = (\mathbf{q} + \mathbf{p})/2$  and  $\mathbf{k}' = (\mathbf{q} - \mathbf{p})/2$ . Then we end up with

$$\begin{aligned}
 F(\mathbf{r}', \mathbf{r}'') &= \int \frac{d^3q}{(2\pi)^3} \int \frac{d^3p}{(2\pi)^3} e^{i\frac{\hbar t}{m}\mathbf{p}\mathbf{q}} e^{i\mathbf{p}(\mathbf{r}'+\mathbf{r}'')/2} e^{i\mathbf{q}(\mathbf{r}'-\mathbf{r}'')} \\
 &= \left(\frac{m}{2\hbar\pi t}\right)^3 e^{im(\mathbf{r}'+\mathbf{r}'')(\mathbf{r}'-\mathbf{r}'')/(2\hbar t)}. \tag{B.7}
 \end{aligned}$$

The final (exact) expression for the molecular density distribution then reads

$$n(\mathbf{r}, t) = \int d^3r' \int d^3r'' M_0^*(\mathbf{r}')M_0(\mathbf{r}'')e^{i\frac{m}{\hbar t}\mathbf{r}(\mathbf{r}'-\mathbf{r}'')} \left(\frac{m}{2\hbar\pi t}\right)^3 e^{im(\mathbf{r}'+\mathbf{r}'')(\mathbf{r}'-\mathbf{r}'')/(2\hbar t)}. \tag{B.8}$$

After a long time-of-flight, the cloud is much larger than its initial configuration and we neglect the second exponential since  $\mathbf{r}'$  and  $\mathbf{r}''$  are restricted to the initial cloud size and are small compared to  $\mathbf{r}$ . The expression then simplifies and becomes

$$\begin{aligned}
 n(\mathbf{r}, t) &= \int d^3r' \int d^3r'' M_0^*(\mathbf{r}')M_0(\mathbf{r}'')e^{i\frac{m}{\hbar t}\mathbf{r}(\mathbf{r}'-\mathbf{r}'')} \left(\frac{m}{2\hbar\pi t}\right)^3 \\
 &= \left(\frac{m}{2\hbar\pi t}\right)^3 \tilde{M}_0^*\left(\frac{m\mathbf{r}}{\hbar t}\right) \tilde{M}_0\left(\frac{m\mathbf{r}}{\hbar t}\right) = \left(\frac{m}{2\hbar\pi t}\right)^3 \tilde{n}\left(\mathbf{k} = \frac{m\mathbf{r}}{\hbar t}\right). \tag{B.9}
 \end{aligned}$$

Thus, the time-of-flight measurement of the density distribution in fact measures the initial momentum distribution of the cloud.

**Release from a quasi-1D tube** After having derived the general form of the density distribution after time-of-flight, we want to turn to the special case where the gas is initially trapped in a quasi-1D tube. This can be created by an optical lattice, where the confinement in two directions (e.g.  $y$  and  $z$ ) is much larger than in the third one ( $x$ ). We further assume

---

that our condensate is in a FFLO state with non-zero center-of-mass momentum of the molecules such that the initial wave function is given by<sup>1</sup>

$$M_0(\mathbf{r}) = M_q(\mathbf{r})e^{iqx}, \quad (\text{B.10})$$

with

$$M_q(\mathbf{r}) \propto e^{-(y^2+z^2)/(2r_0^2)} e^{-x^2/(2a_0^2)}. \quad (\text{B.11})$$

Here,  $r_0$  is the radial confinement and  $a_0$  is the axial confinement with the condition that  $r_0 \ll a_0$ .

Fourier transformation of Eq. (B.10) yields

$$\tilde{M}_0(\mathbf{k}) \propto e^{-a_0^2(q-k_x)^2/2} e^{-r_0^2(k_y^2+k_z^2)/2}. \quad (\text{B.12})$$

Finally, we arrive at

$$n(\mathbf{r}, t) \propto \left( \frac{m}{2\pi\hbar t} \right)^3 e^{-a_0^2(q-\frac{mx}{\hbar t})^2} e^{-r_0^2(y^2+z^2)(\frac{m}{\hbar t})^2}. \quad (\text{B.13})$$

We see, that the density distribution is peaked around

$$x = \frac{q\hbar t}{m} \quad (\text{B.14})$$

with a width  $\Delta x = \hbar t/(\sqrt{2}a_0 m)$ . Obviously, the peak can only be resolved under the condition  $x/\Delta x \gg 1$  such that for experimental observation, the following condition has to hold

$$q a_0 \gg 1. \quad (\text{B.15})$$

This means, that on the one hand, polarization has to be large enough and on the other hand that the confinement along the axial direction has to be weak.

---

<sup>1</sup>Generalization to a superposition of different momenta is straightforward.



## C. Error control

In this appendix, we present selected plots for the truncation error in our simulations. For  $L = 24$ , we restricted the number of kept states to  $D = 1024$  at most. Concerning the truncation error, we see that in some cases (see the error of the visibility in Fig. C.1), the observable has not completely converged with respect to the number of states. However, we do not see any qualitative or striking quantitative difference in our results. In addition, we have chosen the upper limit in such a way that we still get reasonable computation times.

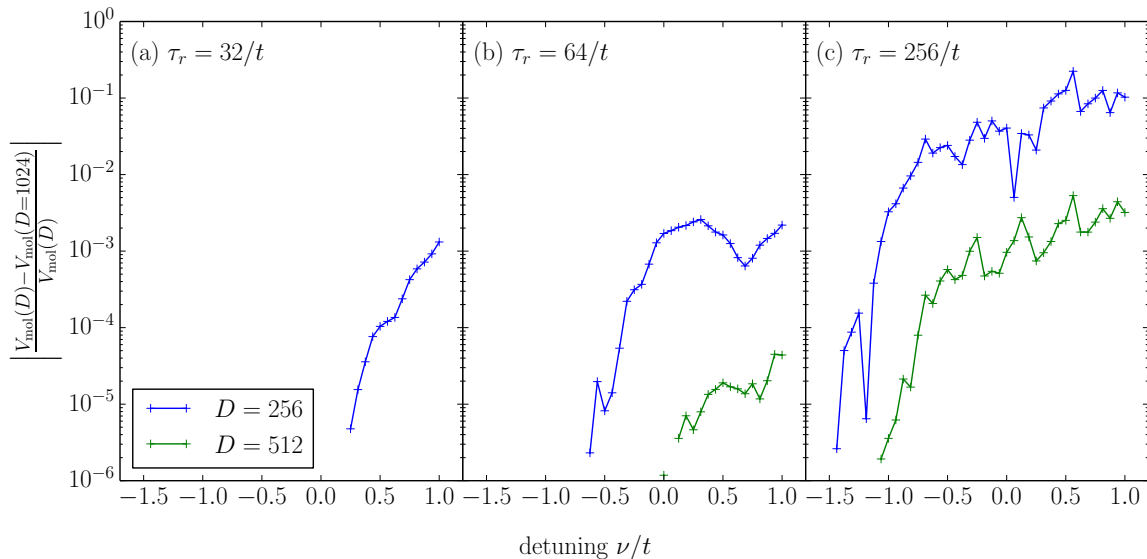


**Figure C.1.:** Truncation error of the visibility  $V_{\text{mol}}$  for  $\mathbf{p} = \mathbf{3}/4$  and different ramp times. ( $g = t/2$ ,  $L = 24$ ,  $n = 2/3$ ,  $\varepsilon = 10^{-8}$ ). At points, where no data is shown, the error was below the precision of the data, set to  $10^{-10}$ .

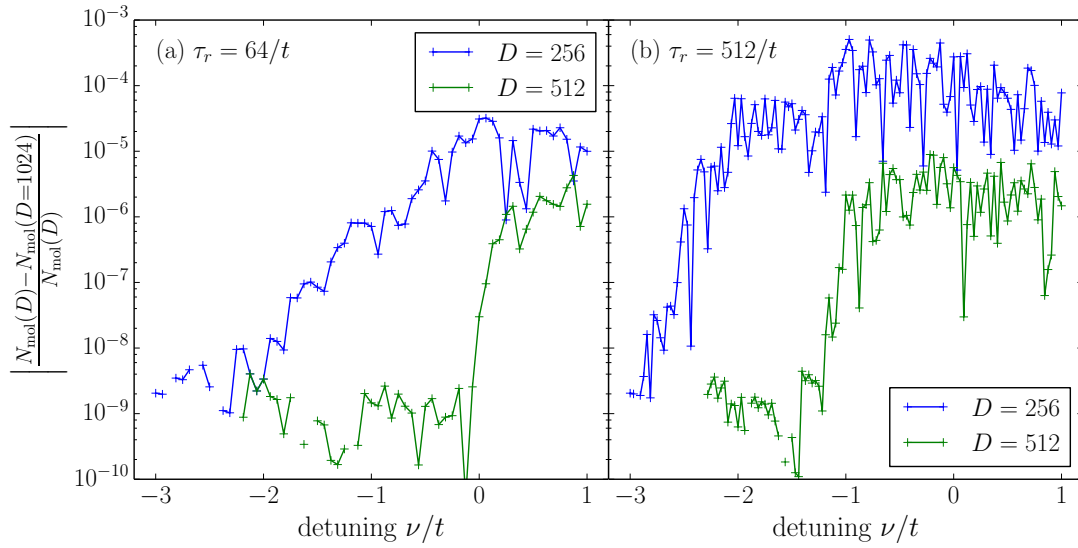


**Figure C.2.:** Truncation error of the number of molecules  $N_{\text{mol}}$  during the ramp for  $\mathbf{p} = \mathbf{3}/4$  and different ramp times (a)  $\tau_r = 64/t$  and (b)  $\tau_r = 512/t$ . ( $g = t/2$ ,  $L = 24$ ,  $n = 2/3$ ,  $\varepsilon = 10^{-8}$ ). At points, where no data is shown, the error was below the precision of the data, set to  $10^{-10}$ .

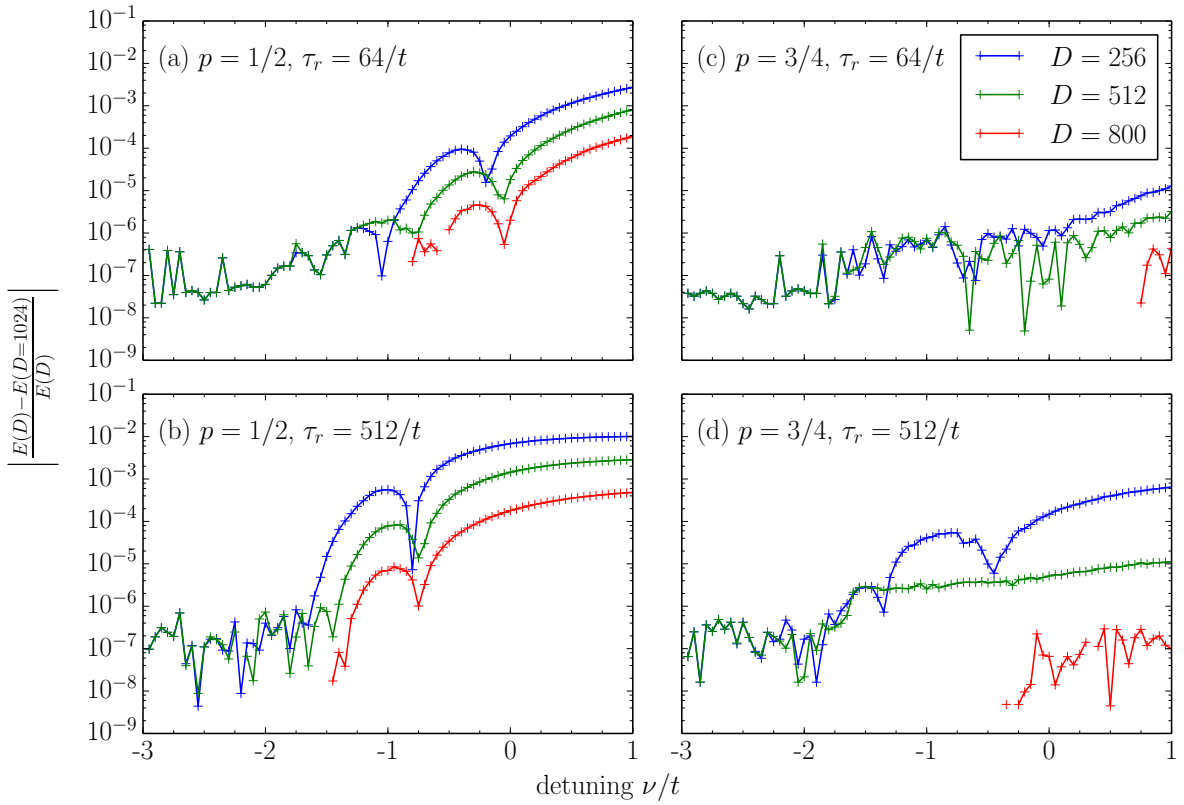


**Figure C.3.:** Truncation error of the Energy  $E$  during the ramp for  $\mathbf{p} = \mathbf{1/2}$  ((a) and (b)) and  $\mathbf{p} = \mathbf{3/4}$  ((c) and (d)). ( $g = t/2$ ,  $L = 24$ ,  $n = 2/3$ ,  $\varepsilon = 10^{-8}$ ). At points, where no data is shown, the error was below the precision of the data, set to  $10^{-10}$ .



## D. Additional figures

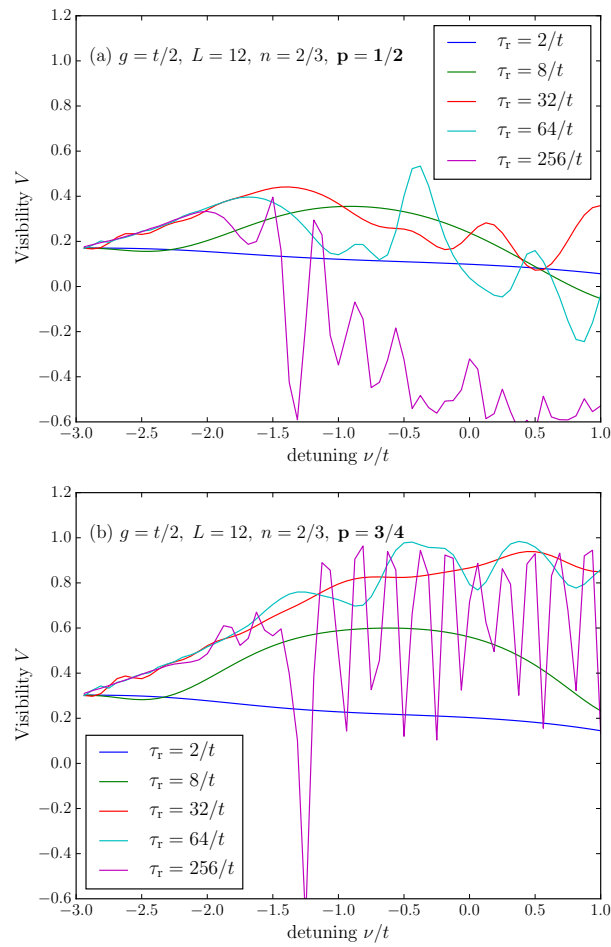


**Figure D.1.:** (a) Visibility  $V_{\text{mol}}$  during ramp for  $\mathbf{p} = 1/2$  and different ramp times  $\tau_r$ . (b) Visibility  $V_{\text{mol}}$  during ramp for  $\mathbf{p} = 3/4$  and different ramp times  $\tau_r$ . (TEBD:  $D = 512$ ,  $\varepsilon = 10^{-8}$ ,  $n_{\text{steps}} = 2560$ )

D. Additional figures

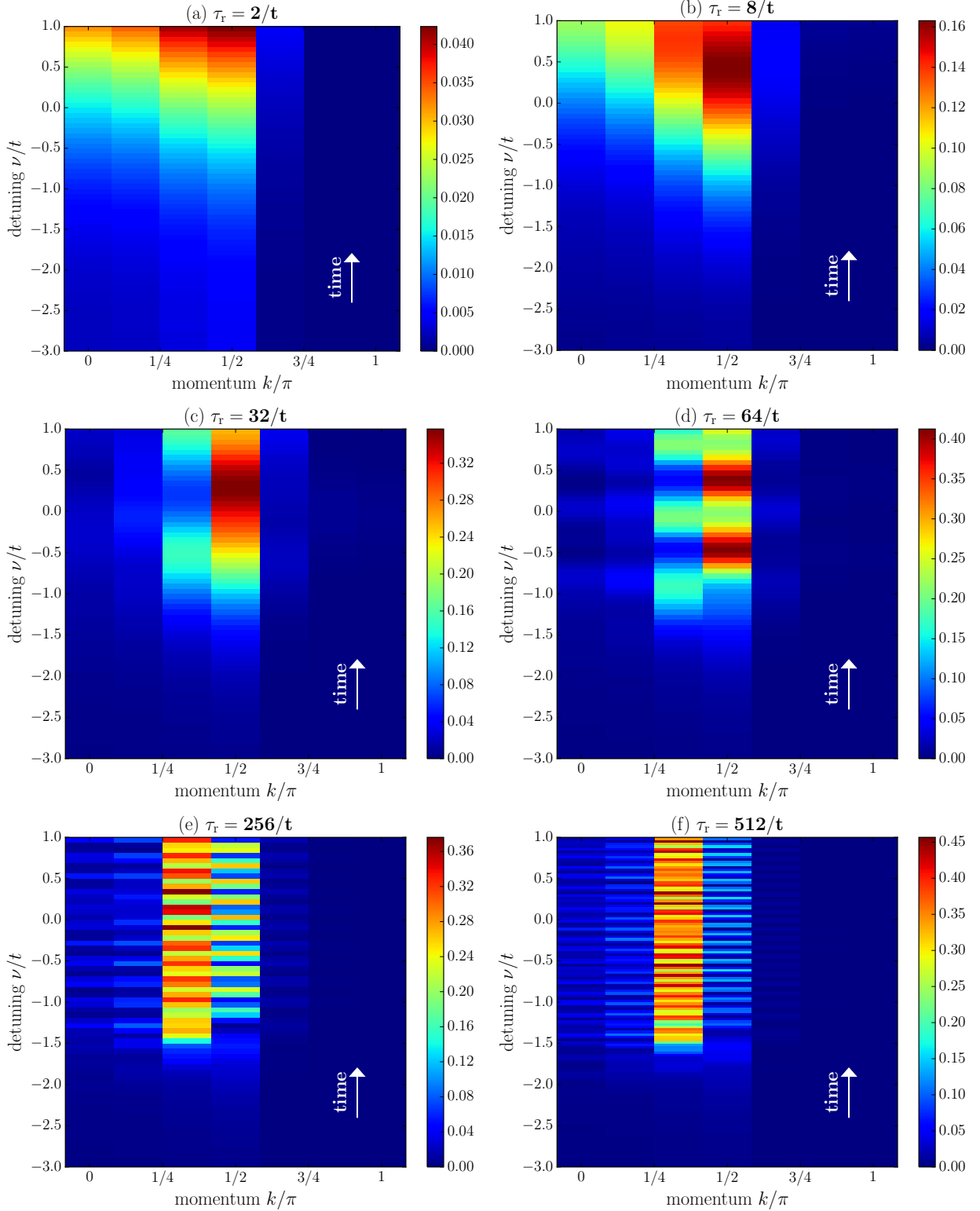


**Figure D.2.:**  $n_k^{\text{mol}}$  during the ramp for  $\mathbf{p} = 3/4$  and different ramp times  $\tau_r$ . The white arrow indicates the direction of time. FFLO momentum is at  $k = q = \pi/2$ . (TEBD:  $g = t/2$ ,  $L = 12$ ,  $n = 2/3$ ,  $D = 512$ ,  $\varepsilon = 10^{-8}$ ,  $n_{\text{steps}} = 2560$  ( $\tau_r \leq 256/t$ ) and  $n_{\text{steps}} = 512$  ( $\tau_r = 512/t$ ))

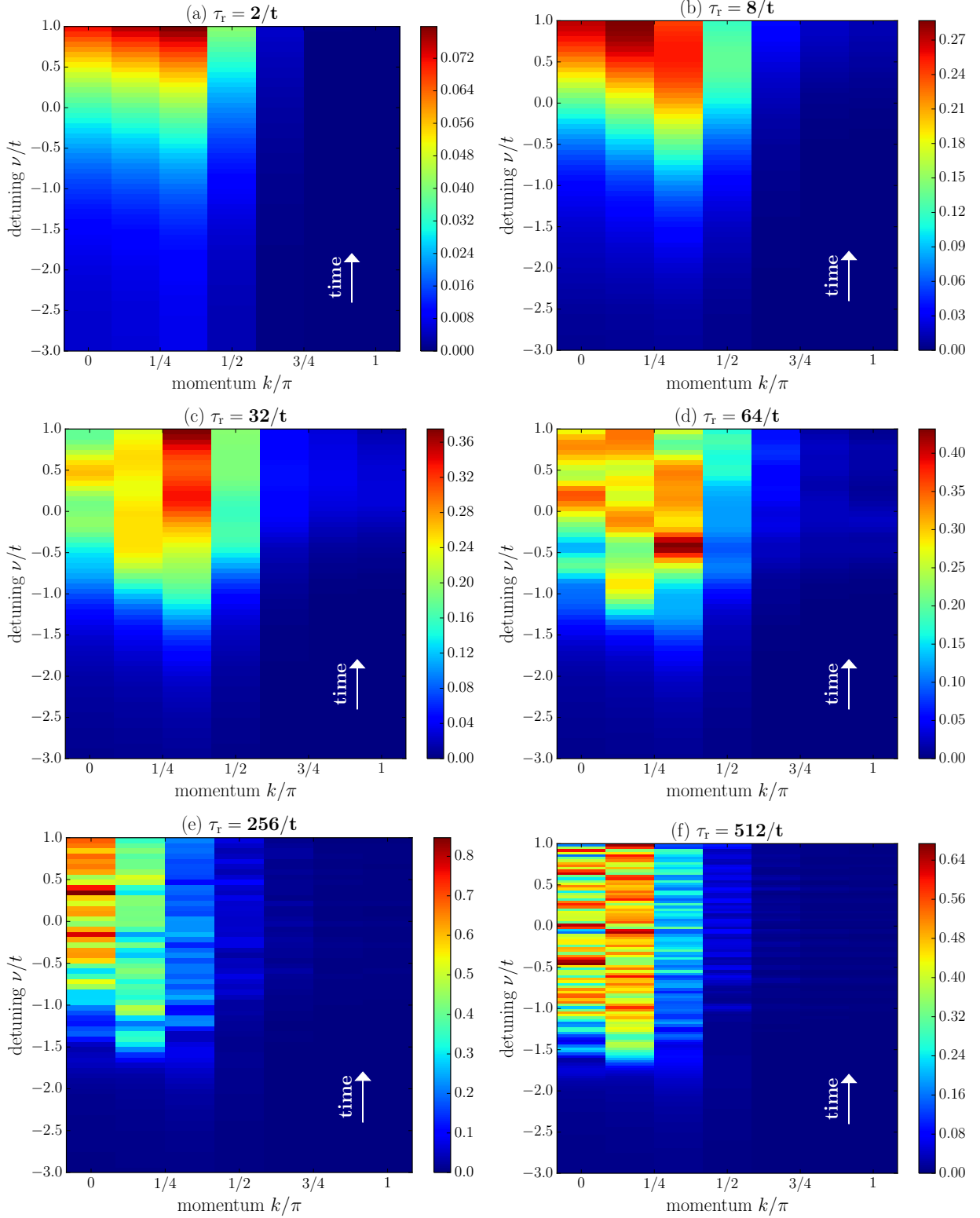


**Figure D.3.:**  $n_k^{\text{mol}}$  during the ramp for  $\mathbf{p} = 1/2$  and different ramp times  $\tau_r$ . The white arrow indicates the direction of time. FFLO momentum is at  $k = q = \pi/3$ . (TEBD:  $g = t/2$ ,  $L = 12$ ,  $n = 2/3$ ,  $D = 512$ ,  $\varepsilon = 10^{-8}$ ,  $n_{\text{steps}} = 2560$  ( $\tau_r \leq 256/t$ ) and  $n_{\text{steps}} = 512$  ( $\tau_r = 512/t$ ))



# Bibliography

- [1] P. Fulde and R. A. Ferrell. Superconductivity in a Strong Spin-Exchange Field. *Physical Review* **135**, A550–A563 (1964).
- [2] A. I. Larkin and Y. N. Ovchinnikov. Inhomogeneous state of superconductors. *Sov. Phys. JETP* **20**, 762 (1965).
- [3] J. Bardeen, L. N. Cooper, and J. R. Schrieffer. Theory of Superconductivity. *Physical Review* **108**, 1175 (1957).
- [4] A. E. Feiguin, F. Heidrich-Meisner, G. Orso, and W. Zwerger. BCS–BEC Crossover and Unconventional Superfluid Order in One Dimension. In W. Zwerger (ed.), *The BCS-BEC Crossover and the Unitary Fermi Gas, Lecture notes in physics*, volume 836, pp. 503–532 (Springer, Berlin) (2012).
- [5] X.-W. Guan, M. T. Batchelor, and C. Lee. Fermi gases in one dimension: From Bethe ansatz to experiments. *Reviews of Modern Physics* **85**, 1633–1691 (2013).
- [6] R. Lortz, Y. Wang, A. Demuer, P. H. M. Böttger, B. Bergk, G. Zwicknagl, Y. Nakazawa, and J. Wosnitza. Calorimetric Evidence for a Fulde-Ferrell-Larkin-Ovchinnikov Superconducting State in the Layered Organic Superconductor  $\kappa$ -(BEDT-TTF)<sub>2</sub>Cu(NCS)<sub>2</sub>. *Physical Review Letters* **99**, 187002 (2007).
- [7] A. M. Clogston. Upper Limit for the Critical Field in Hard Superconductors. *Physical Review Letters* **9**, 266–267 (1962).
- [8] L. G. Aslamazov. Influence of impurities on the existence of an inhomogeneous state in a ferromagnetic superconductor. *Sov. Phys. JETP* **28** (1969).
- [9] D. F. Agterberg and K. Yang. The effect of impurities on Fulde-Ferrell-Larkin-Ovchinnikov superconductors. *Journal of Physics: Condensed Matter* **13**, 9259–9270 (2001).

- [10] I. Bloch, J. Dalibard, and W. Zwerger. Many-body physics with ultracold gases. *Reviews of Modern Physics* **80**, 885 (2008).
- [11] S. Giorgini, L. P. Pitaevskii, and S. Stringari. Theory of ultracold atomic Fermi gases. *Reviews of Modern Physics* **80**, 1215–1274 (2008).
- [12] W. Ketterle and M. W. Zwierlein. Making, probing and understanding ultracold Fermi gases. In M. Inguscio, W. Ketterle, and C. Salomon (eds.), *Ultracold Fermi Gases, Proceedings of the International School of Physics “Enrico Fermi”, Course CLXIV, Varenna, 20-30 June 2006* (IOS Press, Amsterdam) (2008).
- [13] H. Feshbach. Unified theory of nuclear reactions. *Annals of Physics* **5**, 357–390 (1958).
- [14] C. Chin, R. Grimm, P. Julienne, and E. Tiesinga. Feshbach resonances in ultracold gases. *Reviews of Modern Physics* **82**, 1225–1286 (2010).
- [15] V. A. Yurovsky, M. Olshanii, and D. S. Weiss. Collisions, correlations, and integrability in atom waveguides. In *Advances In Atomic, Molecular, and Optical Physics*, volume 55. pp. 61–138 (Elsevier) (2008).
- [16] M. A. Cazalilla, R. Citro, T. Giamarchi, E. Orignac, and M. Rigol. One dimensional bosons: From condensed matter systems to ultracold gases. *Reviews of Modern Physics* **83**, 1405–1466 (2011).
- [17] M. Gaudin. Un système à une dimension de fermions en interaction. *Physics Letters A* **24**, 55–56 (1967).
- [18] C. N. Yang. Some Exact Results for the Many-Body Problem in one Dimension with Repulsive Delta-Function Interaction. *Physical Review Letters* **19**, 1312–1315 (1967).
- [19] J. N. Fuchs, A. Recati, and W. Zwerger. Exactly Solvable Model of the BCS-BEC Crossover. *Physical Review Letters* **93**, 090408 (2004).
- [20] I. V. Tokatly. Dilute Fermi Gas in Quasi-One-Dimensional Traps: From Weakly Interacting Fermions via Hard Core Bosons to a Weakly Interacting Bose Gas. *Physical Review Letters* **93**, 090405 (2004).
- [21] H. Hu, X.-J. Liu, and P. D. Drummond. Phase Diagram of a Strongly Interacting Polarized Fermi Gas in One Dimension. *Physical Review Letters* **98**, 070403 (2007).

- 
- [22] G. Orso. Attractive Fermi Gases with Unequal Spin Populations in Highly Elongated Traps. *Physical Review Letters* **98**, 070402 (2007).
- [23] K. Yang. Inhomogeneous superconducting state in quasi-one-dimensional systems. *Physical Review B* **63**, 140511 (2001).
- [24] A. E. Feiguin and F. Heidrich-Meisner. Pairing states of a polarized Fermi gas trapped in a one-dimensional optical lattice. *Physical Review B* **76**, 220508 (2007).
- [25] A. Lüscher, R. M. Noack, and A. M. Läuchli. Fulde-Ferrell-Larkin-Ovchinnikov state in the one-dimensional attractive Hubbard model and its fingerprint in spatial noise correlations. *Physical Review A* **78**, 013637 (2008).
- [26] M. Rizzi, M. Polini, M. A. Cazalilla, M. R. Bakhtiari, M. P. Tosi, and R. Fazio. Fulde-Ferrell-Larkin-Ovchinnikov pairing in one-dimensional optical lattices. *Physical Review B* **77**, 245105 (2008).
- [27] M. Tezuka and M. Ueda. Density-Matrix Renormalization Group Study of Trapped Imbalanced Fermi Condensates. *Physical Review Letters* **100**, 110403 (2008).
- [28] G. G. Batrouni, M. H. Huntley, V. G. Rousseau, and R. T. Scalettar. Exact Numerical Study of Pair Formation with Imbalanced Fermion Populations. *Physical Review Letters* **100**, 116405 (2008).
- [29] S. K. Baur, J. Shumway, and E. J. Mueller. Fulde-Ferrell-Larkin-Ovchinnikov versus Bose-Fermi mixture in a polarized one-dimensional Fermi gas at a Feshbach resonance: A three-body study. *Physical Review A* **81**, 033628 (2010).
- [30] X.-J. Liu, H. Hu, and P. D. Drummond. Fulde-Ferrell-Larkin-Ovchinnikov states in one-dimensional spin-polarized ultracold atomic Fermi gases. *Physical Review A* **76**, 043605 (2007).
- [31] M. M. Parish, S. K. Baur, E. J. Mueller, and D. A. Huse. Quasi-One-Dimensional Polarized Fermi Superfluids. *Physical Review Letters* **99**, 250403 (2007).
- [32] H. Moritz, T. Stöferle, K. Günter, M. Köhl, and T. Esslinger. Confinement Induced Molecules in a 1D Fermi Gas. *Physical Review Letters* **94**, 210401 (2005).
- [33] M. Olshanii. Atomic Scattering in the Presence of an External Confinement and a Gas of Impenetrable Bosons. *Physical Review Letters* **81**, 938 (1998).

- [34] T. Bergeman, M. G. Moore, and M. Olshanii. Atom-Atom Scattering under Cylindrical Harmonic Confinement: Numerical and Analytic Studies of the Confinement Induced Resonance. *Physical Review Letters* **91**, 163201 (2003).
- [35] Y.-A. Liao, Rittner, Ann Sophie C, T. Paprotta, W. Li, G. B. Partridge, R. G. Hulet, S. K. Baur, and E. J. Mueller. Spin-imbalance in a one-dimensional Fermi gas. *Nature* **467**, 567–569 (2010).
- [36] K. Yang. Realization and Detection of Fulde-Ferrell-Larkin-Ovchinnikov Superfluid Phases in Trapped Atomic Fermion Systems. *Physical Review Letters* **95**, 218903 (2005).
- [37] T. Paananen, T. K. Koponen, P. Törmä, and J.-P. Martikainen. Noise correlations of the ultracold Fermi gas in an optical lattice. *Physical Review A* **77**, 053602 (2008).
- [38] M. R. Bakhtiari, M. J. Leskinen, and P. Törmä. Spectral Signatures of the Fulde-Ferrell-Larkin-Ovchinnikov Order Parameter in One-Dimensional Optical Lattices. *Physical Review Letters* **101**, 120404 (2008).
- [39] M. Holland, S. Kokkelmans, M. L. Chiofalo, and R. Walser. Resonance Superfluidity in a Quantum Degenerate Fermi Gas. *Physical Review Letters* **87**, 120406 (2001).
- [40] E. Timmermans, K. Furuya, P. W. Milonni, and A. K. Kerman. Prospect of creating a composite Fermi–Bose superfluid. *Physics Letters A* **285**, 228–233 (2001).
- [41] A. Recati, J. Fuchs, and W. Zwerger. Boson-fermion resonance model in one dimension. *Physical Review A* **71**, 033630 (2005).
- [42] R. Citro and E. Orignac. Atom-Molecule Coherence in a One-Dimensional System. *Physical Review Letters* **95**, 130402 (2005).
- [43] E. Orignac and R. Citro. Phase transitions in the boson-fermion resonance model in one dimension. *Physical Review A* **73**, 063611 (2006).
- [44] F. Heidrich-Meisner, A. E. Feiguin, U. Schollwöck, and W. Zwerger. BCS-BEC crossover and the disappearance of Fulde-Ferrell-Larkin-Ovchinnikov correlations in a spin-imbalance one-dimensional Fermi gas. *Physical Review A* **81**, 023629 (2010).

- 
- [45] L. Riegger. *Non-equilibrium dynamics of one-dimensional spin-polarized Fermi gases with attractive interactions*. Master thesis, Ludwig-Maximilians-Universität, München (2014).
- [46] L. Riegger, G. Orso, and F. Heidrich-Meisner. Interaction quantum quenches in the one-dimensional Fermi-Hubbard model with spin imbalance. *Physical Review A* **91**, 043623 (2015).
- [47] G. Vidal. Efficient Classical Simulation of Slightly Entangled Quantum Computations. *Physical Review Letters* **91**, 147902 (2003).
- [48] G. Vidal. Efficient Simulation of One-Dimensional Quantum Many-Body Systems. *Physical Review Letters* **93**, 040502 (2004).
- [49] T. Kibble. Topology of cosmic domains and strings. *Journal of Physics A: Mathematical and General* **9**, 1387–1398 (1976).
- [50] W. Zurek. Cosmological experiments in superfluid helium? *Nature* **317**, 505–508 (1985).
- [51] W. Zurek, U. Dorner, and P. Zoller. Dynamics of a Quantum Phase Transition. *Physical Review Letters* **95**, 105701 (2005).
- [52] M. Alford, J. A. Bowers, and K. Rajagopal. Crystalline color superconductivity. *Physical Review D* **63**, 074016 (2001).
- [53] J. A. Bowers and K. Rajagopal. Crystallography of color superconductivity. *Physical Review D* **66**, 065002 (2002).
- [54] K. Machida and H. Nakanishi. Superconductivity under a ferromagnetic molecular field. *Physical Review B* **30**, 122–133 (1984).
- [55] M. Randeria, J.-M. Duan, and L.-Y. Shieh. Bound states, Cooper pairing, and Bose condensation in two dimensions. *Physical Review Letters* **62**, 981 (1989).
- [56] M. Girardeau. Relationship between Systems of Impenetrable Bosons and Fermions in One Dimension. *Journal of Mathematical Physics* **1**, 516 (1960).
- [57] C. Mora, A. Komnik, R. Egger, and A. O. Gogolin. Four-Body Problem and BEC-BCS Crossover in a Quasi-One-Dimensional Cold Fermion Gas. *Physical Review Letters* **95**, 080403 (2005).

- [58] A. Luther and V. J. Emery. Backward Scattering in the One-Dimensional Electron Gas. *Physical Review Letters* **33**, 589 (1974).
- [59] E. H. Lieb and W. Liniger. Exact Analysis of an Interacting Bose Gas. *Physical Review* **130**, 1605–1624 (1963).
- [60] P. Kakashvili and C. J. Bolech. Paired states in spin-imbalanced atomic Fermi gases in one dimension. *Physical Review A* **79**, 041603 (2009).
- [61] E. Zhao, X.-W. Guan, W. V. Liu, M. T. Batchelor, and M. Oshikawa. Analytic Thermodynamics and Thermometry of Gaudin-Yang Fermi Gases. *Physical Review Letters* **103**, 140404 (2009).
- [62] C. J. Bolech, F. Heidrich-Meisner, S. Langer, I. P. McCulloch, G. Orso, and M. Rigol. Long-Time Behavior of the Momentum Distribution During the Sudden Expansion of a Spin-Imbalanced Fermi Gas in One Dimension. *Physical Review Letters* **109**, 110602 (2012).
- [63] H. Lu, L. O. Baksmaty, C. J. Bolech, and H. Pu. Expansion of 1D Polarized Superfluids: The Fulde-Ferrell-Larkin-Ovchinnikov State Reveals Itself. *Physical Review Letters* **108**, 225302 (2012).
- [64] J. Kajala, F. Massel, and P. Törmä. Expansion Dynamics in the One-Dimensional Fermi-Hubbard Model. *Physical Review Letters* **106**, 206401 (2011).
- [65] A. Polkovnikov, K. Sengupta, A. Silva, and M. Vengalattore. Colloquium: Nonequilibrium dynamics of closed interacting quantum systems. *Reviews of Modern Physics* **83**, 863–883 (2011).
- [66] J. Eisert, M. Friesdorf, and C. Gogolin. Quantum many-body systems out of equilibrium. *Nature Physics* **11**, 124–130 (2015).
- [67] T. Langen, R. Geiger, and J. Schmiedmayer. Ultracold Atoms Out of Equilibrium. *Annual Review of Condensed Matter Physics* **6**, 201–217 (2015).
- [68] T. Kibble. Some implications of a cosmological phase transition. *Physics Reports* **67**, 183–199 (1980).
- [69] W. Zurek. Cosmic strings in laboratory superfluids and the topological remnants of other phase transitions. *Acta Physica Polonica B* **24**, 1301–1311 (1993).

- 
- [70] W. Zurek. Cosmological experiments in condensed matter systems. *Physics Reports* **276**, 177–221 (1996).
- [71] S. Sachdev. *Quantum phase transitions* (Cambridge University Press, Cambridge and New York), 2nd edition (2011).
- [72] B. Damski. The Simplest Quantum Model Supporting the Kibble-Zurek Mechanism of Topological Defect Production: Landau-Zener Transitions from a New Perspective. *Physical Review Letters* **95**, 035701 (2005).
- [73] B. Damski and W. Zurek. Adiabatic-impulse approximation for avoided level crossings: From phase-transition dynamics to Landau-Zener evolutions and back again. *Physical Review A* **73**, 063405 (2006).
- [74] L. D. Landau. Zur Theorie der Energieübertragung. II. *Physikalische Zeitschrift der Sowjetunion* **2**, 46–51 (1932).
- [75] C. Zener. Non-Adiabatic Crossing of Energy Levels. *Proceedings of the Royal Society A: Mathematical, Physical and Engineering Sciences* **137**, 696–702 (1932).
- [76] L. E. Sadler, J. M. Higbie, S. R. Leslie, M. Vengalattore, and D. M. Stamper-Kurn. Spontaneous symmetry breaking in a quenched ferromagnetic spinor Bose-Einstein condensate. *Nature* **443**, 312–315 (2006).
- [77] C. N. Weiler, T. W. Neely, D. R. Scherer, A. S. Bradley, M. J. Davis, and B. P. Anderson. Spontaneous vortices in the formation of Bose–Einstein condensates. *Nature* **455**, 948–951 (2008).
- [78] D. Chen, M. White, C. Borries, and B. DeMarco. Quantum Quench of an Atomic Mott Insulator. *Physical Review Letters* **106**, 235304 (2011).
- [79] G. Lamporesi, S. Donadello, S. Serafini, F. Dalfovo, and G. Ferrari. Spontaneous creation of Kibble–Zurek solitons in a Bose–Einstein condensate. *Nature Physics* **9**, 656–660 (2013).
- [80] L. Corman, L. Chomaz, T. Bienaimé, R. Desbuquois, C. Weitenberg, S. Nascimbène, J. Dalibard, and J. Beugnon. Quench-Induced Supercurrents in an Annular Bose Gas. *Physical Review Letters* **113**, 135302 (2014).

- [81] L. Chomaz, L. Corman, T. Bienaimé, R. Desbuquois, C. Weitenberg, S. Nascimbène, J. Beugnon, and J. Dalibard. Emergence of coherence via transverse condensation in a uniform quasi-two-dimensional Bose gas. *Nature communications* **6**, 6162 (2015).
- [82] N. Navon, A. L. Gaunt, R. P. Smith, and Z. Hadzibabic. Quantum gases. Critical dynamics of spontaneous symmetry breaking in a homogeneous Bose gas. *Science* **347**, 167–170 (2015).
- [83] S. Braun, M. Friesdorf, S. S. Hodgman, M. Schreiber, J. P. Ronzheimer, A. Riera, M. Del Rey, I. Bloch, J. Eisert, and U. Schneider. Emergence of coherence and the dynamics of quantum phase transitions. *Proceedings of the National Academy of Sciences of the United States of America* **112**, 3641–3646 (2015).
- [84] A. del Campo and W. H. Zurek. Universality of phase transition dynamics: Topological defects from symmetry breaking. *International Journal of Modern Physics A* **29**, 1430018 (2014).
- [85] A. Polkovnikov and V. Gritsev. Breakdown of the adiabatic limit in low-dimensional gapless systems. *Nature Physics* **4**, 477–481 (2008).
- [86] W. Zwerger. Thermodynamics: Limited adiabaticity. *Nature Physics* **4**, 444–446 (2008).
- [87] F. Pellegrini, S. Montangero, G. E. Santoro, and R. Fazio. Adiabatic quenches through an extended quantum critical region. *Physical Review B* **77**, 140404 (2008).
- [88] S. Deng, G. Ortiz, and L. Viola. Dynamical non-ergodic scaling in continuous finite-order quantum phase transitions. *EPL* **84**, 67008 (2008).
- [89] U. Schollwöck. The density-matrix renormalization group in the age of matrix product states. *Annals of Physics* **326**, 96–192 (2011).
- [90] G. Vidal. Classical Simulation of Infinite-Size Quantum Lattice Systems in One Spatial Dimension. *Physical Review Letters* **98**, 070201 (2007).
- [91] J. Eisert, M. Cramer, and M. B. Plenio. Colloquium: Area laws for the entanglement entropy. *Reviews of Modern Physics* **82**, 277–306 (2010).
- [92] E. H. Lieb and D. W. Robinson. The finite group velocity of quantum spin systems. *Communications in Mathematical Physics* **28**, 251–257 (1972).

- 
- [93] M. B. Hastings. Light-cone matrix product. *Journal of Mathematical Physics* **50**, 095207 (2009).
- [94] A. J. Daley. *Manipulation and Simulation of Cold Atoms in Optical Lattices*. Phd thesis, University of Innsbruck, Innsbruck (2005).
- [95] D. Gobert, C. Kollath, U. Schollwöck, and G. Schütz. Real-time dynamics in spin-1/2 chains with adaptive time-dependent density matrix renormalization group. *Physical Review E* **71**, 036102 (2005).
- [96] P. Jordan and E. Wigner. Über das Paulische Äquivalenzverbot. *Zeitschrift für Physik* **47**, 631 (1928).
- [97] P. Barmettler, M. Punk, V. Gritsev, E. Demler, and E. Altman. Relaxation of Antiferromagnetic Order in Spin-1/2 Chains Following a Quantum Quench. *Physical Review Letters* **102**, 130603 (2009).
- [98] H. Bethe. Zur Theorie der Metalle. *Zeitschrift für Physik* **71**, 205 (1931).
- [99] J.-S. He, A. Foerster, X. W. Guan, and M. T. Batchelor. Magnetism and quantum phase transitions in spin-1/2 attractive fermions with polarization. *New Journal of Physics* **11**, 073009 (2009).
- [100] T. Vekua, S. I. Matveenko, and G. V. Shlyapnikov. Curvature effects on magnetic susceptibility of 1D attractive two component fermions. *JETP Letters* **90**, 289 (2009).
- [101] P. Calabrese and J. Cardy. Entanglement entropy and quantum field theory. *Journal of Statistical Mechanics: Theory and Experiment* **2004**, P06002 (2004).
- [102] I. Affleck and Ludwig, Andreas W. W. Universal noninteger “ground-state degeneracy” in critical quantum systems. *Physical Review Letters* **67**, 161 (1991).
- [103] C. Pethick and H. Smith. *Bose-Einstein condensation in dilute gases* (Cambridge University Press, Cambridge, New York), 2nd edition (2008).



# Acknowledgements

First of all, I want to express my gratitude to my supervisor PD Dr. Fabian Heidrich-Meisner for his advice and assistance and the many times, he patiently gave helpful comments on my work.

Next, I want to thank Florian Dorfner for the many discussions about my code and for helping me finding bugs. I also want to give thanks to him for proof-reading parts of this thesis.

Special thanks go to Luis Riegger for the discussion about his thesis.

Further, I owe thanks to my officemates Fabian Kolley and Jan Stolpp and the other master students Benjamin Spreng and Thomas Martynec for the good atmosphere and lots of discussions about physics and other stuff.

Last but not least, I want to thank my family and friends for giving me the support throughout my studies and always reminding me that there is a life outside of physics.



# Eigenständigkeitserklärung

Hiermit erkläre ich, die vorliegende Arbeit selbständig verfasst zu haben und keine anderen als die in der Arbeit angegebenen Quellen und Hilfsmittel benutzt zu haben.

München, 16. September 2015

Jan Kumlin